Unusual growth of ZnO film induced by ion bombardment and applications of ZnO film to acoustic wave devices

By Shinji TAKAYANAGI

Doshisha University

Graduate School of Engineering

November 2013

Doshisha University

Graduate School of Engineering

ABSTRACT

Unusual growth of ZnO film induced by ion bombardment and applications of ZnO film to acoustic wave devices

By Shinji TAKAYANAGI

SUPERVISOR: Professor Mami MATSUKAWA

A polycrystalline film usually grows in its most densely packed plane parallel to a substrate plane. In case of ZnO film, ion bombardment to the substrate during film deposition suppresses the usual (0001)-oriented grain growth, resulting in the preferential development of unusual $(11\bar{2}0)$ or $(10\bar{1}0)$ orientation. This is because the most densely packed (0001) plane should incur more damage by ion bombardment than the $(11\bar{2}0)$ and $(10\bar{1}0)$ planes. The author demonstrated that the unusual crystalline growth can occur by using energetic negative ions generated in the RF magnetron sputtering without using separated ion source. Negative ion energy and flux entering the substrate were quantitatively measured by electrostatic energy analyzer, and compared with the preferential crystalline growth of the unusual $(11\bar{2}0)$ orientation in ZnO films. Strong XRD intensity of the $(11\bar{2}0)$ orientation was found at the cathode erosion area where large amount of high energy negative ion of 170-250 eV was observed in low gas pressure of 0.1 Pa. In addition the author proposed applying RF substrate bias in RF magnetron sputtering method to induce the positive ion bombardment to the substrate. This method made possible to form preferential $(11\bar{2}0)$ or $(10\bar{1}0)$ orientation in the conditions where the (0001) oriented film was grown without the substrate bias. Then, the potentiality of these $(11\bar{2}0)$ and $(10\bar{1}0)$ oriented ZnO films where the crystallite c-axis unidirectionally-aligned and parallel to the substrate plane was investigated for guided acoustic waves including Lamb waves. In theoretical analyses, value of electromechanical coupling coefficient K^2 reached 10.5% for the first symmetrical mode Lamb wave. Finally, the Lamb wave device was fabricated, and the first symmetrical mode Lamb wave was experimentally excited.

ACKNOWLEDGEMENTS

I would like to show my greatest appreciation to the following people supporting my study. First, I am particularly grateful for the tremendous support given by Prof. Mami Matsukawa. She gave me insightful comments and suggestions not only in the laboratory but also on the way home. I am also deeply grateful to Prof. Yoshiaki Watanabe. He provides me with sincere encouragement, and his advices are extremely valuable as a person.

I would like to offer my special thanks to Dr. Takahiko Yanagitani at Nagoya Institute of Technology. Without his incisive guidance and constant encouragement, this thesis would not have been possible. Extensive discussions in the midnight were greatly helpful for my study.

For piezoelectric device fabrications, I received generous support from Prof. Philippe Pernod, Dr. Abdelkrim Talbi, Dr. Nicolas Tiercelin, and Dr. Jean-Claude Gerbedoen at Joint International Laboratory LIA LEMAC-LICS in Institute of Electronics, Microelectronics and Nanotechnology (IEMN).

I greatly appreciate Prof. Tadashi Ohachi for his willing cooperation on XRD measurement equipment.

I would like to thank Prof. Iwaki Akiyama for his warm-hearted encouragement. Constructive comments given by Assoc. Prof. Daiske Koyama have been a great help in piezoelectric actuators.

I also wish to acknowledge Dr. Kenji Yoshida, Dr. Takayuki Kawamoto, and Mr. Naoki Morisato for technical supports in the experiments. My sincere thanks go to my colleagues at Laboratory of Ultrasonic Electronics in Doshisha University, including Mr. Hiroyuki Sano, Mr. Tomohiro Nakatsuji, Mr. Mamoru Sawasaki, Mr. Yuta Nakahigashi, Mr. Kenji Fukui, Mr. Kosuke Imamura, Mr. Ryo Ikoma, Mr. Takeshi Sugimoto, Mr. Masahiro Okino, Mr.

Daisuke Suga, Mr. Yoshiya Kato, Mr. Masanari Yoshida, Mr. Ryosuke Hashimoto, Mr. Hayato Ichihashi, and Ms. Hiroko Tsuneda.

Finally, I would like to express my gratitude to my parents for their long-term supports and considerable encouragements that have enabled me to maintain my research.

This work was partly supported by a Research Fellowship for Young Scientists (No. 24-5255) from the Japan Society for the Promotion of Science.

Shinji TAKAYANAGI

高柳真司

CONTENTS

CHAPTER 1.

INTRODUCTION

1.1 PURPOSE ····· 1

1.2 UNUSUAL CRYSTAL GROWTH OF ZnO ····· 2

1.3 APPLICATION OF C-AXIS-PARALLEL-ORIENTED ZnO ····· 4

1.3.a BULK ACOUSTIC WAVE DEVICE ····· 4

1.3.b SURFACE ACOUSTIC WAVE DEVICE AND LAMB WAVE DEVICE ····· 6

1.4 TOPIC OF CHAPTERS ····· 9

REFERENCES ····· 10

CHAPTER 2.

SPUTTERING PROCESS

2.1 SPUTTERING METHOD ····· 13

2.1.a DC SPUTTERING DEPOSITION ····· 14

2.1.b RF SPUTTERING DEPOSITION ····· 16

2.2 ION BOMBARDMENT ····· 18

2.3 MAGNETRON CIRCUIT ····· 20

REFERENCES ····· 23

CHAPTER 3.

UNUSUAL GROWTH OF ZnO

INDUCED BY NEGATIVE ION BOMBARDMENT

IN RF MAGNETRON SPUTTURING

3.1 UNUSUAL GROWTH OF ZnO ····· 24

3.2 EXPERIMENTAL METHODS ····· 25

3.2.a ZnO FILM GROWTHS USING RF MAGNETRON SPUTTERING ····· 25

3.2.b EVALUATION METHOD OF CRYSTALLINE ORIENTATION ····· 25

3.2.c MEASUREMENTS OF ENERGETIC ION BOMBARDMENT ····· 26

3.3 RESULTS AND DISCUSSIONS ····· 29

3.3.a CRYSTALLIZATIONS OF THE ZnO SAMPLES ····· 29

3.3.b Energy and flux of ions bombarding the substrate ····· 31
3.3.c Effect of ion bombardment during deposition on unusual crystal growth in ZnO films ····· 36
References ····· 39

CHAPTER 4.
ORIENTATION CONTROL OF HEXIAGONAL FILMS BY POSITIVE ION BOMBARDMENT USING RF SUBSTRATE BIAS SPUTTERING

4.1 Substrate bias sputtering ····· 40
4.1.a No-bias condition ····· 41
4.1.b Positive-DC-bias condition ····· 41
4.1.c Negative-DC-bias condition ····· 43
4.1.d RF-bias condition ····· 43
4.2 Orientation control of ZnO film using RF-substrate-bias sputtering ····· 45
4.2.a Experimental methods ····· 45
4.2.b Results and discussions ····· 47
4.3 Unusual crystal growth of AlN film using RF-substrate-bias sputtering ····· 52
4.3.a Ion bombardment during AlN film growth ····· 52
4.3.b AlN and ScAlN film growth ····· 54
References ····· 57

CHAPTER 5.
PIEZOELECTRIC EFFECT AND ELECTROMECHANICAL CONVERSION

5.1 Piezoelectric effect ····· 58
5.2 Material constant tensor ····· 58
5.3 BAW propagation ····· 61
5.4 Electromechanical coupling coefficient ····· 65
References ····· 67

CHAPTER 6.

ESTIMATION OF ELECTROMECHANICAL COUPLING COEFFICIENT AND THICKNESS OF UNORIENTED LAYER

6.1 One-dimensional mechanical transmission line model ····· 68

6.1.a Mason's equivalent circuit model ····· 69

6.1.b Equivalent circuit model including piezoelectrically inactive layer ····· 73

6.2 Estimation of electromechanical coupling coefficient ····· 76

6.3 Estimation of thickness of unoriented layer ····· 79

References ····· 86

CHAPTER 7.

APPLICATION OF C-AXIS-PARALLEL ORIENTED ZnO FOR SURFACE ACOUSTIC WAVE AND LAMB WAVE DEVICES

7.1 SAW and Lamb wave properties of c-axis parallel oriented ZnO film ····· 88

7.2 SAW and Lamb wave device fabrications ····· 93

References ····· 99

CHAPTER 8.

CONCLUSIONS ····· 100

APPENDIX

APPENDIX A.

EFFECT OF METAL AND OXIDE MODE OF Zn TARGET ON c-AXIS-PARALLEL-ORIENTED ZnO FILM GROWTH IN A REACTIVE MAGNETRON SPUTTERING

A.1 Introduction ····· 104

A.2 ZnO film fabrications ····· 105

A.3 Crystalline Orientations of ZnO films ····· 108

A.4 CONCLUSIONS ····· 110
REFERENCES ····· 111

APPENDIX B.

WIDEBAND MULTIMODE TRANSDUCER CONSISTING OF c-AXIS TILTED ZnO/c-AXIS NORMAL ZnO MULTILAYER

B.1 INTRODUCTION ····· 113
B.2 EXPERIMENTAL METHODS ····· 115
B.2.a TRANSDUCER FABRICATION ····· 115
B.2.b TRANSDUCER CHARACTERIZATION ····· 116
B.3 CRYSTALLINE ORIENTATION OF THE TRANSDUCER ····· 117
B.4 FREQUENCY CHARACTERISTICS OF THE TRANSDUCER ····· 120
B.5 CONCLUSIONS ····· 122
REFERENCES ····· 124

LIST OF SYMBOLS

f_r	Resonant frequency of BAW resonator
v	BAW velocity of piezoelectric material
d	Thickness of piezoelectric material
V_1	Sheath voltage toward electrode 1
V_2	Sheath voltage toward electrode 2
V_p	Plasma potential
A_1	Area of electrode 1
A_2	Area of electrode 2
V_T	Average target voltage
V_{Tt}	Target voltage
V_{Pt}	Plasma potential
V_S	Average target potential
V_P	Average substrate potential
$\boldsymbol{B}$	Magnetic field
q	Electric charge of a particle
$\boldsymbol{v}$	Velocity of a particle
$\boldsymbol{E}$	Electric field
$\boldsymbol{F}$	Total force
ψ	Elevation angle in XRD mesurement
ϕ	Rotation angle in XRD mesurement
T_{ij}	Stress component
S_{kl}	Strain component
e_{ijk}	Piezoelectric constant
E_k	Electric field
D_i	Electrical displacement
$c^E{}_{ijkl}$	Elastic constant under constant electric field
$\varepsilon_{ik}{}^S$	Dielectric constant
ρ	Density
$[a]$	Transformation matrix
$[M]$	6×6 transformation matrix

u_i	Mechanical displacement
φ	Electric potential
ω	Angular frequency
v	Phase velocity
k	Electromechanical coupling coefficient
U_i	Input energy
U_o	Output energy
c^D	Elastic constant under constant electric displacement
K	Effective electromechanical coupling coefficient
v_f	Phase velocity for free surface of wave propagation path
v_m	Phase velocity for metallized surface of wave propagation path
F_i	Force acting on surface of elastic solid
V	Voltage
I	Current
γ	Propagation constant
Z	Acoustic impedance
C	Static capacitance
ϕ_0	Ratio of transformer
Y_in	Input admittance
CL	Conversion loss
G_f	Input conductance
B_f	Input susceptance
S_{11}	Reflection coefficients
d_n	Thickness of the piezoelectrically inactive layer
H/λ	Normalized film thickness
θ	c-Axis tilt angle
R_n	Over tone mode in Rayleigh wave
A_0	First asymmetrical mode in Lamb wave
S_0	First symmetrical mode in Lamb wave

LIST OF ABBREVIATIONS

AZO	Al-doped ZnO
BAW	Bulk acoustic wave
BGSW	Bleustein-Gulyaev-Shimizu Wave
CCP	Capacitively coupled plasma
DC	Direct current
ED	Electron diffraction
FBAR	Film bulk acoustic resonator
FWHM	Full width at half maximum
HBAR	High-overtone bulk acoustic resonator
IBAD	Ion-beam-assisted deposition
IDT	Interdigital transducer
MEMS	Micro-electro-mechanical system
MOCVD	Metalorganic chemical vapor deposition
RF	Radio frequency
RGA	Residual gas analysis
SAW	Surface acoustic wave
SEM	Scanning electron microscopy
SH-SAW	Shear horizontal surface acoustic wave
SV wave	Shear vertical wave
TEM	Transmission electron microscopy
UHF	Ultra-high-frequency
VHF	Very-high-frequency
XRD	X-ray diffraction
YSZ	Yttria-stabilized zirconia

LIST OF FIGURES

Fig. 1.1 Three types of crystalline orientation in a hexagonal sturucture.

Fig. 1.2 (a) Longitudinal-mode and (b) shear-mode BAW resonators.

Fig. 1.3 (a) HBAR and (b) FBAR.

Fig. 1.4 (a) Rayleigh SAW excitation with a c-axis-normally-oriented film, and (b) SH-SAW or (c) Rayleigh SAW excitations with a c-axis-parallel-oriented film.

Fig. 1.5 Lamb wave device.

Fig. 2.1 Schematic of sputtering phenomenon.

Fig. 2.2 Conventional sputtering system.

Fig. 2.3 RF power supply.

Fig. 2.4 Asymmetric discharge system with a blocking capacitor.

Fig. 2.5 Plasma potential and target voltage in the asymmetric system.

Fig. 2.6 Average-potential distribution in a conventional RF sputtering system.

Fig. 2.7 Motion of an electron ejected from a target surface in a magnetic field and electric field. The magnetic field is parallel, and the electric field is orthogonal to the surface.

Fig. 2.8 (a) Magnetic field with a magnetron circuit in the conventional magnetron sputtering system, and (b) motion of an electron on a disc target.

Fig. 3.1 RF magnetron sputtering apparatus.

Fig. 3.2 Measurement system for the spatial distributions of the amount of ion flux and the ion energy in the RF magnetron sputtering.

Fig. 3.3 Mass spectra of (a) positive ions and (b) negative ions bombarding the substrate in 1 Pa, and that of (c) positive ions and (d) negative ions in 0.1 Pa.

Fig. 3.4 XRD patterns of the samples grown in (a) 1 Pa and (b) 0.1 Pa.

Fig. 3.5 Integrated intensities of (0002) and $(11\bar{2}0)$ XRD peaks of the samples with (a) 1 Pa and (b) 0.1 Pa

Fig. 3.6 Amount of ion flux and ion energy of O_2^+ positive ions as functions of the distance from anode center at (a) 1 Pa and (b) 0.1 Pa.

Fig. 3.7 Amount of ion flux and ion energy of O^- negative ions as functions of the distance from anode center at (a) 1 Pa and (b) 0.1 Pa.

Fig. 3.8 Mass spectra of (a) positive ions and (b) negative ions bombarding the substrate. (c) the amount of ion flux as functions of the distance from anode center and the ion energy of O^- negative ions during pure argon discharge in 0.1 Pa.

Fig. 3.9 FWHM values of ω-rocking curves of the sample with 0.1 Pa.

Fig. 3.10 $(11\bar{2}2)$ pole figure of the sample with 0.1 Pa, measured at 30 mm from the anode center.

Fig. 4.1 Average-potential distribution in a (a) positive-DC-bias sputtering system and (b) negative-DC-bias sputtering.

Fig. 4.2 Average-potential distribution in an RF-bias sputtering.

Fig. 4.3 RF-bias sputtering system.

Fig. 4.4 Measurement system for the spatial distributions of the amount of ion flux and the ion energy in the RF-bias sputtering.

Fig. 4.5 Energy distributions of (a) O_2^+ positive ions and (b) O^- negative ions which enter the substrate during the deposition with 2 MHz RF bias.

Fig. 4.6 (a) XRD patterns and (b) ratios of the XRD peak integrated intensities of the samples grown without bias, or with 2 MHz RF bias. I_{0002}, $I_{11\bar{2}0}$, and $I_{10\bar{1}0}$ are the integrated intensities of the (0002), $(11\bar{2}0)$, and $(10\bar{1}0)$ XRD peaks, respectively.

Fig. 4.7 Summary of the relationship between the preferred orientations and the ion bombardment in RF bias sputtering deposition.

Fig. 4.8 $(10\bar{1}1)$ pole figure of the sample with the RF bias of 50 W, measured at (a) 0 and (b) 45 mm from the anode center.

Fig. 4.9 Mass spectra of (a) positive ions and (b) negative ions bombarding the substrate in AlN film growth, and that of (c) negative ions in ZnO film growth using a conventional RF magnetron sputtering.

Fig. 4.10 Energy distributions of Ar^+ positive ions which enter the substrate during the AlN growth with 2 MHz RF bias.

Fig. 4.11 XRD patterns of the AlN and ScAlN samples with 2 MHz RF bias.

Fig. 5.1 Hexagonal structure.

Fig. 5.2. Euler angles ϕ, θ, and ψ for the coordinate transformations.

Fig. 5.3 Analytical model of BAW propagation in a c-axis-parallel-oriented film.

Fig. 6.1 HBAR structure consisting of c-axis-parallel-oriented film.

Fig. 6.2 Equivalent circuit of non-piezoelectric elastic solid.

Fig. 6.3 Equivalent circuit of piezoelectric elastic solid.

Fig. 6.4 One-dimensional mechanical transmission line model of the HBAR.

Fig. 6.5 Schematic diagrams of piezoelectric polarizations induced at upper and lower parts of (a) a single uniform piezoelectric layer and (b) a multilayer including the piezoelectrically inactive multilayer, respectively.

Fig. 6.6 One-dimensional mechanical transmission line model included a piezoelectrically inactive layer. The substrate thickness is assumed to be infinite to exclude the effect of acoustic waves reflected from the bottom surface of the substrate.

Fig. 6.7 Measurement system of reflection coefficient S_{11} by a network analyzer.

Fig. 6.8 Impulse response of the HBAR.

Fig. 6.9 Frequency response of the shear-mode conversion losses of (a) sample A and (b) sample B.

Fig. 6.10 Frequency responses of the longitudinal-mode conversion losses of (a) the ZnO(0001) film resonator (sample C) and (b) the ZnO(0001)/AZO(0001) film resonator (sample D). The simulated minimum conversion losses using k_{33}=0.23 in Fig. 6.9(a) and k_{33}=0.22 in Fig. 6.9(b) provided the best agreement with the experimental one at the fundamental thickness longitudinal mode resonant frequency L_1.

Fig. 6.11 Frequency responses of the longitudinal-mode conversion losses of (a) the ZnO($11\bar{2}0$) film resonator (sample A) and (b) the ZnO($10\bar{1}0$) film resonator (sample B). The simulated minimum conversion losses using k_{15}=0.12 in Fig. 6.10(a) and k_{15}=0.17 in Fig. 6.10(b) provided the best agreement with the experimental one at the fundamental thickness shear mode resonant frequency S_1.

Fig. 6.12 (a) Cross-sectional TEM image of the ($11\bar{2}0$) ZnO film (sample A) and ED patterns at the region (b) 3.3 μm (region A), (c) 1.9 μm (region B) and (d) 0.5 μm (region C) from the Al bottom electrode.

Fig. 7.1 Calculated electromechanical coupling coefficients of quasi-longitudinal wave k'_{33} and quasi-shear wave k'_{35} for ZnO as a function of the angle θ between the c-axis and electric field direction。

Fig. 7.2 Calculated electromechanical coupling coefficient K^2 of the second mode (Sezawa) SAW as a function of the c-axis tilt angle θ and normalized film thickness H/λ in IDT/ZnO/Si structure.

Fig. 7.3 the profile curves of K^2 as a function of H/λ at (a) θ = 0º and (b) 90º in IDT/ZnO/Si structure

Fig. 7.4 Calculated K^2 values of the first symmetrical Lamb wave mode (S_0) in (a) ZnO film and (b) ZnO film/bottom electrode, respectively, as functions of normalized film thickness H/λ and c-axis tilt angle θ.

Fig. 7.5 Profile curves of K^2 as a function of H/λ at $\theta = 0^\circ$ and 90º in the first asymmetrical mode (A_0) and first symmetrical mode (S_0) of (a) ZnO film and (b) ZnO film/bottom electrode

Fig. 7.6 XRD pattern of the sample on Si substrate.

Fig. 7.7 (a) IDT configurations and (b) optic-microscopic image of the IDT structure.

Fig. 7.8 Insertion loss characteristic observed in the Al/Ti IDT/c-axis-parallel-oriented ZnO/Si substrate structure.

Fig. 7.9 SAW velocities calculated as a function of normalized film thickness H/λ.

Fig. 7.10 Optic-microscopic image of the Al/Ti IDT/c-axis-parallel-oriented ZnO membrane structure.

Fig. 7.11 Insertion loss characteristic observed in the Al/Ti IDT/c-axis-parallel-oriented ZnO membrane structure.

Fig. 7.12 Lamb wave velocities calculated as a function of normalized film thickness H/λ.

Fig. A.1 Reactive RF magnetron sputtering system for fabricating c-axis parallel oriented ZnO films.

Fig. A.2 Zn target used in the sputtering deposition (a) in the metal mode and (b) the oxide mode. Temperatures of the target surface in the metal mode and the oxide mode were adjusted to 300 ºC and 340 ºC, respectively.

Fig. A.3 2θ–ω scan XRD patterns of the ZnO films deposited (a) in the metal mode and (b) in the oxide mode of the Zn target.

Fig. A.4 FWHM of the $(11\bar{2}0)$ plane ω–scan rocking curve in the ZnO films deposited in the metal mode and in the oxide mode.

Fig. B.1 Structures of the transducers consisting of (a) single c-axis tilted ZnO layer and (b) c-axis tilted ZnO/c-axis normal ZnO multilayer.

Fig. B.2 RF magnetron sputtering system for fabricating c-axis tilted ZnO/c-axis normal ZnO multilayer.

Fig. B.3 ψ-scan profile curve of Au(111) in the multilayer transducer.

Fig. B.4 ψ-scan profile curves of ZnO(0002) in (a) the single layer transducer and (b) multilayer transducer.

Fig. B.5 Cross-sectional SEM image of the multilayer transducer.

Fig. B.6 (a) Longitudinal wave and (b) shear wave conversion losses of the transducers. Dashed lines show the theoretical curves of the single layer transducer. Circles and lines show the experimental and theoretical curves of the multilayer transducer, respectively.

Fig. B.7 Schematic diagrams of piezoelectric polarizations induced at upper and lower parts of (a) the ZnO single layer and (b) ZnO multilayer.

LIST OF TABLES

Table 3.1 Deposition conditions in RF magnetron sputtering.

Table 3.2 Summary of distributions of the ion bombardment and the crystalline orientation under 0.1 Pa.

Table 4.1 Expected conditions of ion bombardment to the substrate.

Table 4.2 Deposition conditions in the RF-bias sputtering.

Table 4.3 Deposition condition of an AlN sample growth in RF-bias sputtering.

Table 6.1 HBAR structures of sample A and B.

Table 6.2 HBAR structures of sample C and D.

Table 7.1 Deposition conditions is grown on a Si substrate in RF magnetron sputtering.

Table A.1 Deposition conditions for ZnO films.

Table B.1 Deposition conditions for c-axis tilted ZnO/c-axis normal ZnO multilayer.

1. INTRODUCTION

1.1 PURPOSE

Crystalline orientation control of thin films has become much more important with the progress in development of smaller and thinner devices. Because of its thermodynamic stability, the close-packed plane of crystal preferentially orients parallel to the substrate plane in polycrystalline thin film growth without epitaxial technique [1.1]. Unusual crystalline orientation is interesting because electrical and mechanical properties have anisotropy in the crystal [1.2-1.4], but these orientations are difficult to obtain.

It is well known that the crystalline orientation of the film is strongly influenced by the crystalline orientation of the substrate. It is mainly caused by epitaxial relationship between the crystalline grains of the film layer and the substrate structure including the bottom electrode [1.5-1.7]. Therefore, the crystalline orientation of the film can be controlled by a suitable choice of the substrate structure. In this epitaxial growth, however, the restriction of the substrate material is an unavoidable problem for device applications.

Strong tendency of the grain growth toward the close-packed direction can be suppressed by the energetic ion bombardment during deposition because the close-packed plane incurs more collision damage than the less densely packed plane, resulting in the preferential development of the unusual crystalline orientation [1.4, 1.8-1.11]. According to this sputter-yield -anisotropy-induced unusual crystal growth, the preferred orientation of polycrystalline films can be controlled by using ion bombardment during deposition.

Many studies have been reported the unusual crystal growth in an ion-beam-assisted deposition (IBAD) of yttria-stabilized zirconia (YSZ) [1.10-1.13], $YBa_2Cu_3O_{7-x}$/YSZ [1.14, 1.15], ZnO [1.4, 1.16], TiN [1.2, 1.3, 1.8, 1.9, 1.17, 1.18] and AlN [1.19, 1.20] films. Deposition source and ion source for substrate ion bombardment in the IBAD are generally separated,

and ions extracted from the ion source are used in this system. The separated ion source has the advantage of being easy to control ion bombardment, but it is difficult to achieve industry applications by means of the expensive ion source.

In this study, the author proposes a method for an unusual crystal growth using ion bombardment in capacitively coupled plasma (CCP) deposition. This method is based on a conventional RF magnetron sputtering, and it does not require the separated ion source. This study will discuss the flux and energy of ions which enter the substrate during the film deposition, and describe an unusual crystal growth of ZnO film without use of an epitaxial growth. Furthermore, piezoelectric devices will be introduced for applications of unusual crystalline oriented ZnO.

1.2 UNUSUAL CRYSTAL GROWTH OF ZnO FILM

ZnO crystal has a hexagonal wurtzite structure. Figure 1.1 shows three types of ZnO crystalline orientation. In general, ZnO films tend to grow in their most densely packed (0001) plane parallel to the substrate plane. Crystalline c-axis in (0001) oriented ZnO is perpendicular to the substrate plane. On the other hand, $(11\bar{2}0)$ and $(10\bar{1}0)$ orientations where the c-axis is unidirectionally-aligned and parallel to the substrate plane are unusual orientations.

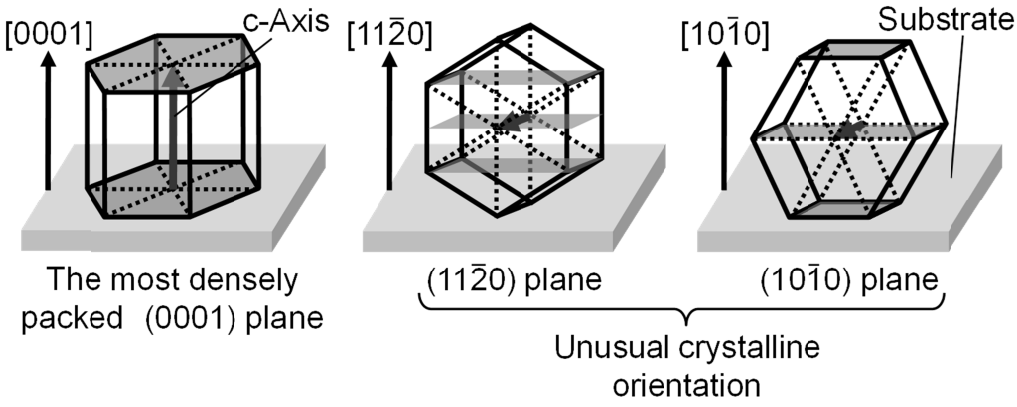

Fig. 1.1 Three types of crystalline orientation in a hexagonal sturucture.

The c-axis parallel $(11\bar{2}0)$ oriented ZnO films can be epitaxially grown on R-sapphire single crystal by metalorganic chemical vapor deposition (MOCVD) [1-21] and sputtering deposition [1-5, 1-22]. On the other hand, without use of epitaxial technique, the $(11\bar{2}0)$ or $(10\bar{1}0)$ oriented ZnO films can be obtained by using oxygen ion beam in IBAD [1.4, 1.16]. The ion bombardment to the substrate during deposition suppresses the (0001)-oriented grain growth, resulting in the preferential development of $(11\bar{2}0)$ or $(10\bar{1}0)$ texture instead of the (0001) texture. This is because the most densely packed (0001) plane should incur more damage by ion bombardment than the $(11\bar{2}0)$ and $(10\bar{1}0)$ planes.

It is well known that the substrate is bombarded with ions during a sputtering deposition. Tominaga et al. have reported that the energetic negative ion generated at oxide cathode bombard the anode plane in a sputtering deposition of the oxide films [1.23, 1.24]. An electron can be easily added to the oxygen atom which has a high electron affinity, and therefore, negative ions such as O^- generate during the deposition. The negative ion bombardment during ZnO film deposition causes a degradation of a usual (0001) orientation [1.23]. However, the preferential unusual crystal growth by negative ion bombardment has not been achieved. This may be due to the insufficient negative ion generation on the sputtering target to induce unusual crystal growth. Chapters 3 and 4 will introduce the methods for increasing the amount of ion bombardment, and describe the unusual crystal growth of ZnO film.

1.3 APPLICATION OF C-AXIS-PARALLEL-ORIENTED ZnO

ZnO has many advantages in terms of large excitation binding energy (60 meV), wide bandgap energy (3.4 eV), well-developed growth process, and high electromechanical coupling coefficient. Therefore, it has found numerous applications such as facial powders, blue light emitting diode, varistor, transparent electrode films, and piezoelectric devices [1.25]. Unusual

c-axis-parallel-oriented ZnO films can further expand the possibilities of applications by its anisotropy of electrical and mechanical properties. In this section, piezoelectric device applications of c-axis-parallel-oriented ZnO films will be described.

1.3.a BULK ACOUSTIC WAVE DEVICE

Electromechanical conversion by piezoelectric devices is important for frequency filters in mobile communications [1.26, 1.27] and microsensors [1.28, 1.29]. A bulk acoustic wave (BAW) can be excited when electric field is applied to a piezoelectric material. A sandwich structure consisting of Top electrode/piezoelectric material/bottom electrode is typically used for the BAW excitation. Figure 1.2 shows two types of the BAW resonator. The crystalline c-axis corresponds to the piezoelectric axis in a hexagonal wurtzite structure including ZnO crystal. If the direction of the applied electric field is parallel to the c-axis, the resonator excites longitudinal-mode BAW, as shown in Fig. 1.2(a). On the other hand, if the direction of the applied electric field is orthogonal to the c-axis, the resonator can excite shear-mode BAW, as shown in Fig. 1.2(b). The resonant frequency f_r of these resonators is given by

$$f_r = \frac{v}{2d}, \tag{1.1}$$

where v is BAW velocity and d is thickness of the piezoelectric material. Equation (1.1) indicates that thinner piezoelectric material is required for high-frequency BAW devices. Therefore, in very-high-frequency (VHF) to ultra-high-frequency (UHF) range, piezoelectric films are used [1.26, 1.28, 1.30].

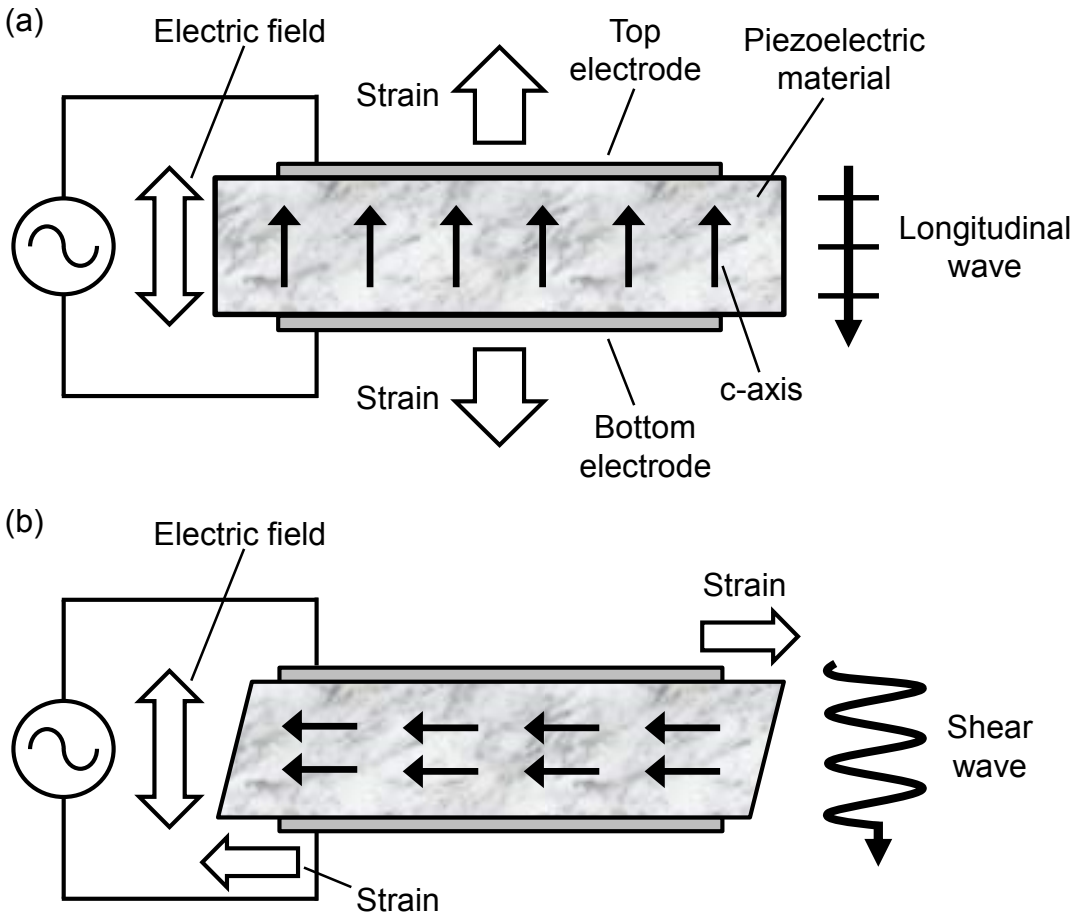

Fig. 1.2 (a) Longitudinal-mode and (b) shear-mode BAW resonators.

Because a base substrate is needed in the thin film growth, the resonator consisting of piezoelectric thin film includes the substrate material, as shown in Fig. 1.3(a). This structure is called high-overtone bulk acoustic resonator (HBAR). The BAW is excited at the piezoelectric film and propagates in the substrate. The leakage of BAW into the substrate is the energy loss for sensor applications. To prevent this, the substrate of HBAR is etched around the bottom electrode, as shown in Fig. 1.3(b). This structure is called film bulk acoustic resonator (FBAR).

Longitudinal-mode FBARs are used for duplexers [1.26] and gas sensors [1.28]. Almost all of them consists of ZnO or AlN films whose c-axis is perpendicular to the substrate [1.30-1.32]. On the other hand, shear-mode FBARs have an important advantage over the longitudinal-mode FBARs. Because shear-mode BAW which is excited at the piezoelectric film does not

leak into liquids, shear-mode FBARs can operate in liquid phase [1-33]. These devices are promising for the sensors to measure viscosity of fluids and detect mass loading due to biochemical reaction. Furthermore, because the sensitivity of the detection depends on the thickness of the piezoelectric material, the FBAR has a higher sensitivity than the resonator consisting of a single-crystal piezoelectric plate. Therefore, c-axis-parallel-oriented films, which can excite shear-mode BAW as shown in Fig. 1.2(b), are suitable for shear-mode FBARs.

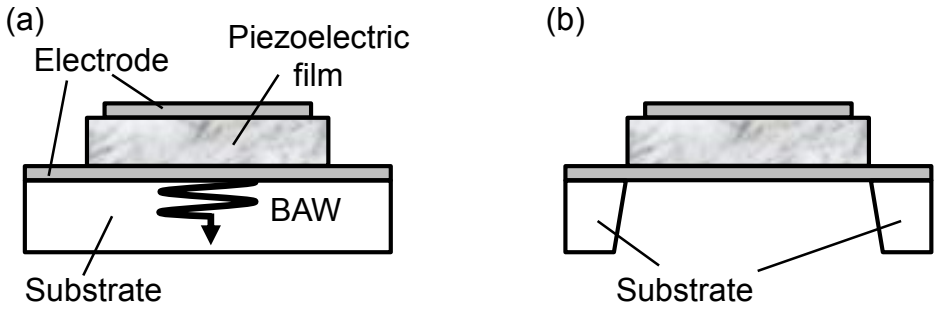

Fig. 1.3 (a) HBAR and (b) FBAR.

1.3.b SURFACE ACOUSTIC WAVE DEVICE AND LAMB WAVE DEVICE

A surface acoustic wave (SAW) is generally excited with an interdigital transducer (IDT) on a piezoelectric substrate, and it propagate along the surface of the substrate. A piezoelectric thin film/substrate structure is sometimes used to provide desired SAW properties such as a high electromechanical coupling and a specific mode of propagation [1.27, 1.29, 1.34]. The thin film acts as a wave guide in this case.

Figure 1.4(a) shows an IDT/ c-axis-normally-oriented film/substrate structure. This structure can excite Rayleigh SAW. Because the c-axis-normally-oriented film is easy to be obtained, it is widely used frequency filters and duplexers in mobile phones [1.27, 1.34].

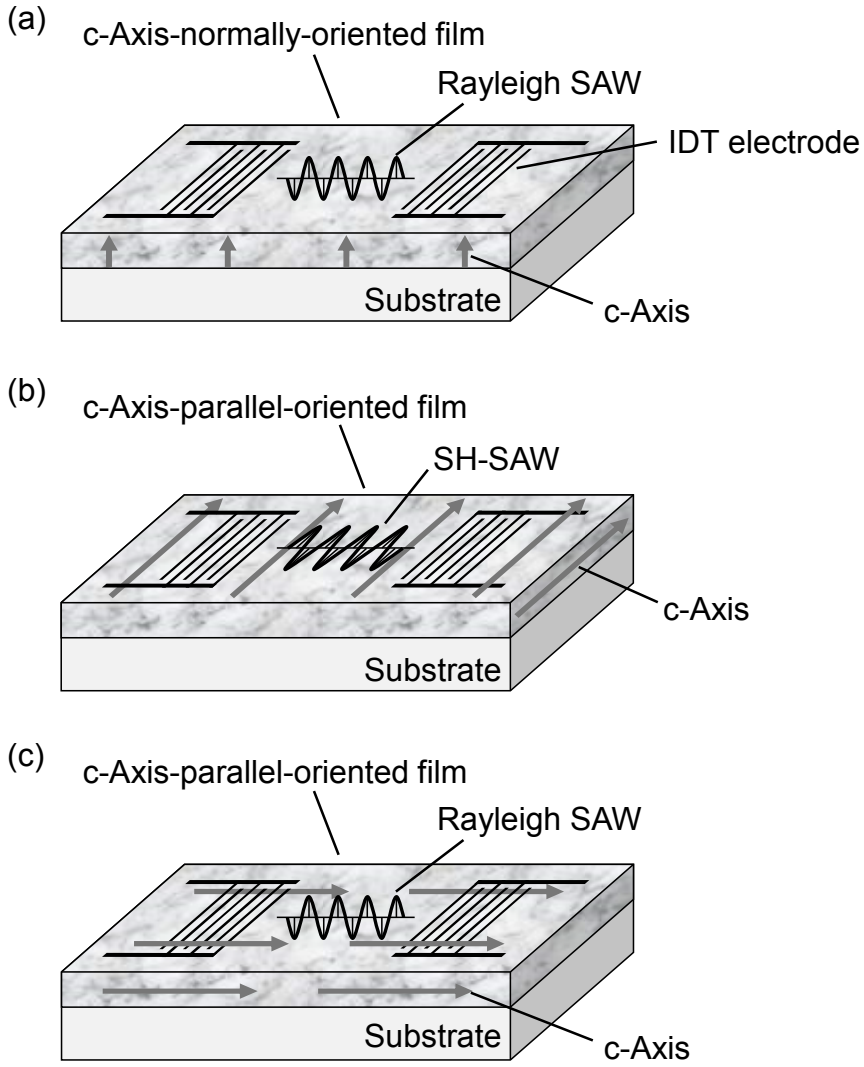

Fig. 1.4 (a) Rayleigh SAW excitation with a c-axis-normally-oriented film, and (b) SH-SAW or (c) Rayleigh SAW excitations with a c-axis-parallel-oriented film.

Figures 1.4(b) and (c) show IDT/ c-axis-parallel-oriented film/substrate structures. In Fig 1.4 (b), the c-axis of the piezoelectric film is parallel to the substrate plane and orthogonal to the SAW-propagation direction. This structure can excite a shear horizontal SAW (SH-SAW) which is known Bleustein-Gulyaev-Shimizu Wave (BGSW) [1.35]. Even if liquids are loaded on the SAW-propagation path, SH-SAW does not significantly leak to the liquids as the same manner of the shear-mode FBAR [1.36]. Therefore, this

structure is expected for the sensors to measure the viscosity and conductivity of liquids [1.37]. In Fig 1.4 (c), on the other hand, the c-axis of the piezoelectric film is parallel to both the substrate plane and the SAW-propagation direction. This structure excites Rayleigh SAW, as is the case in Fig. 1.4(a). However, the higher electromechanical coupling coefficient is achievable with the structure consisting of the c-axis-parallel-oriented film on a Si substrate, which will be discussed in Chapter 7. Because both the wideband SAW filters and high-sensitivity SAW sensors require the substrate structure with the high electromechanical coupling, the c-axis-parallel-oriented film are promising for these SAW devices.

Figure 1.5 shows a Lamb wave device. It is usually prepared by etching the substrate of the SAW device around the piezoelectric film. Reflecting at the top and bottom boundaries of the film, BAWs which are induced by an IDT propagate as a Lamb wave [1-38]. Because the acoustic wave energy is confined within the film, Lamb wave devices usually achieve the higher electromechanical coupling than SAW devices, which will be also discussed in Chapter 7.

In micro-electro-mechanical system (MEMS), Si etching is a very important process and well-studied. Therefore, if the c-axis-parallel-oriented film can be grown on a Si substrate without an epitaxial technique, the development of the high-sensitivity Lamb wave sensors is expected.

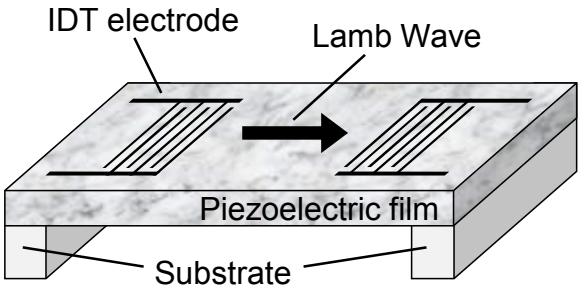

Fig. 1.5 Lamb wave device.

1.4 TOPIC OF CHAPTERS

In Chapter 2, the conventional RF magnetron sputtering will be introduced. This chapter will also describe the mechanism of the ion bombardment to the substrate during the deposition. Chapter 3 will describe the unusual crystal growth of $(11\bar{2}0)$ oriented ZnO film on a glass substrate. The effect of the energetic-negative-ion bombardment on ZnO orientation will be discussed. Chapter 4 will introduce film growth of c-axis-parallel-oriented ZnO by RF substrate bias sputtering method. Positive ions are easily accelerated to the substrate in this method. In addition, unusual growth of AlN films will be described.

In Chapter 5, acoustic wave excitations and propagations will be introduced. This chapter will also describe an electromechanical coupling coefficient which provides an index of piezoelectricity. In Chapter 6, conversion losses of HBARs consisting of a ZnO film will be measured. The electromechanical coupling coefficients of ZnO films will be evaluated by the comparison of the conversion loss with a mechanical transmission line model of the HBAR. In addition, a method for predicting thickness of unoriented layer of ZnO film in the initial stage of its growth will be discussed. Chapter 7 will introduce the SAW and Lamb wave devices with c-axis-parallel-oriented ZnO film. The electromechanical coupling coefficients of these devices will be calculated, and then these devices will be fabricated. Finally, this study will be concluded in Chapter 8.

Appendix A will introduce the effect of metal mode and oxide mode of Zn target on $(11\bar{2}0)$ oriented ZnO film growth in an RF magnetron sputtering. Appendix B will introduce a wideband ultrasonic transducer consisting of c-axis-tilted ZnO/c-axis-normally-oriented ZnO multilayer on the Au(111)/Ti/silica glass substrate.

REFERENCES

[1.1] K. Wasa and S. Hayakawa,
Handbook of Sputter Deposition Technology (Academic, New York, 1992), p. 147.

[1.2] L. Alberts, R. Leutenecker, P. Moine, and G.K. Wolf,
Surf. Coat. Technol. **84**, 453 (1996).

[1.3] G. Abadias and Y. Y. Tse,
J. Appl. Phys. **95,** 2414 (2004).

[1.4] T. Yanagitani and M. Kiuchi,
J. Appl. Phys. **102**, 044115 (2007).

[1.5] T. Mitsuyu, S. Ona, and K. Wasa,
J. Appl. Phys. **51**, 2464 (1980).

[1.6] R.H.Wittstruck, X. Tong, N. W. Emanetoglu, P. Wu, Y. Chen, J. Zhu, S. Muthukumar, Y. Lu and A. Ballato,
IEEE Trans. Ultrason. Ferroelectr. Freq. Control **50**, 1272 (2003).

[1.7] Y. Yoshino,
J. Appl. Phys. **105**, 061623 (2009).

[1.8] W. Ensinger,
Nucl. Instrum. Methods Phys. Res. B **106**, 142 (1995).

[1.9] W. Ensinger,
Nucl. Instrum. Methods Phys. Res. B **127-128**, 796 (1997).

[1.10] K. G. Ressler, N. Sonnenberg, and M. J. Cima,
J. Am. Ceram. Soc. **80**, 2637 (1997).

[1.11] I. O. Usov, P. N. Arendt, and K. E. Sickafus,
Nucl. Instrum. Methods Phys. Res. B **268**, 622 (2010).

[1.12] A. Knierim, R. Auer, J. Geerk, Y. Li, G. Linker, O. Meyer, J. Reiner, P. Schweiss, and R. Smithey,
Nucl. Instrum. Methods Phys. Res. B **127-128**, 832 (1997).

[1.13] Z. Wang, K. Shi, H. Chen, F. Feng, J.C. Sun, and Z. Han,
Thin solid films **517**, 2044 (2009).

[1.14] Y. Iijima, N. Tanabe, O. Kohno, and Y. Ikeno,
Appl. Phys. Lett. **60**, 769 (1992).

[1.15] R. P. Reade, P. Berdahl, R. E. Russo, and S. M. Garrison,
Appl. Phys. Lett. **61**, 2231 (1992).

[1.16] D. Köhl, G. Natarajan, and M. Wuttig,
J. Phys. D: Appl. Phys. **45**, 245302 (2012).

[1.17] L. Alberts, R. Leutenecker, and G.K. Wolf,
Surf. Coat. Technol. **84**, 443 (1996).

[1.18] J.-H Huang, C.-H Lin, C.-H Ma, and H. Chen,
Scr. Mater. **42**, 573 (2000).

[1.19] Y. Nakamura, Y. Watanabe, S. Hirayama, and Y. Naota,
Surf. Coat. Technol. **76-77**, 337 (1995).

[1.20] X. Wang, A. Kolitsch, F. Prokert, and W. Möller,
Surf. Coat. Technol. **103-104**, 334 (1998).

[1.21] C. R. Gorla, W. E. Mayo, S. Liang, and Y. Lu,
J. Appl. Phys. **87**, 3736 (2000).

[1.22] M. Kadota and T. Miura,
Jpn. J. Appl. Phys. **41**, 3281 (2002).

[1.23] K. Tominaga, Y. Sueyoshi, H. Imai, and M. Shirai,
Jpn. J. Appl. Phys. **31**, 3009 (1992).

[1.24] K. Tominaga, T. Kikuma, K. Kusaka, and T. Hanabusa,
Vacuum **66,** 279 (2002).

[1.25] D. C. Look,
Mater. Sci. Eng. B **80**, 383 (2001).

[1.26] R. Ruby, P. Bradley, J. D. Larson III and Y. Oshmyansky,
Electron. Lett. **35**, 794 (1999).

[1.27] M. Kadota,
Jpn. J. Appl. Phys. **44**, 4285 (2005).

[1.28] M. Benetti, D. Cannatà, F. Di Pietrantonio, V. Foglietti, and E. Verona,
Appl. Phys. Lett. **87**, 173504 (2005)

[1.29] S. Kumar, G. Kim, K. Sreenivas, and R.P. Tandom,
J. Electroceram. **22**, 198 (2009).

[1.30] X. Qiu, J. Zhu, J. Oiler, C. Yu, Z. Wang, and H. Yu,
Appl. Phys. Lett. **94**, 151917 (2009).

[1.31] J. B. Lee, J. P. Jung, M. H. Lee, and J. S. Park,
Thin solid films **447-448**, 610 (2004).

[1.32] K. M. Lakin,
IEEE Trans. Ultrason. Ferroelectr. Freq. Control **52**, 707 (2005).

[1.33] G. Wingqvist, J. Bjurström, L. Liljeholm, V. Yantchev, and I. Katardjiev,
Sens. Actuators B **123**, 466 (2007).

[1.34] K. Hashimoto, S. Sato, A. Teshigahara, T. Nakahara, and K. Kano,
IEEE Trans. Ultrason. Ferroelectr. Freq. Control **60**, 637 (2013).

[1.35] J. L. Bleustein,
Appl. Phys. Lett. **13**, 412 (1968).

[1.36] K. Nakamura, M. Kazumi, and H. Shimizu,
in *IEEE 1977 Ultrasonics Symp. Proc.*, Phoenix, Arizona, 26-28 October 1977, pp. 819-822.

[1.37] J. Kondoh, S. Hayashi and S. Shiokawa,
Jpn. J. Appl. Phys. **40**, 3713 (2001).

[1.38] R. M. White and S. W. Wenzel,
Appl. Phys. Lett. **52**, 1653 (1988).

2 SPUTTERING PROCESS [2.1]

2.1 SPUTTERING METHOD

When energetic particles bombard the surface of a solid (which is called the *target*), a series of collisions between atoms of the target occurs, resulting in the ejection of one of these atoms. This phenomenon is known as sputtering. Because ions can easily be accelerated by an electric field, they are normally used as the energetic particles which bombard the target surface. Figure 2.1 shows a schematic of a sputtering phenomenon. The sputtering process is very often compared to the break in a game of billiards. The bombarding ion strikes the atomic array of the target, and then the target atoms are scattered in all directions. Some of them are ejected from the target surface. A thin film can be grown by receiving these ejected atoms on a substrate surface.

In this section, both a conventional DC and RF sputtering system will be described as a practical deposition process.

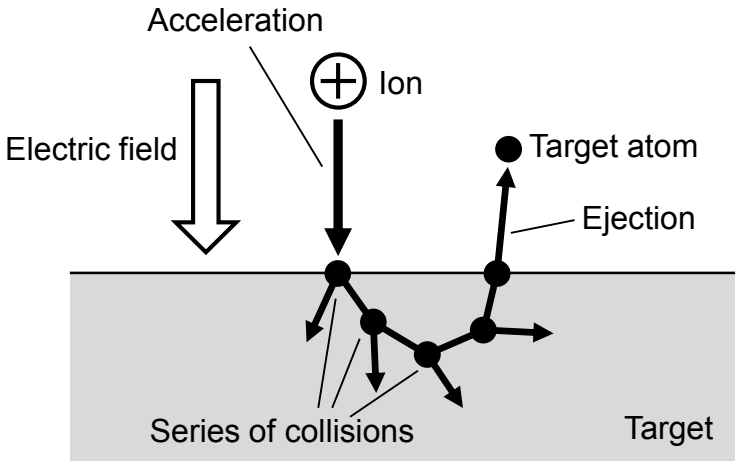

Fig. 2.1 Schematic of a sputtering phenomenon.

2.1.a DC SPUTTERING DEPOSITION

Figure 2.2 shows a conventional magnetron sputtering system. A sputtering deposition is performed in a vacuum chamber. A sputtering target is set on the cathode which is connected to a DC or RF power supply, and a substrate on the anode faces the target in the conventional system. A magnetron circuit is often included in the cathode. The effect of the magnetron will be introduced in Section 2.3. Gasses such as Ar and O_2 are introduced into the chamber to some specified pressure.

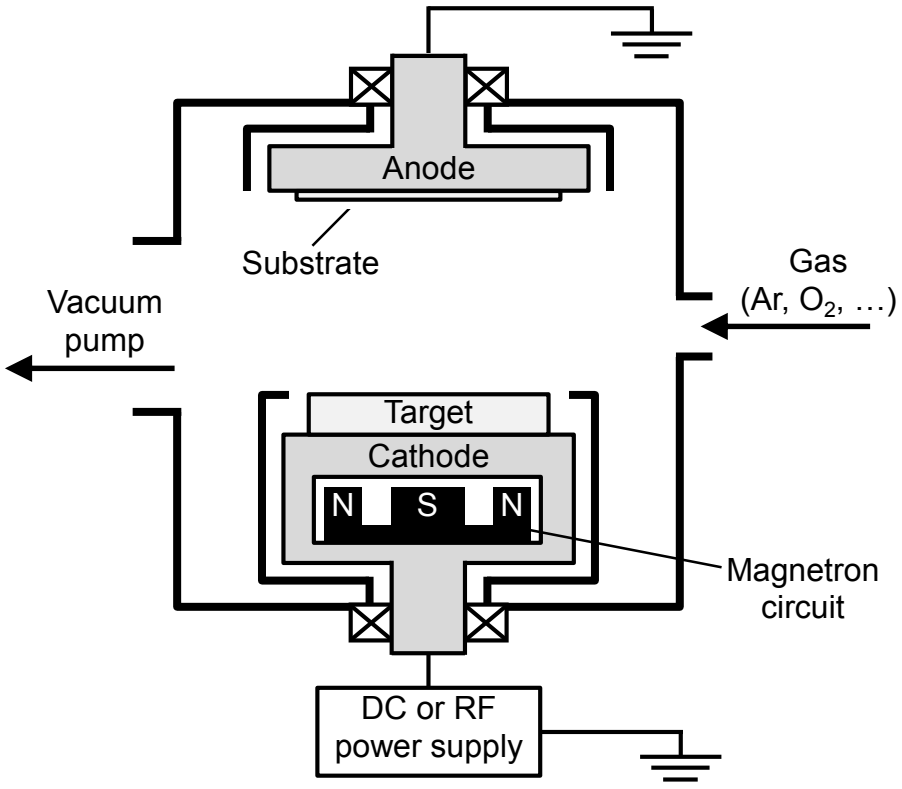

Fig. 2.2 Conventional sputtering system.

In a DC sputtering deposition, a high negative DC voltage is applied to the target. Electrons are accelerated by the DC electric field, and collide with gas atoms. The collision processes in the discharge can be broadly divided as follows:

- Elastic collision
- Inelastic collision
  - Ionization and recombination
  - Excitation and relaxation
  - Dissociation
  - Electron attachment

The most important process of these is ionization. An electron is removed from the atom by the electron collision, resulting in producing a positive ion and two electrons, e.g.

$$e + Ar \rightarrow 2e + Ar^{+}. \qquad (2.1)$$

This phenomenon is known as electron-impact ionization. Then, the two electrons are accelerated again, and collide with other gas atoms. On the other hand, the positive ion is accelerated toward the target. It recombines with an electron to form a neutral atom or bombard the target. When the ions bombard the target, the sputtering of the target atoms may occur, resulting in the deposition of the target material on the substrate. Secondary electrons may be also liberated from the target. They are accelerated by the electric field, which contribute further ionizations. Through these collision processes, both the discharge and deposition are sustained.

Excitations and relaxations also occur in the discharge. Transitions in the relaxation process are accompanied by the emission of a photon with very specific energy. Because of the photon emission, this discharge is called a *glow* discharge. The glow region where the ionization, recombination, excitation, and relaxation frequently occur keeps the charge neutral since these processes are always pairwise. The partially-ionized gas consisting of equal numbers of positive and negative charges is well known as plasma.

Ions and electrons in the plasma have different mass and temperature. Because the electrons has high temperature and low mass, the average speed of them is significantly higher than that of the ions. The rapid motion of the electrons means they can be easily lost by collision with the substrate (anode)

and wall of the chamber. Then, the spaces around the substrate and wall are positively charged, which is generally known as a space charge. It forms a *sheath* in the glow discharge plasma. Because of the space charge, the plasma has a relatively-positive potential to almost everything in the system (including the target of course). Ions are accelerated through the sheath voltage. It will be described in Section 2.2.

2.1.b RF SPUTTERING DEPOSITION

In the DC sputtering deposition of an electrically insulating material, when a negative voltage is applied to the insulating target, the potential of the insulating-target surface is negative. The negatively biased target are bombarded by positive ions, and charged positively (because it loses electrons as the ions are neutralized at its surface). Then, the potential of the target surface rises toward zero, resulting in the extinguishment of the discharge.

An RF sputtering deposition provides a significant advantage over the DC sputtering for the deposition of the insulating material. Figure 2.3 shows a RF power supply. A matching box is practically connected between the RF generator and the cathode. The main role of the matching box is to increase the power consumption in the discharge, and to protect the generator.

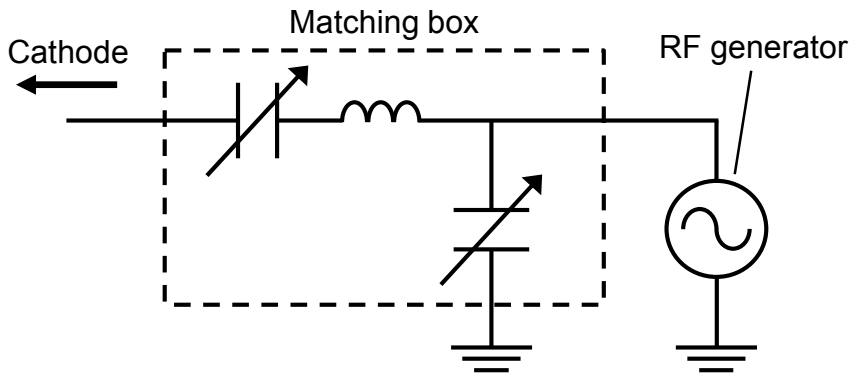

Fig. 2.3 RF power supply.

The series capacitor in the matching box plays an additional role as a blocking capacitor. It creates asymmetry in glow discharge systems [2.2]. Figure 2.4 shows an asymmetric discharge system with a blocking capacitor. Without the blocking capacitor, the sheath voltage V_1 and V_2 are equal to V_p. On the other hand, with the blocking capacitor (including the capacitor of the insulating target), the RF voltage is capacitively divided between two sheaths. The relation between V_1 and V_2 is given by

$$\frac{V_1}{V_2} = \left(\frac{A_2}{A_1} \right)^4 , \tag{2.2}$$

where A_1 and A_2 are areas of two electrode [2.2]. Equation (2.2) indicates that the larger voltage sheath appears at the smaller electrode. If the target is set on the smaller cathode, the target material can be sputtered effectively. Since the wall of the chamber is usually grounded as is the case with the anode, the anode area is much larger than the cathode area.

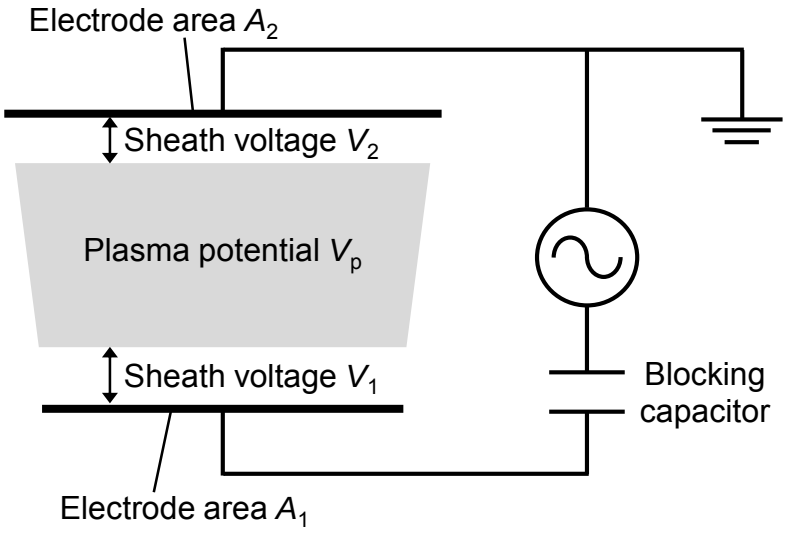

Fig. 2.4 Asymmetric discharge system with a blocking capacitor.

In the RF sputtering, the excitation frequency with 13.56 MHz is commonly used. Because the high mass of the ions prevent them moving far in the RF electric field, the electron current is much larger than the ion current in the target. The average voltage of the target V_T is a negative value, which is called a self-bias, as shown in Fig. 2.5 [2.3]. Since the target voltage V_{Tt} is positive for only a very short fraction of each cycle, they prevent the insulating-target surface charging up. On the other hand, the plasma potential V_{Pt} is always the highest value in the almost everything, as is the case of the DC glow discharge.

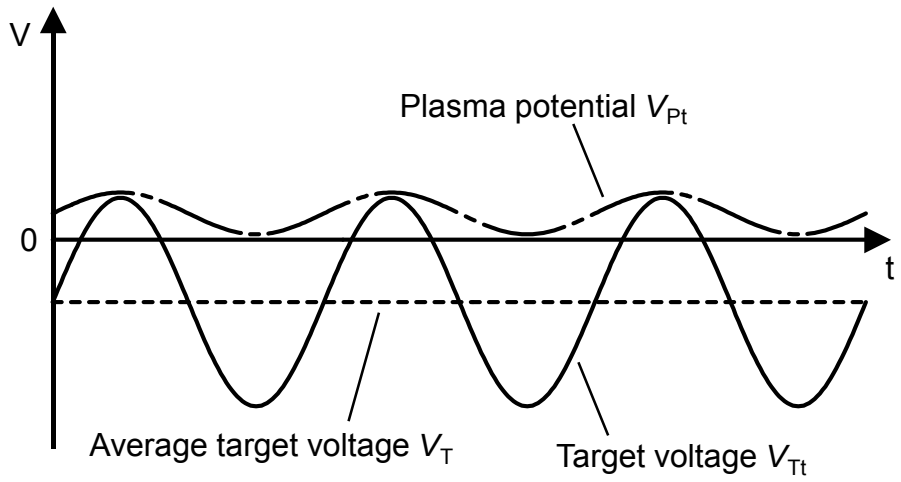

Fig. 2.5 Plasma potential and target voltage in the asymmetric system [2.3].

2.2 ION BOMBARDMENT

In the glow discharge process, sheaths are formed toward a target and substrate. Because Ions are accelerated or decelerated by the electric fields in the sheaths, the target and substrate are bombarded with the ions. It is well known that the ion bombardment to the substrate have an effect on the thin film growth [2.4-2.9].

Figure 2.6 shows an average-potential distribution in a conventional RF sputtering system. Positive ions in the plasma enter the sheath toward the

substrate with very low energy, and then they are accelerated through the potential difference between the plasma and target. This acceleration energy corresponds to small plasma potential (several tens of Volts [2.3, 2.10]) because the anode is grounded. Therefore, the positive ions enter the substrate with low energy.

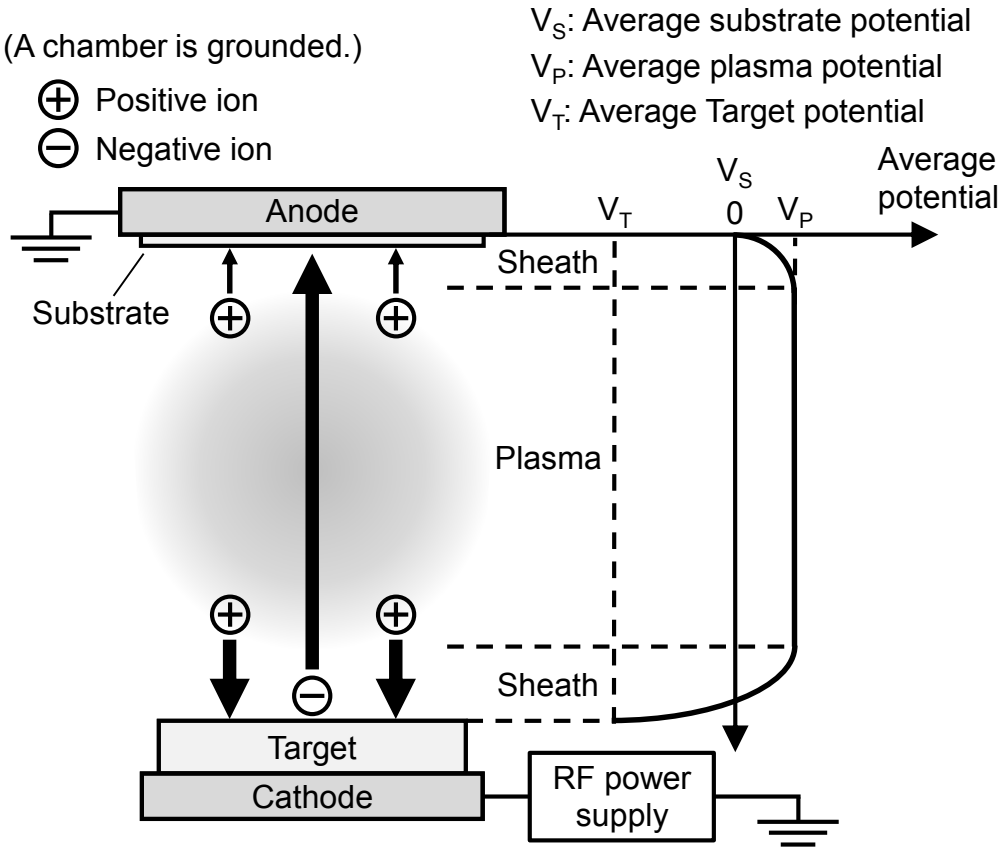

Fig. 2.6 Average-potential distribution in a conventional RF sputtering system.

Negative ion bombardments become an important problem in the oxide film deposition [2.8, 2.9]. Oxygen gas is usually introduced during the deposition. The collision process between the ion and electron includes dissociation, as described in Section 2.1a. The process of dissociation is the breaking apart of a molecule. In a glow discharge, the electron impact dissociation of oxygen is common:

$$e + O_2 \rightarrow e + O + O. \tag{2.3}$$

Because the oxygen atom has a high electron affinity (1.461 eV [2.11]), an electron can be attached to it:

$$e + O \rightarrow O^-. \tag{2.4}$$

This process is known as electron attachment. On the other hand, argon atoms have little or no tendency to form negative ions, because the outer electron shells of them are filled with electrons. Oxygen negative ions are also generated from the oxide target, when it is bombarded with positive ions which are accelerated through the sheath toward it. The negative ions generated near the target are greatly accelerated to the substrate by the negative voltage of the self-bias (Section 2.1a). Therefore, the substrate is bombarded with these highly-energetic negative ions. Many studies have reported the degradations of the crystalline orientation by the ion bombardment during the sputtering deposition [2.8, 2.9]. In this study, however, unusual crystal growths will be demonstrated by using the highly-energetic ions (Chapters 3 and 4).

2.3 MAGNETRON CIRCUIT

In sputtering systems, a magnetron circuit is usually used for the increase of sputtering rate, extension of operating pressure range, and reduction of electron bombardment at the substrate. If a magnetic field $\boldsymbol{B}$ is applied a particle of charge q and velocity $\boldsymbol{v}$, a Lorentz force is produced on the particle. In addition, the particle is also forced by an electric field $\boldsymbol{E}$. The total force $\boldsymbol{F}$ is given by

$$\boldsymbol{F} = q(\boldsymbol{v} \times \boldsymbol{B} + \boldsymbol{E}). \tag{2.5}$$

When a magnetic field which is parallel to the target surface is applied during the sputtering deposition, electrons ejected from the surface move in cycloidal orbits, as shown in Fig. 2.7. They are trapped near the target by the magnetic field. On the other hand, the ions are too massive to be affected by the magnetic field. Figure 2.8(a) shows a magnetic field with a magnetron circuit in the conventional magnetron sputtering system. A disc target and coaxial magnet are widely used in the system. The magnetic field is parallel to the target surface near the target and between the north and south magnetic poles. Electrons are trapped there, as shown in fig. 2.8(b), and the effect of electron-impact ionization is increased. Therefore, the sputtering deposition can be operated under the lower gas pressure, and the sputtering rate can be increased, although the target is locally eroded by the concentrated glow.

Another effect of the magnetron circuit is to induce ion bombardments to the substrate. A sputtering method using the effect is called an unbalanced magnetron sputtering [2.12, 2.13]. The magnetron circuit is designed so that its magnetic field can be also applied to the substrate as shown in fig. 2.8(a). Because electrons move to the substrate in helical orbit along the magnetic field, the Ionization of gas atoms is enhanced near the substrate. In this case, the substrate is bombarded by positive ions with not only high flux but also high energy because of increased plasma potential [2.13].

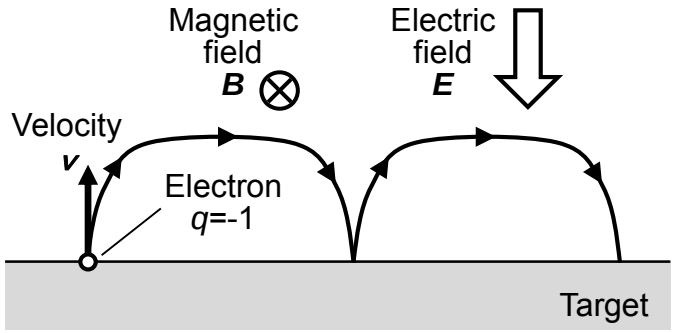

Fig. 2.7 Motion of an electron ejected from a target surface in a magnetic field and electric field. The magnetic field is parallel, and the electric field is orthogonal to the surface.

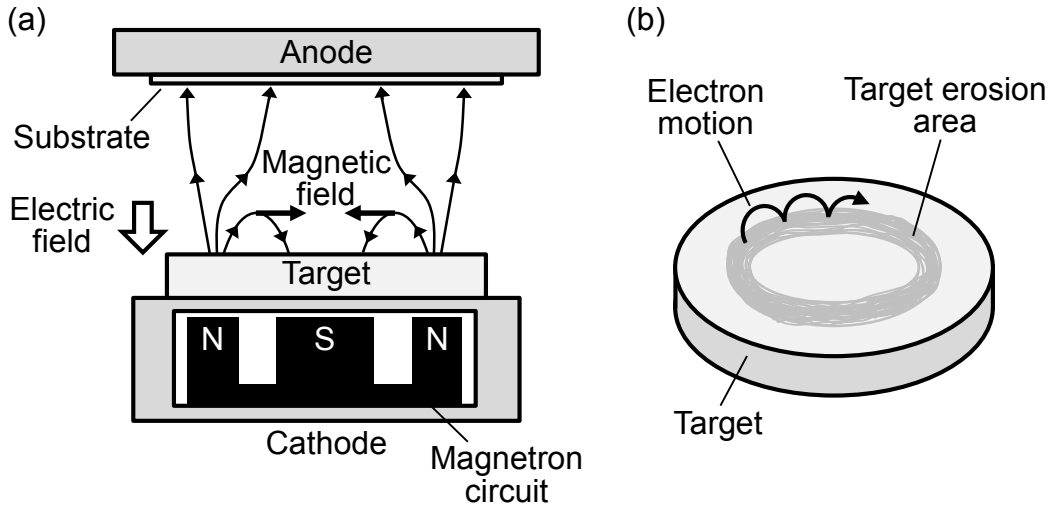

Fig. 2.8 (a) Magnetic field with a magnetron circuit in the conventional magnetron sputtering system, and (b) motion of an electron on a disc target.

REFERENCES

[2.1] B. Chapman,
Glow discharge processes (John Wiley & Sons, New York, 1980), p. 21.

[2.2] H. R. Koenig and L. I. Maissel,
IBM J. Res. Develop. **14**, 168 (1970).

[2.3] J. W. Coburn and E. Kay,
J. Appl. Phys. **43**, 4965 (1972).

[2.4] J. L. Vossen and J. J. O'Neill Jr.,
RCA Review **29**, 566 (1968).

[2.5] H. F. Winters and E. Kay,
J. Appl. Phys. **38**, 3928 (1968).

[2.6] J. L. Vossen,
J. Vac. Sci. Tech. **8**, S12 (1971).

[2.7] J. W. Patten and E. D. McClanahan,
J. Appl. Phys. **43**, 4811 (1972).

[2.8] K. Tominaga, Y. Sueyoshi, H. Imai, and M. Shirai,
Jpn. J. Appl. Phys. **31**, 3009 (1992).

[2.9] K. Tominaga, T. Kikuma, K. Kusaka, and T. Hanabusa,
Vacuum **66**, 279 (2002).

[2.10] K. Köhler, J. W. Coburn, D. E. Horne, E. Kay, and J. H. Keller,
J. Appl. Phys. **57**, 59 (1985).

[2.11] R. A. Kendall, T. H. Dunning Jr., and R. J. Harrison,
J. Chem. Phys. **96**, 6796 (1992).

[2.12] B. Window and N. Savvides,
J. Vac. Sci. Tech. A **4**, 196 (1986).

[2.13] B. Window and G. L. Harding,
J. Vac. Sci. Tech. A **10**, 3300 (1992).

3 UNUSUAL GROWTH OF ZnO INDUCED BY NEGATIVE ION BOMBARDMENT IN RF MAGNETRON SPUTTURING

3.1 UNUSUAL GROWTH OF ZnO

In general, ZnO films tend to grow in their most densely packed (0001) plane parallel to the substrate plane. However, the energetic particle bombardment during deposition suppresses the (0001)-oriented grain growth, resulting in the preferential development of $(11\bar{2}0)$ texture instead of the (0001) texture [3.1].

Yanagitani and Kiuchi have showed that $(11\bar{2}0)$ texture formation was observed under oxygen ion beam irradiation using ion beam sputtering [3.1, 3.2]. D. Köhl et al. have reported a suppression of the usual (0001) oriented grain growth by irradiation of high-energy O^+ ion beam set to 800 eV, resulting in a growth of both $(10\bar{1}0)$ and $(11\bar{2}0)$ preferred orientations [3.3]. On the other hand, Tominaga et al. reported that energetic particles such as O^- ions and O atoms are produced in the sputtering system facing sputtering targets. When the ZnO film was bombarded by these particles at lower gas pressures, the formation of (0001) textured film was disturbed severely [3.4]. Yanagitani et al. [3.5, 3.6] and Kawamoto et al. [3.7, 3.8] succeeded in $(11\bar{2}0)$ -oriented-film growth by RF magnetron sputtering without epitaxial techniques. However, the growth mechanism of $(11\bar{2}0)$ oriented ZnO in a planer RF magnetron sputtering system is still not clear.

In this chapter, the negative-ion-induced unusual crystalline growth of ZnO film will be demonstrated. Negative ions are generated on the target in an RF magnetron sputtering. The spatial distributions of the energy and flux of positive and negative ions entering the substrate will be measured and compared with the distribution of crystalline orientation of films.

3.2 EXPERIMENTAL METHODS

3.2.a ZnO FILM GROWTHS USING RF MAGNETRON SPUTTERING

ZnO films were grown using an RF magnetron sputtering apparatus as shown in Fig. 3.1. Pyrex glass (25 ×100 ×0.5 mm^3) was used as a substrate and ZnO ceramic (Furuuchi Chemical Co., 80 mm in diameter) was used as a oxide target on the cathode. Table I shows the deposition conditions. Total gas pressures were set to 1 or 0.1 Pa to investigate the effects of gas pressure on the crystalline orientation. It is predicted that the negative ion bombardment from the target increases under low gas pressure, because the mean free path of the gas molecules is long. In addition, the negative ion generation on the target is drastically enhanced by strong magnetic field of neodymium magnetron inside the cathode. The target erosion area (see Section 2.3) is at 25-35 mm from the anode (cathode) center. Thicknesses of the samples with 1 and 0.1 Pa were adjusted to be 3 μm at 30 mm from the anode center.

3.2.b EVALUATION METHOD OF CRYSTALLINE ORIENTATION

The crystalline orientations of the samples were measured by a 2θ–ω scan XRD pattern using an x-ray diffractometer (PANalytical, X-Pert Pro MRD). The degrees of (0001) and $(11\bar{2}0)$ oriented crystallizations of the samples were determined from the integrated intensities of (0002) and $(11\bar{2}0)$ XRD peaks, respectively. In addition, the degree of the $(11\bar{2}0)$ preferred orientation of the samples was measured from the full width at half maximum (FWHM) of the $(11\bar{2}0)$ plane ω-scan rocking curve. These measurements of the samples were performed at 0 to 50 mm from the anode center. In addition, 3-dimensional crystalline orientations of the $(11\bar{2}0)$ ZnO films were quantitatively evaluated by XRD pole figure analysis.

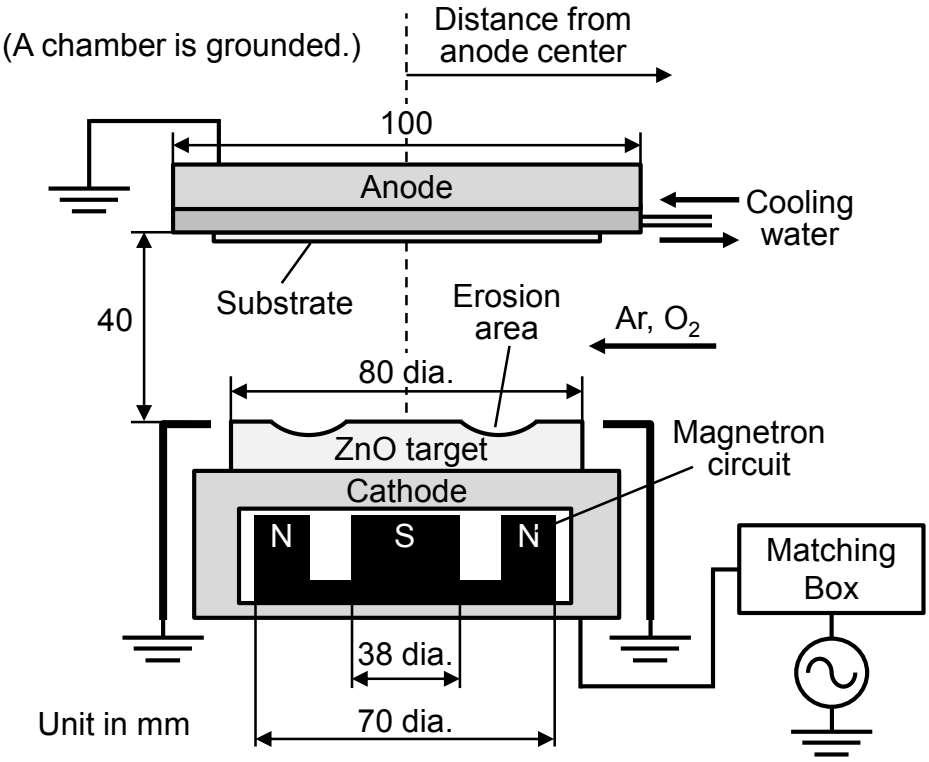

Fig. 3.1 RF magnetron sputtering apparatus.

Table 3.1 Deposition conditions in RF magnetron sputtering

Total gas pressure	0.1, 1.0 Pa
Ar / O_2	1 / 3
RF power	13.56 MHz, 50 W
Target-substrate distance	40 mm
Deposition time	15 hours

3.2.c MEASUREMENTS OF ENERGETIC ION BOMBARDMENT

During the sputtering deposition, gas molecules are positively ionized. These positive ions are accelerated toward the substrate by the ion sheath voltage near the substrate. Negative ions generated near the target are accelerated to the substrate by the target ion sheath and bombard the substrate

surface. This negative ion bombardment leads texture modification of ZnO film [3.4].

The distributions of the ion energy and the amount of ion flux in the anode plane during the depositions were measured by electrostatic energy analyzer with quadrupole mass spectrometer (PSM003, Hiden Analytical) as shown in Fig. 3.2. The discharge conditions for the measurement and the film growth were set to be same. The PSM003 Probe is mounted in a differentially pumped housing fitted with a cover tube that incorporates an orifice plate. It comprises the following items [3.9]:

- An ion extraction system.
- A fully-adjustable electron-impact ion source for residual gas analysis (RGA) of neutrals and radicals.
- A Bessel box energy filter.
- A triple-section quadrupole mass filter for mass-to-charge ratio analysis.
- A ditector.

The detector is an ion counting secondary electron multiplier which counts the number of ions striking it per second. The RF head mounts directly on the Probe vacuum feedthrough. It contains the RF generator circuits and the detector amplifier/discriminator.

The effects of sputtering gas pressures and species on the ion energy and the amount of ion bombardment were measured. Before the measurements, the species of positive and negative ions which enter the substrate were identified by a mass spectrometry. Figure 3.3 shows mass spectra of positive and negative ions under bombarding the substrate in 1 and 0.1 Pa, respectively. Strong O_2^+ and Ar^+ peaks were observed in mass spectra of positive ions [Figs. 3.3(a) and (c)], and strong O^- peak were observed in that of negative ions [Figs. 3.3(b) and (d)] at both 1 and 0.1 Pa. Therefore, the ion energy distributions of O_2^+ positive and O^- negative ions were focused. In addition, to confirm the generation of the negative ions from the oxide target, mass spectra and energy distributions of the ions during pure argon discharge in 0.1 Pa were also investigated.

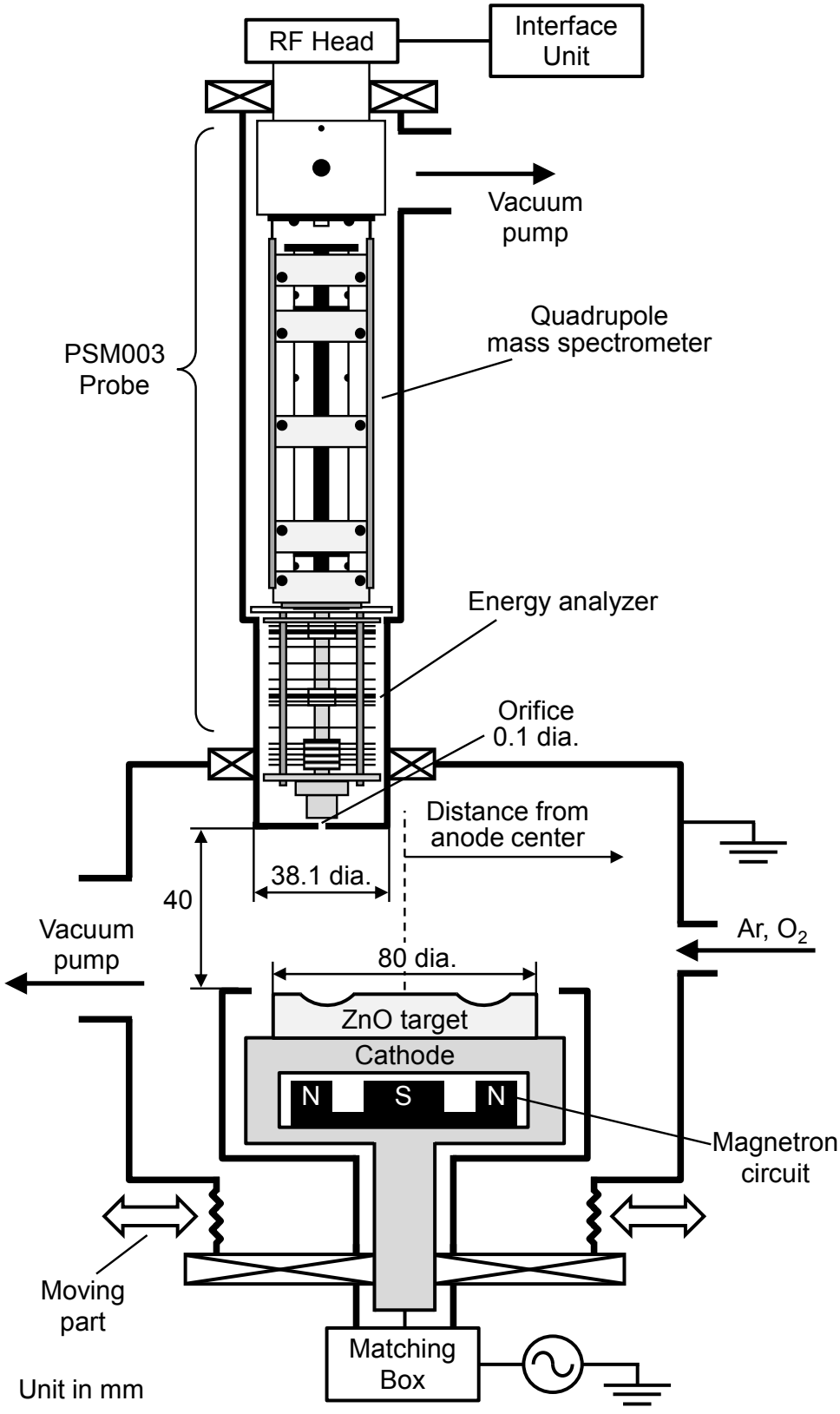

Fig. 3.2 Measurement system for the spatial distributions of the amount of ion flux and the ion energy in the RF magnetron sputtering.

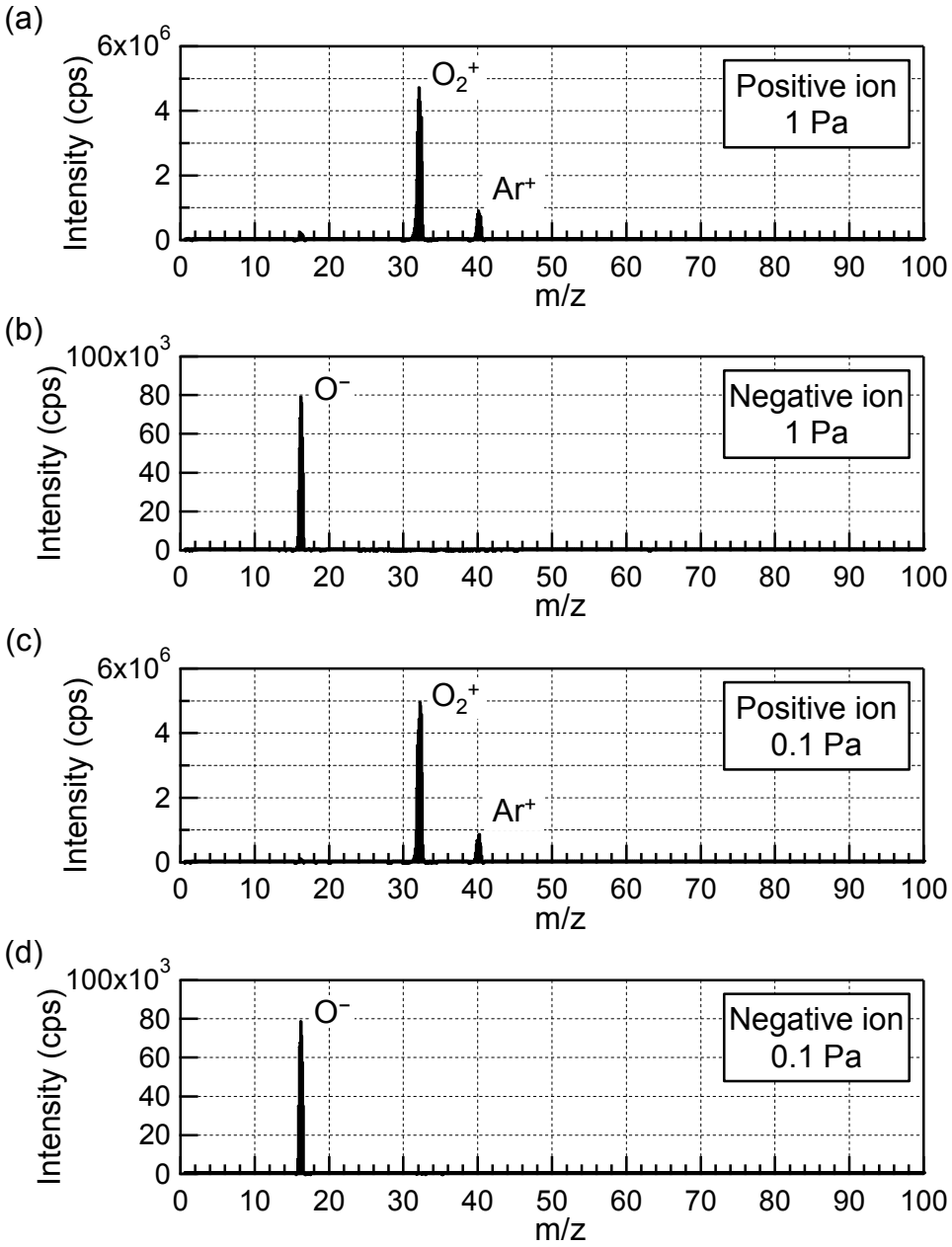

Fig. 3.3 Mass spectra of (a) positive ions and (b) negative ions bombarding the substrate in 1 Pa, and that of (c) positive ions and (d) negative ions in 0.1 Pa.

3.3 RESULTS AND DISCUSSIONS

3.3.a CRYSTALLIZATIONS OF THE ZnO SAMPLES

Figures 3.4(a) and (b) shows XRD patterns of the ZnO film samples grown in 1 and 0.1 Pa, respectively. Intense (0002) peaks were observed in the case

of 1 Pa. On the other hand, the unusual $(11\bar{2}0)$ preferred orientation was appeared in low gas pressure of 0.1 Pa. Figures 3.5(a) and (b) show the integrated intensities of (0002) and $(11\bar{2}0)$ XRD peaks of the samples with 1 and 0.1 Pa, respectively. Wurtzite ZnO films tend to grow in their most densely packed (0001) plane parallel to the substrate plane [3.10]. The (0002) integrated intensity was observed near the anode center at 1 Pa, but the (0002) peak was not observed at all measurement positions at 0.1 Pa. Instead of the (0002) peak, the high $(11\bar{2}0)$ intensity was found at 0.1 Pa, especially around the target erosion area (at 25-35 mm from the anode center).

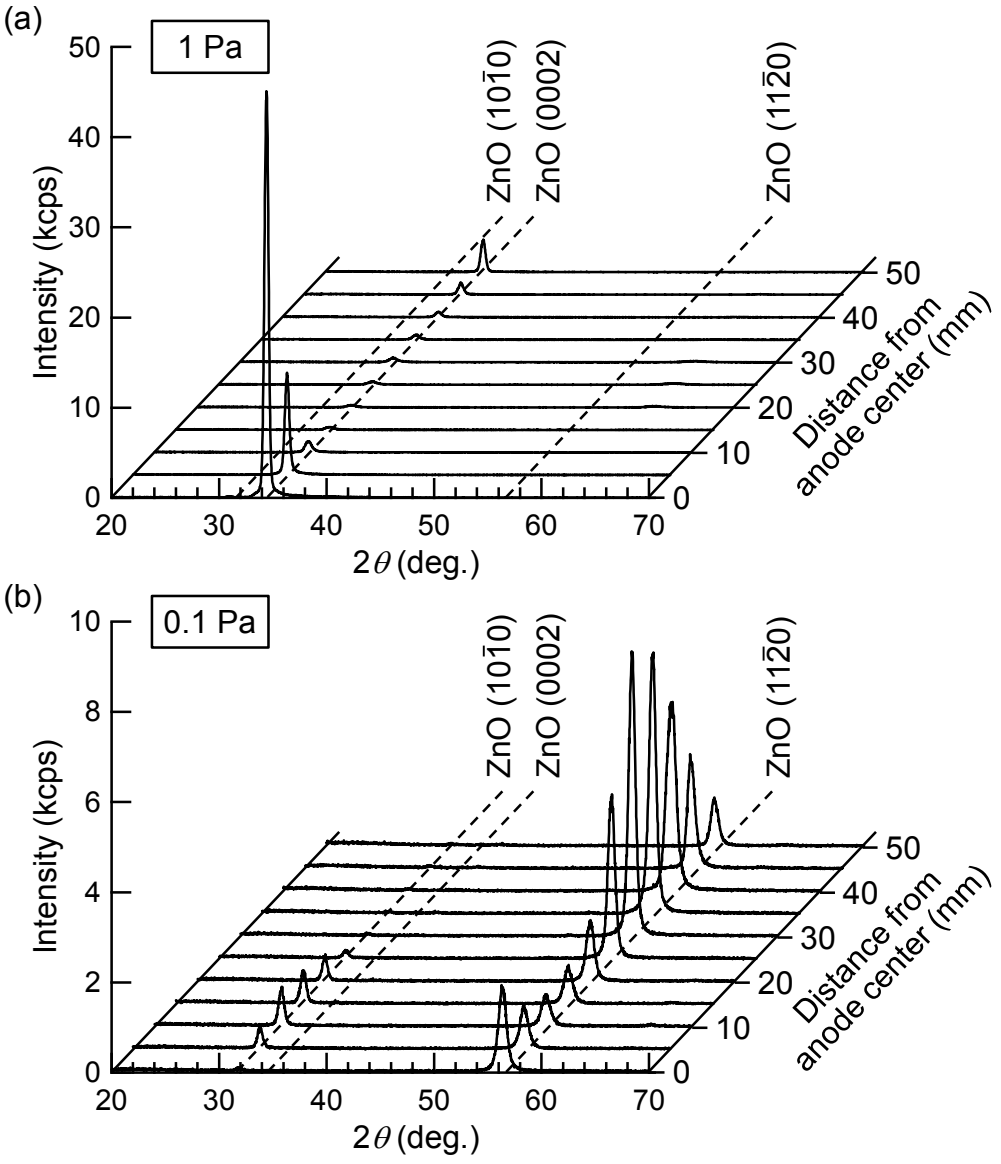

Fig. 3.4 XRD patterns of the samples grown in (a) 1 Pa and (b) 0.1 Pa.

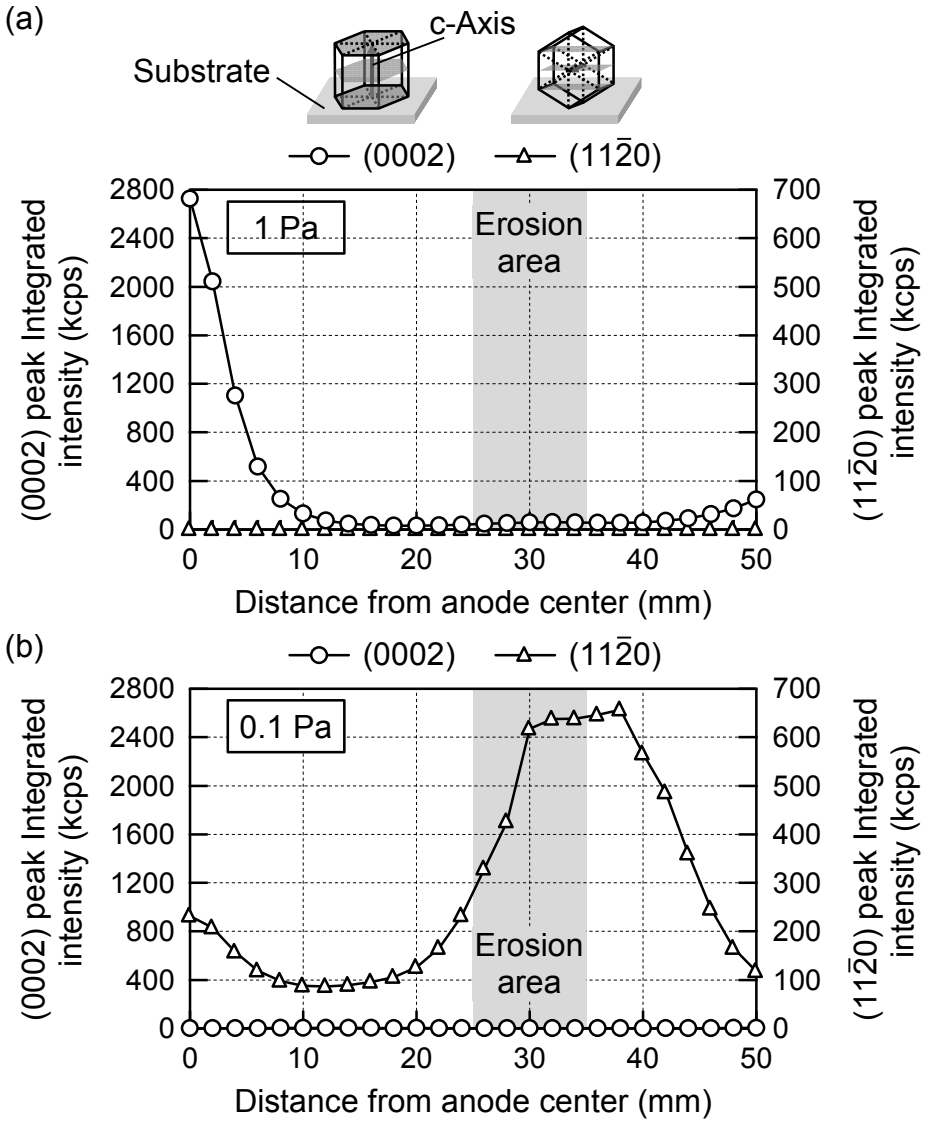

Fig. 3.5 Integrated intensities of (0002) and (11$\bar{2}$0) XRD peaks of the samples with (a) 1 Pa and (b) 0.1 Pa

3.3.b ENERGY AND FLUX OF IONS BOMBARDING THE SUBSTRATE

Figures 3.6(a) and (b) show the amount of ion flux and the ion energy of O_2^+ positive ions entering the substrate as functions of the distance from anode center at 1 Pa and 0.1 Pa, respectively. O_2^+ positive ions had large flux but had low ion energy (5-40 eV), and a similar result was observed in Ar^+ positive ion. A large amount of gas molecules are positively ionized during the discharge and these positive ions near the substrate bombard the substrate.

The difference between the anode potential and the plasma potential corresponds to the acceleration energy of positive ions bombarding the substrate. In this case, this energy corresponds to small plasma potential because anode (or energy analyzer) was grounded. Therefore, positive ions were little accelerated toward the substrate.

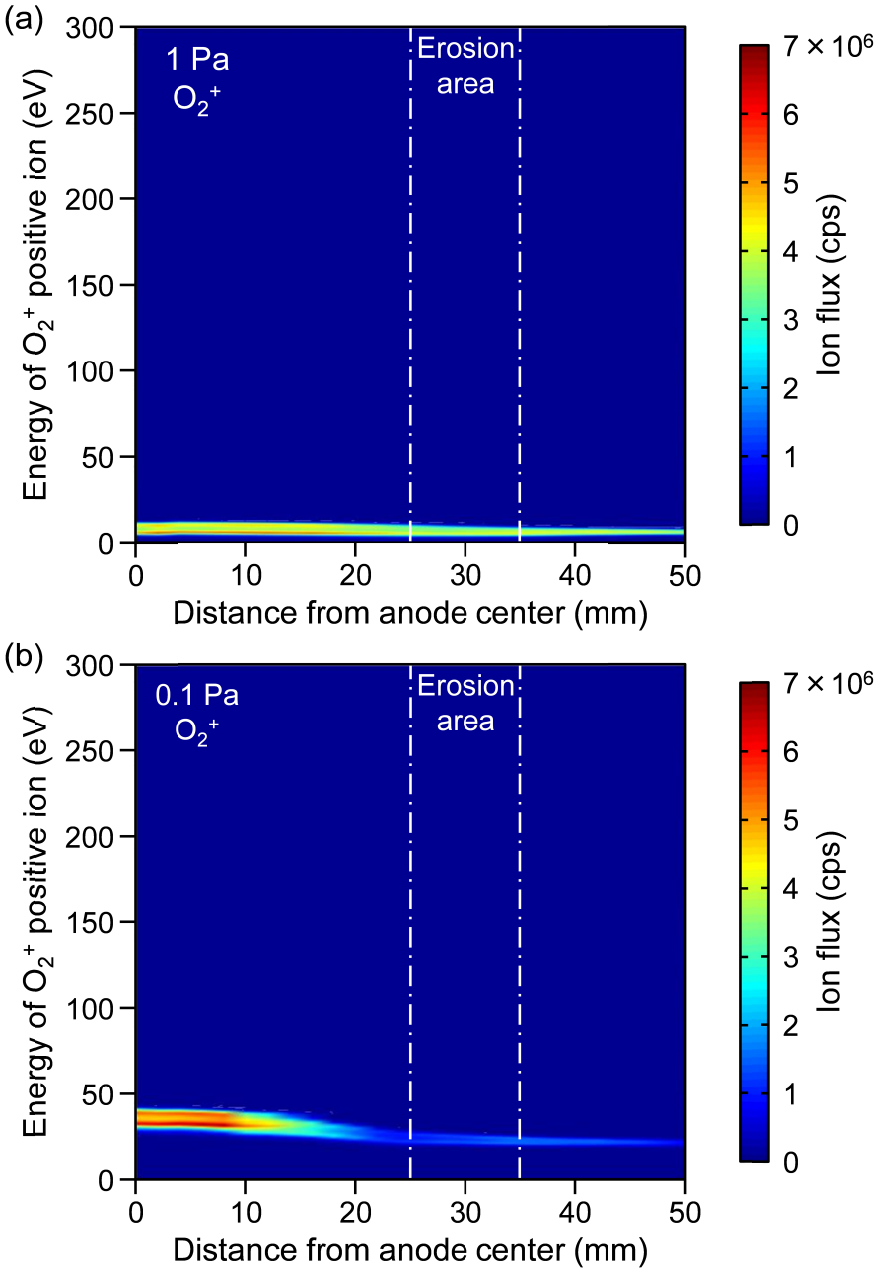

Fig. 3.6 Amount of ion flux and ion energy of O_2^+ positive ions as functions of the distance from anode center at (a) 1 Pa and (b) 0.1 Pa.

Figs. 3.7(a) and (b) show the distribution of O^- negative ions at 1 Pa and 0.1 Pa, respectively. O^- negative ions had small flux but had high energy (170-250 eV). Negative ions generating near the oxide target are greatly accelerated to the substrate by the negative bias at the target, and these energetic O^- bombarded the substrate.

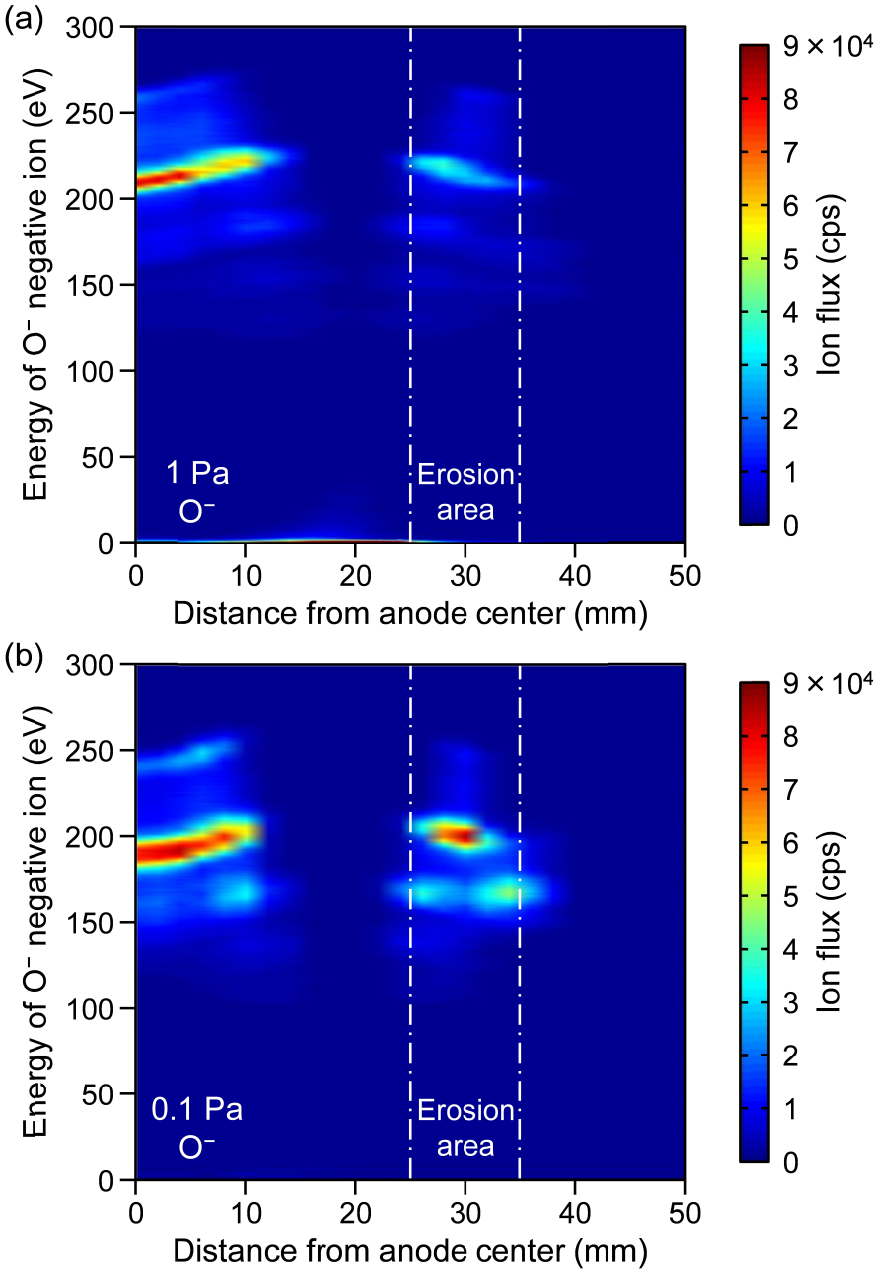

Fig. 3.7 Amount of ion flux and ion energy of O^- negative ions as functions of the distance from anode center at (a) 1 Pa and (b) 0.1 Pa.

The amounts of O_2^+ flux in 0.1 Pa were larger than that in 1 Pa by comparing Fig. 3.6 with Fig. 3.7, as expected. In the unbalanced magnetron sputtering, electrons move to the substrate along the magnetic field, and then a lot of gas molecules are ionized near the substrate, especially under the low gas pressure [3.11]. The plasma potential is also increased with increased sheath voltage between the plasma and substrate. Therefore, the energy of O_2^+ ions in 0.1 Pa was about 20 eV higher than that in 1 Pa. On the other hand, the energy of O^- negative ions was decreased. This result indicates that the target potential was increased by increased plasma potential in order to keep the target sheath voltage constant. The amounts of O^- flux decreased with distance from the anode center at both 1 Pa and 0.1 Pa, but interestingly, highly energetic O^- ions were observed above the target erosion area at 0.1 Pa.

In addition, to confirm the origin of the O^- negative ions, mass spectra of positive and negative ions during pure argon discharge in 0.1 Pa were also investigated, as shown Fig 3.8(a) and 3.8(b). Strong Ar^+ peak was observed as expected, but O_2^+ positive ion was not generated because oxygen gas molecules did not exist. On the other hand, although the intensity of O^- peak decreased to a quarter of that in argon-oxygen atmosphere, O^- negative ions were generated in pure argon atmosphere. Figure 3.8(c) shows the distributions of the energy and flux of these O^- negative ions. They had high energy (200 eV) on the target erosion area where a large amount of electrons are trapped by magnetic field and positive ions hit by the negative bias. These results indicate that a part of O^- negative ions were generated from the oxide target during the sputtering deposition of oxide films. They were greatly accelerated to the substrate by the negative bias at the target, and these energetic O^- bombarded the substrate, especially under the low gas pressure where the mean free path of the gas molecules is long.

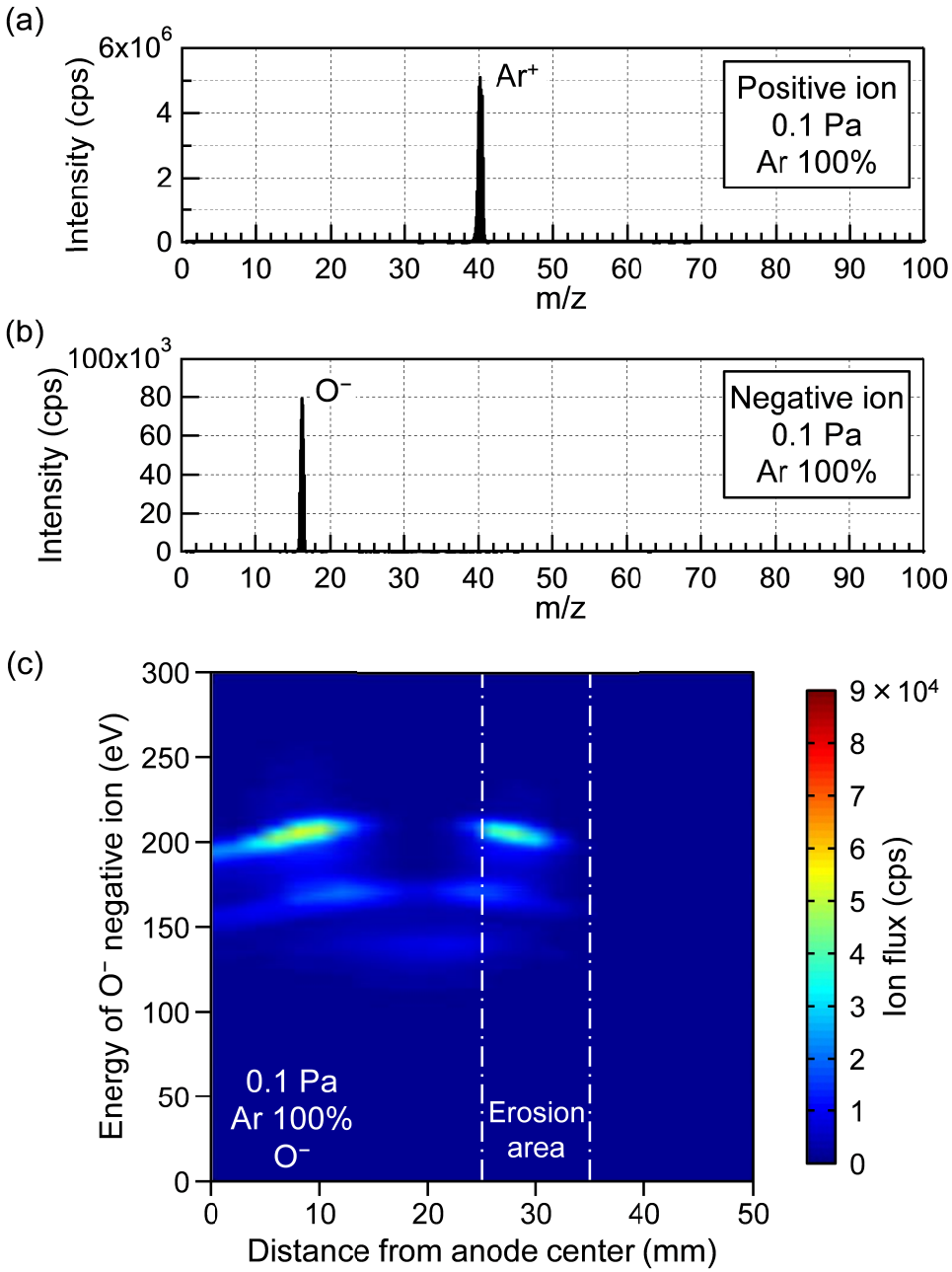

Fig. 3.8 Mass spectra of (a) positive ions and (b) negative ions bombarding the substrate. (c) the amount of ion flux as functions of the distance from anode center and the ion energy of O^- negative ions during pure argon discharge in 0.1 Pa.

3.3.c Effect of ion bombardment during deposition on unusual crystal growth in ZnO films

Table 3.2 shows a summary of distributions of the positive and negative ion bombardment and the $(11\bar{2}0)$ crystalline orientations under 0.1 Pa. A comparison of the spatial distribution of the amount of ion flux (Figs. 3.6 and 3.7) in the anode plane with the crystalline orientations on the anode plane in (Fig. 3.5) shows that large amounts of energetic O^- bombardment induced the unusual $(11\bar{2}0)$ preferred orientation in the ZnO film. The energetic O_2^+ positive ion bombardment was not observed on the target erosion area where the highly-crystallized $(11\bar{2}0)$ ZnO film was obtained at 0.1 Pa. On the other hand, the amount of the energetic O^- negative ion bombardment and the degree of crystallization in unusual $(11\bar{2}0)$ ZnO drastically increased on the target erosion area with decreased the gas pressure from 1 Pa to 0.1 Pa. This unusual crystalline growth is probably due to the deference of damage tolerance by ion sputter yield anisotropy in the ZnO crystal. The grain growth in the close-packed (0001) plane is more ion collision damage than that in the $(11\bar{2}0)$ direction, resulting in the preferential development of the unusual $(11\bar{2}0)$ orientation.

Table 3.2 Summary of distributions of the ion bombardment and the crystalline orientation under 0.1 Pa

	Distance from anode center		Target erosion area
	Short	Long	
Positive ion bombardment	Large amount Low energy	Small amount Low energy	Small amount Low energy
Negative ion bombardment	Small amount High energy	Very small amount	Small amount High energy
$(11\bar{2}0)$ orientation	Slightly crystallized	Non crystallized	Highly crystallized

Degrees of these $(11\bar{2}0)$ orientations were estimated from the full width at half maximum (FWHM) of the $(11\bar{2}0)$ plane ω-scan rocking curve, as shown in Fig. 3.9. FWHM values were small on the target erosion area, as expected. These results indicate that highly-crystallized and highly-oriented $(11\bar{2}0)$ ZnO film grew on the cathode erosion area under the low gas pressure. However, the $(11\bar{2}0)$ crystalline orientation was not good at the anode center in spite of enough both O_2^+ positive and O^- negative ion bombardment in this area. One possible explanation is the direction of ion bombardment to the substrate. At the anode center, ions bombard to the substrate from random directions. Therefore, the crystalline c-axis orients randomly in the substrate plane [3.8].

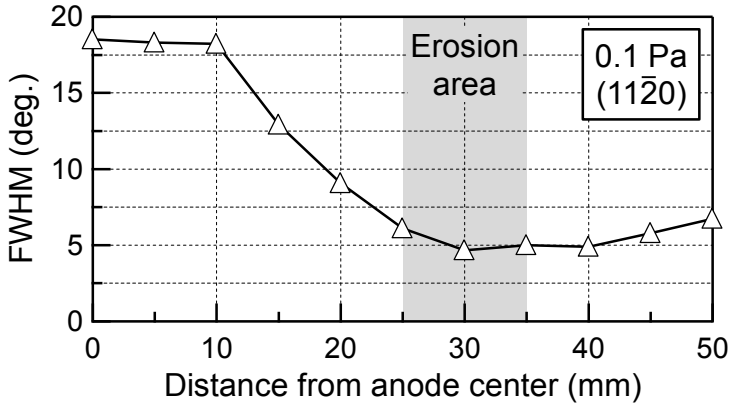

Fig. 3.9 FWHM values of ω-rocking curves of the sample with 0.1 Pa.

3-dimensional crystalline orientation of the $(11\bar{2}0)$ ZnO film with 0.1 Pa was quantitatively evaluated by XRD pole figure analysis. Fig. 3.10 shows the $(11\bar{2}2)$ pole figures measured at 30 mm from the anode center. In a pole figure, intensities are contour plotted with rotating sample plane in out-of plane direction (ψ-scan) and in-plane direction (ϕ-scan). In a $(11\bar{2}0)$ oriented film, a $(11\bar{2}2)$ pole figure should indicate $\{11\bar{2}2\}$ poles diffracted from the $(11\bar{2}0)$ oriented grain at ψ=32º because the angle between the $(11\bar{2}0)$ and $(11\bar{2}2)$ planes in a ZnO crystal is 32º. Two highly concentrated $\{11\bar{2}2\}$ poles were

found near ψ=32°, ϕ=90° and ψ=32°, ϕ=270° diffracted from the (11$\bar{2}$0) -oriented grain, indicating that the crystalline c-axis was both oriented parallel to the film plane and aligned unidirectionally in the film plane. c-axis direction can be determined by ϕ-angle where poles appear. The c-axis direction in the sample plane corresponds to the radial direction of the anode (or the cathode). These results reveal that crystal grains in the ZnO film with 0.1 Pa on the target erosion area aligned in both out-of-plane and in-plane direction (biaxial texture).

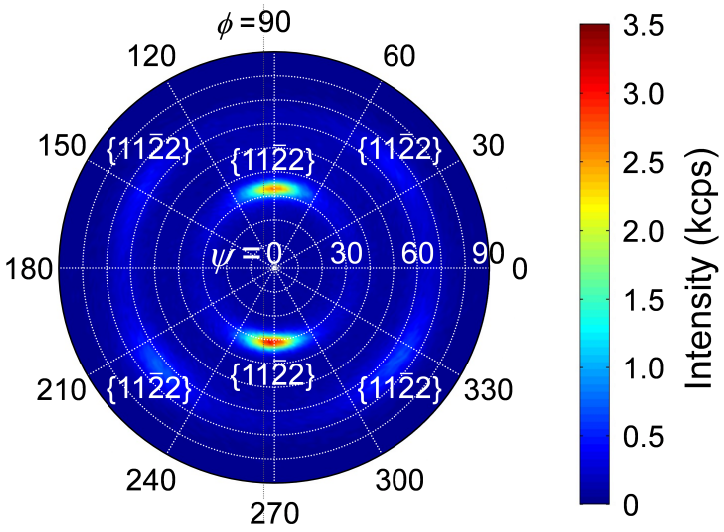

Fig. 3.10 (11$\bar{2}$2) pole figure of the sample with 0.1 Pa, measured at 30 mm from the anode center.

In conclusion, highly crystallized (11$\bar{2}$0) orientation was observed above the target erosion area where highly energetic O^- ions bombard under the low gas pressure condition. This ion bombardment technique is promising for the unusual crystalline growth of various oxide films.

REFERENCES

[3.1] T. Yanagitani and M. Kiuchi,
J. Appl. Phys. **102**, 044115 (2007).

[3.2] T. Yanagitani and M. Kiuchi,
Surf. Coat. Technol. **206**, 816 (2011).

[3.3] D. Köhl, G. Natarajan, and M. Wuttig,
J. Phys. D: Appl. Phys. **45**, 245302 (2012).

[3.4] K. Tominaga, Y. Sueyoshi, H. Imai, and M. Shirai,
Jpn. J. Appl. Phys. **31**, 3009 (1992).

[3.5] T. Yanagitani, M. Matsukawa, Y. Watanabe, and T. Otani,
J. Cryst. Growth **276**, 424 (2005).

[3.6] T. Yanagitani, M. Kiuchi, M. Matsukawa, and Y. Watanabe,
J. Appl. Phys. **102**, 024110 (2007).

[3.7] T. Kawamoto, T. Yanagitani, M. Matsukawa, and Y. Watanabe,
Jpn. J. Appl. Phys. **46**, 4660 (2007).

[3.8] T. Kawamoto, T. Yanagitani, M. Matsukawa, Y. Watanabe, Y. Mori, S. Sasaki, and M. Oba,
Jpn. J. Appl. Phys. **49**, 07HD16 (2010).

[3.9] In *PSM033 user's manual* (Hiden Analytical, England, 2005), p. 1-5

[3.10] N. Fujimura, T. Nishihara, S. Goto, J. Xu, and T. Ito,
J. Cryst. Growth **130**, 269 (1993).

[3.11] B. Window and G. L. Harding,
J. Vac. Sci. Tech. A **10**, 3300 (1992).

4 ORIENTATION CONTROL OF HEXIAGONAL FILMS BY POSITIVE ION BOMBARDMENT USING RF SUBSTRATE BIAS SPUTTERING

4.1 SUBSTRATE BIAS SPUTTERING

In Chapter 3, the unusual $(11\bar{2}0)$ oriented ZnO film was induced by the negative ion bombardment under low gas pressure (0.1 Pa) during RF magnetron sputtering deposition. However, instability of discharge and the limitation of deposition conditions should be serious problems. Simple and easy method is required for unusual $(10\bar{1}0)$ or $(11\bar{2}0)$ film growths.

In this chapter, RF substrate bias RF magnetron sputtering method will be demonstrated. It is difficult to control the motion of neutral particles, but ions can be controlled by applying the local electric field. Another DC or RF supply is connected to the substrate to induce the ion bombardment in this method. The substrate bias techniques have been used for the control of film properties as follows:

- Resistivity [4.1]
- Dielectric property [4.2]
- Hardness [4.3]
- Incorporation of sputtering gas [4.4]

If the highly-energetic ion bombardment is induced by the substrate bias, the unusual crystal growth and orientation control would be expected. In this section, the conditions of the ion bombardment in the DC or RF bias sputtering will be introduced.

4.1.a NO-BIAS CONDITION

The difference between the substrate potential and the plasma potential corresponds to the acceleration energy of positive ions which bombard the substrate (see Chapter 2). In this case, this energy corresponds to small plasma potential because the substrate electrode is grounded. Therefore, positive ions are little accelerated toward the substrate. On the other hand, high-speed negative ions from the target bombard the substrate. These energy distributions of the ions were shown in Chapter 3. The positive ions have low ion energy of 5-40 eV and large flux, whereas negative ions from the target have high energy of 170-250 eV but small flux.

4.1.b POSITIVE-DC-BIAS CONDITION

Figure 4.1(a) shows an average-potential distribution in a positive-DC-bias sputtering system. The plasma potential increases rapidly with the applied positive-DC-bias voltage [4.5], and the substrate potential can be made slightly positive toward the plasma potential. It is limited by an amount equal to the ionization potential of the sputtering gas [4.6].Therefore, positive ion bombardment to the substrate is very weak and very small. On the other hand, the target potential is also increased to keep the plasma-target sheath voltage [4.5]. Therefore, the difference between the target and substrate potentials is little changed. As a result, the negative ion bombardment to the substrate is similar to the non-bias condition.

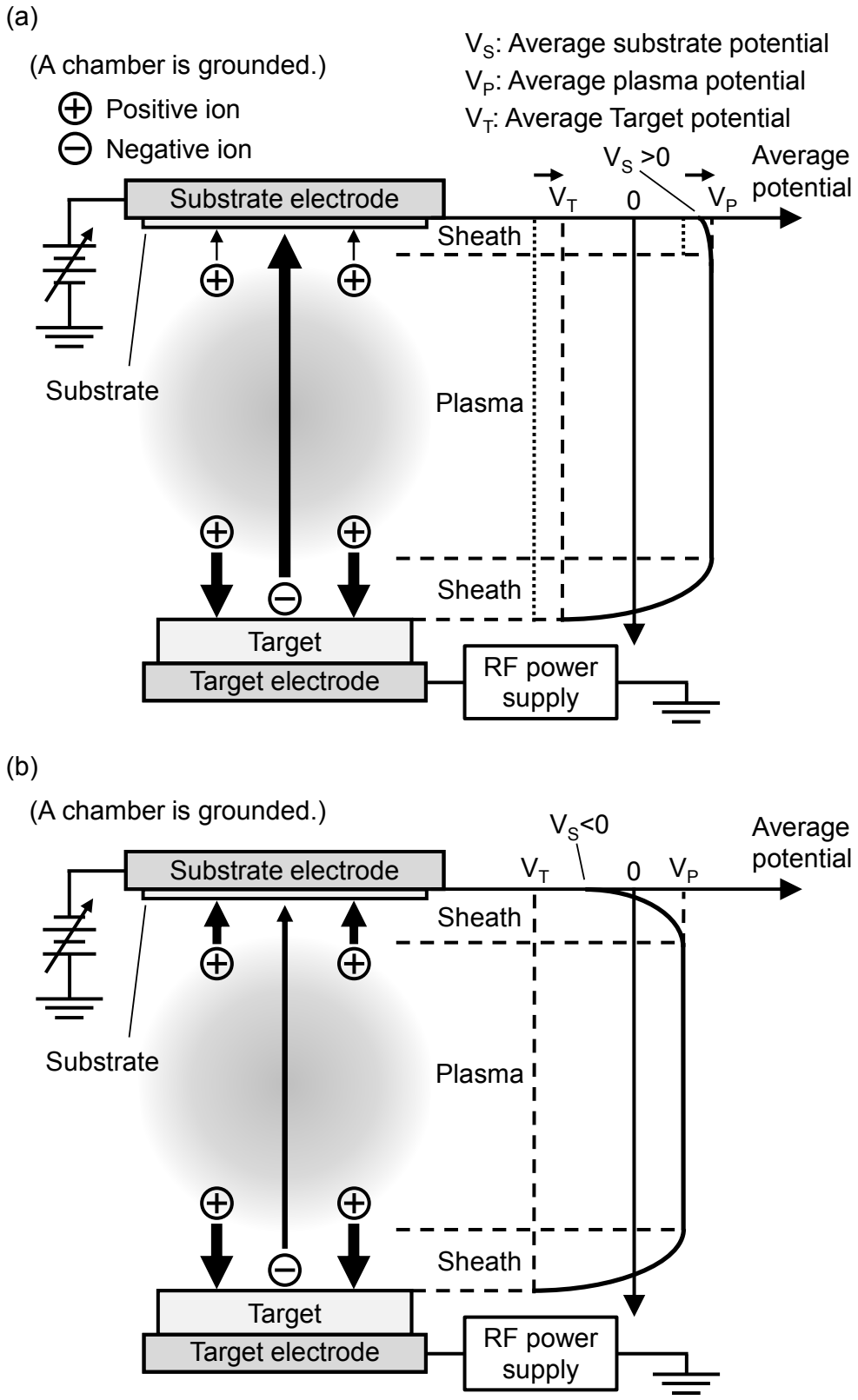

Fig. 4.1 Average-potential distribution in a (a) positive-DC-bias sputtering system and (b) negative-DC-bias sputtering.

4.1.c NEGATIVE-DC-BIAS CONDITION

Figure 4.1(b) shows an average-potential distribution in a negative-DC-bias sputtering system. The substrate potential turns to negative without the change of plasma potential because the wall of the chamber is usually grounded. The difference between the substrate potential and the plasma potential increases, and positive ions are greatly accelerated toward the substrate. In contrast, high-speed negative ions from the target are decelerated.

4.1.d RF-BIAS CONDITION

Figure 4.2 shows an average-potential distribution in a RF-bias sputtering system. The substrate potential becomes negative due to the RF self-bias without change of positive plasma potential. Positive ions are then greatly accelerated toward the substrate as well as negative DC bias condition. In addition, gas molecules around the substrate are positively ionized by RF bias in this case. The amounts of positive ion bombardment to the substrate are therefore larger than those in the negative bias condition.

The expected conditions of ion bombardment to the substrate are summarized in Table 4.1. The negative DC bias and RF bias are suitable for the induction of the highly-energetic ion bombardment. However, as described in Chapter 2, insulating materials are charged up in the DC glow discharge, and then the DC negative bias has no effect. In this study, because insulating glass substrates are used, the RF-substrate-bias RF sputtering is the most promising in these bias methods.

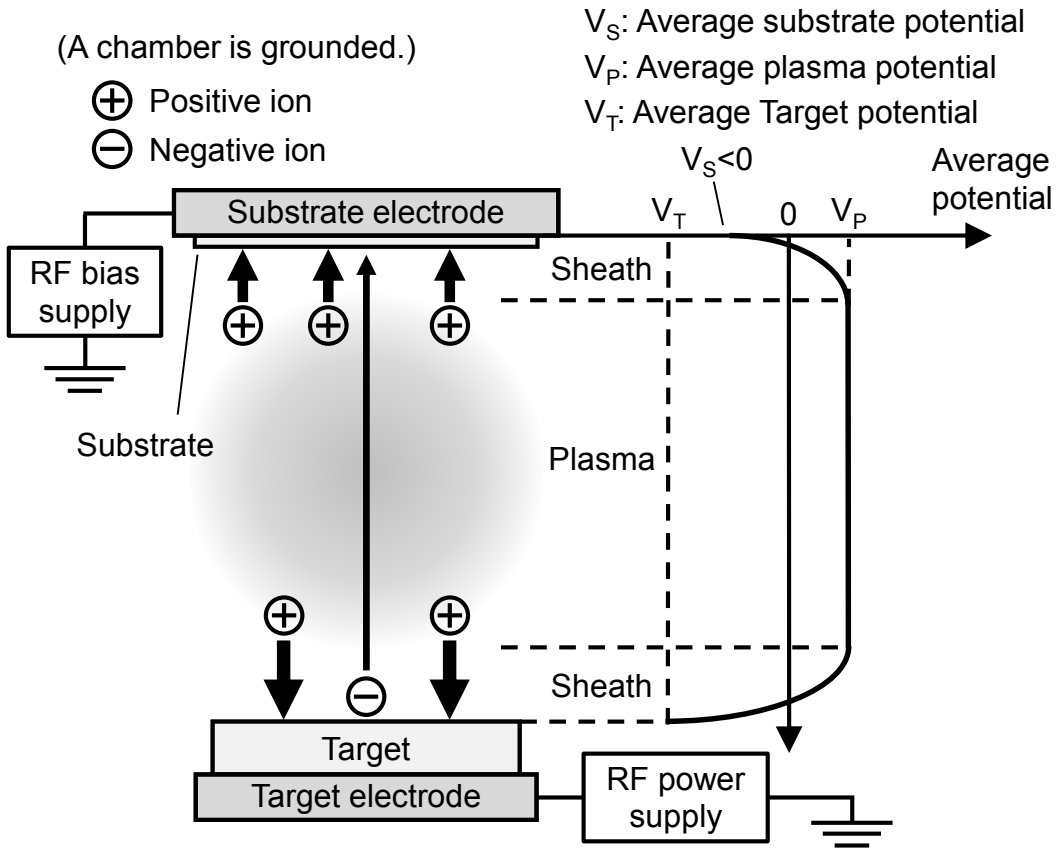

Fig. 4.2 Average-potential distribution in an RF-bias sputtering.

Table 4.1 Expected conditions of ion bombardment to the substrate

	Positive ion	Negative ion
No bias	Large amount Low energy	Small amount High energy
Positive DC bias	Very small amount Very low energy	Small amount High energy
Negative DC bias	Large amount High energy	Very Small amount Low energy
RF bias	Very large amount High energy	Very Small amount Low energy

4.2 ORIENTATION CONTROL OF ZnO FILM USING RF-SUBSTRATE-BIAS SPUTTERING

4.2.a EXPERIMENTAL METHODS

Figure 4.3 shows an RF-bias sputtering system. RF power supply is connected to the target electrode and substrate electrode. Silica glass (25 ×100 ×0.5 mm^3) with evaporated aluminum electrode layer was used as a substrate. ZnO ceramic (Furuuchi Chemical Co. 80 mm in diameter)) were used as a sputtering target. Table 4.2 shows the deposition conditions. ZnO film samples were prepared in 2 MHz-bias conditions. In the deposition conditions, the unusual crystal growth cannot be induced without use of bias technique because of high gas pressure (see Chapter 3). The crystalline orientations in the samples were observed by using an x-ray diffractometer (PANalytical, X-Pert Pro MRD).

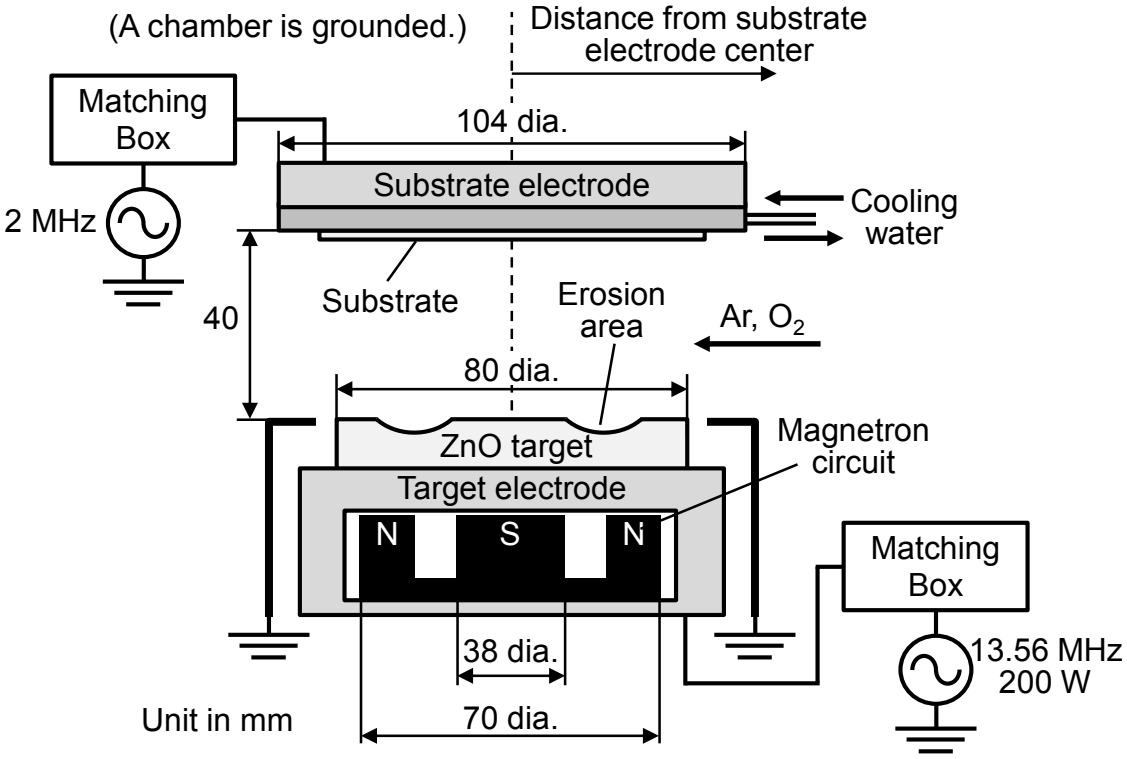

Fig. 4.3 RF-bias sputtering system.

The amount of ion flux and ion energy which enter the substrate were measured by using an energy analyzer with a quadrupole mass spectrometer (PSM003, Hiden Analytical) as shown in Fig 4.4. 2 MHz RF power of 0-25 W was applied to the substrate electrode during the measurement. Except for RF power of 50 W to the target, the discharge conditions in the measurement were set to be same as in the film growths. As is the case with Chapter 3, strong O_2^+ and O^- peaks were observed in mass spectra, and therefore, the ion energy distributions of these ions were focused.

Table 4.2 Deposition conditions in the RF-bias sputtering

Gas pressure	1 Pa
Ar / O_2	1 / 3
RF power supply to the target	13.56 MHz, 200W
RF bias power supply	2 MHz, 0-50 W
Deposition time	3 h

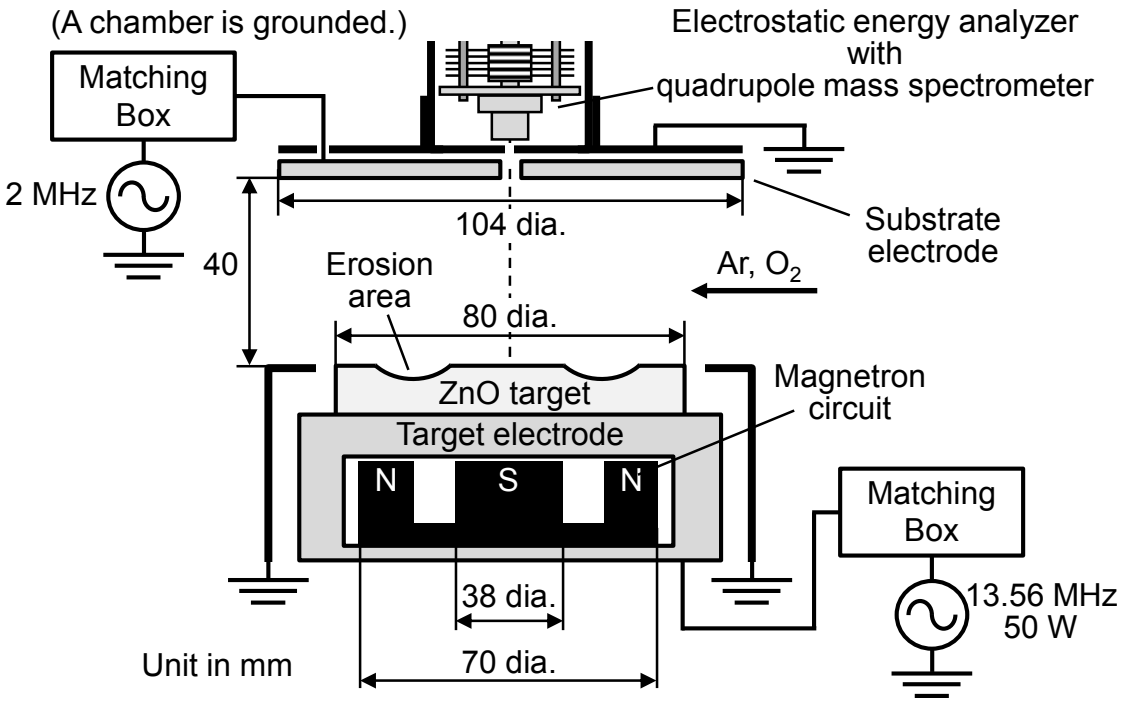

Fig. 4.4 Measurement system for the spatial distributions of the amount of ion flux and the ion energy in the RF-bias sputtering.

4.2.b RESULTS AND DISCUSSIONS

Figure 4.5 shows the energy distributions of O_2^+ positive ions and O^- negative ions which enter the substrate at the substrate electrode center during the RF glow discharge with RF bias. Both the amount of ion flux and ion energy drastically increased as RF bias power increased as expected. These results indicate that the substrate potential becomes negative due to the RF self-bias and the plasma-substrate sheath voltage is increased.

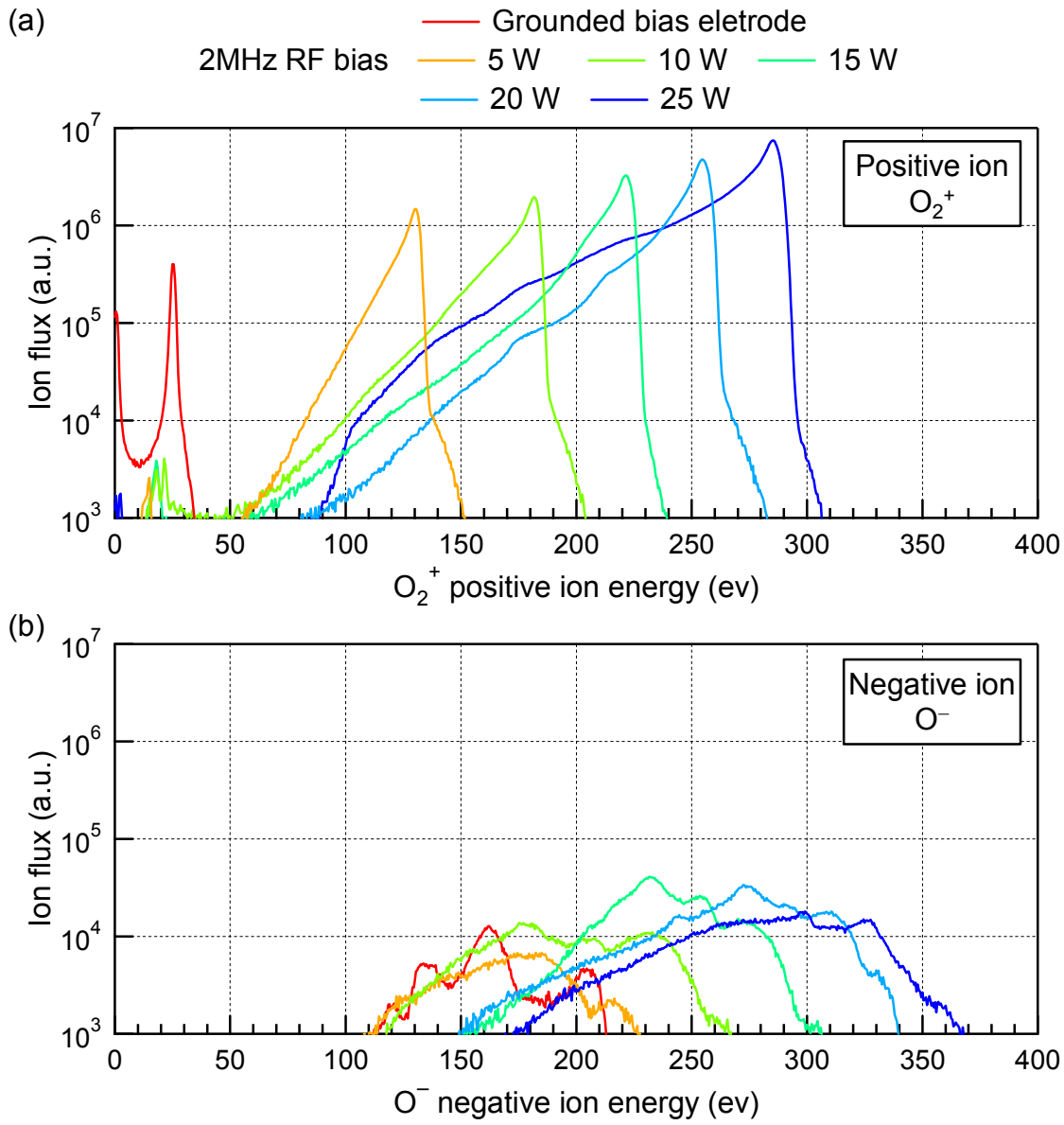

Fig. 4.5 Energy distributions of (a) O_2^+ positive ions and (b) O^- negative ions which enter the substrate during the deposition with 2 MHz RF bias.

In Fig. 4.5(b), the ion flux of O^- negative ions were much lower than that of O_2^+ ions, but the energy of O^- increased with increasing RF bias power. One probable reason of these unexpected results is that the RF bias power is also applied to the plasma-target sheath. In this sputtering system, RF bias is ineffective in decreasing the negative ion bombardment.

Figure 4.6(a) shows the XRD patterns and film thicknesses of the samples at the center of the substrate electrode, and Figure 4.6(b) shows the ratios of the XRD peak integrated intensities of the samples. An intense (0002) peak was observed in the sample grown without bias. In contrast, usual (0001) orientation changed into the $(11\bar{2}0)$ preferred orientation with RF bias power of 10 W, where the peak value of O_2^+ energy was 180 eV. The $(11\bar{2}0)$ preferred orientation then changed into the $(10\bar{1}0)$ preferred orientation with increasing RF bias power of 20 W at O_2^+ energy of 250 eV. Namely, unusual c-axis parallel-oriented films can be grown under the RF bias conditions.

The main reason of these orientation changes is the drastic increase of the ion flux and energy of positive ions induced by the RF bias although the substrate was slightly bombarded with negative ions. In wurtzite films, the (0001) plane has a lower surface energy density than all other planes, which results in the easy growth of the c-axis-perpendicular (0001) orientation [4.7]. The values of the surface energy density of the (0001), $(11\bar{2}0)$, and $(10\bar{1}0)$ planes are 9.9, 12.3 and 20.9 eV/nm^2 [4.7]. The lower the surface energy density is, the higher the surface atomic density becomes, and the higher the damage in the crystal plane by ion bombardment becomes (Fig. 4.7). The gradual changes of main preferred orientation from (0001) to $(10\bar{1}0)$ due to the RF bias are in accordance with the ascending order of the surface energy density. This means that these changes correspond with the order of damage tolerance by ion irradiation. This agrees with the mechanism of the c-axis parallel $(11\bar{2}0)$ or $(10\bar{1}0)$ preferential development as described in Chapters 1. Highly-energetic positive ion bombardment by RF bias sputtering is useful for orientation control of polycrystalline films.

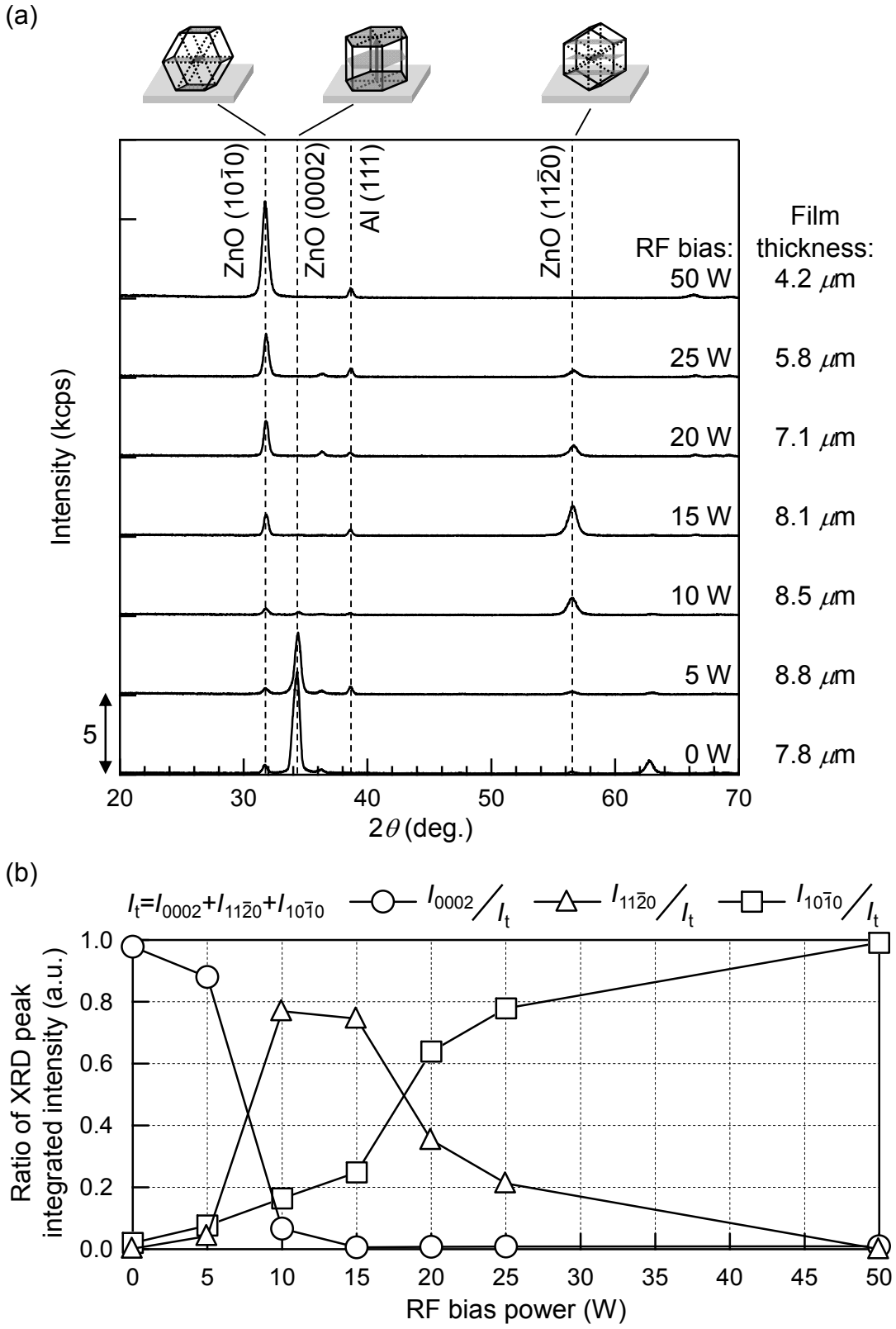

Fig. 4.6 (a) XRD patterns and (b) ratios of the XRD peak integrated intensities of the samples grown without bias, or with 2 MHz RF bias. I_{0002}, $I_{11\bar{2}0}$, and $I_{10\bar{1}0}$ are the integrated intensities of the (0002), (11$\bar{2}$0), and (10$\bar{1}$0) XRD peaks, respectively.

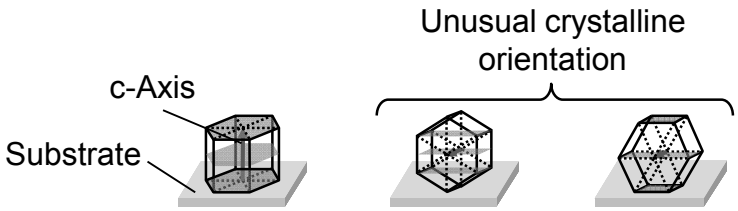

Preferred orientation	(0001) plane	$(11\bar{2}0)$ plane	$(10\bar{1}0)$ plane
RF bias power	Low	⇒	High
Flux and energy of positive ions	Low	⇒	High
Surface energy density (eV/nm^2)	9.9	12.3	20.9 [4.7]
Surface atomic density	High	⇐	Low
Damage by ion bombardment	High	⇐	Low

Fig. 4.7 Summary of the relationship between the preferred orientations and the ion bombardment in RF bias sputtering deposition.

In Fig. 4.6(a), the film thicknesses of the samples grown with the RF bias of 5-15 W were thicker than that without the RF bias, although the substrate was bombarded with the highly-energetic positive ions. These results also indicate that the increase of the plasma-target voltage by the RF bias. With increasing RF bias power of 20 W, the sputtering of the film was caused by the positive ion bombardment, and then the film thickness of the sample was decrease. However, an intense $(10\bar{1}0)$ peak was observed in the sample with 50 W RF bias. 3-dimensional crystalline orientation of the $(10\bar{1}0)$ ZnO film was evaluated by $(10\bar{1}1)$ pole figure. The $(10\bar{1}1)$ plane in ZnO crystal has an angle of 28º with the $(10\bar{1}0)$ plane, so that $(10\bar{1}1)$ pole figure indicates poles at ψ =28º. Fig. 4.8 shows the $(10\bar{1}1)$ pole figures measured at 0 and 45 mm from the substrate electrode center. $\{10\bar{1}1\}$ poles were not concentrated at ψ =28º in the sample at 0 mm. Therefore, the c-axis oriented randomly in in-plane direction. On the other hand, at 45 mm from the substrate electrode center, two concentrated $\{10\bar{1}1\}$ poles were observed near ψ=28º, ϕ=90º and ψ=28º, ϕ=270º. This result indicate that the c-axis aligned in both out-of-plane and in-plane direction. Degree of the $(10\bar{1}0)$ orientation measured by ω-rocking curve FWHM was 4.7º. In the glow discharge, positive

ions generally enter the electrodes at right angle. Therefore, the in-plane alignment of c-axis would not be expected by the positive ion bombardment. On the other hand, the substrate remained to be bombarded with highly-energetic negative ions in the RF bias conditions (Fig. 4.5(b)). A probable reason for the alignment is the bombardment with the negative ions generated near the target, as is the case in Chapter 3.

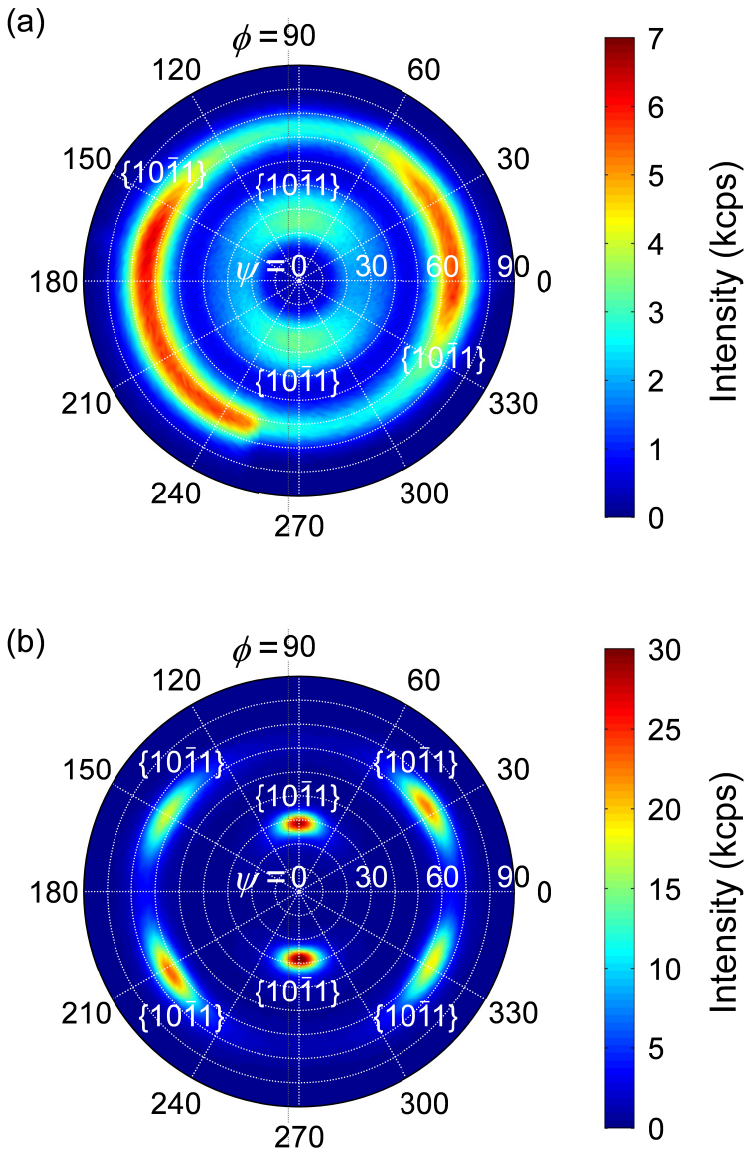

Fig. 4.8 (10$\bar{1}$1) pole figure of the sample with the RF bias of 50 W, measured at (a) 0 and (b) 45 mm from the anode center.

4.3 UNUSUAL CRYSTAL GROWTH OF AlN FILM USING RF-SUBSTRATE-BIAS SPUTTERING

AlN films, which have wurtzite structure, are attractive for high-frequency piezoelectric devices [4.8, 4.9] because the BAW velocity of AlN is about two times higher than that of ZnO. However, low piezoelectric constants of AlN lead to low electromechanical coupling coefficient. Recently, Akiyama et al. found the significant increase of piezoelectricity in the Sc heavily doped AlN film [4.10]. The value of the extensional piezoelectric constant in $Sc_{0.43}Al_{0.57}N$ film was increased five-fold as compared with that in pure AlN film. In this section, unusual crystal growths of c-axis-parallel-oriented AlN and ScAlN will be demonstrated using RF bias sputtering.

4.3.a ION BOMBARDMENT DURING AlN FILM GROWTH

In AlN film growths, argon and nitrogen gas is usually introduced, and Al metal target is used. Figure 4.9 (a) and (b) shows mass spectra of positive ions and negative ions bombarding the substrate in a conventional RF magnetron sputtering system. The total gas pressure was set 1 Pa, and the Ar/N_2 gas ratio was set to 1/3. RF power of 50 W was applied to the Al target. In this condition, a large amount of gas molecules were positively ionized during the discharge. However, highly energetic ions such as N^- were not generated from the Al target surface.

In Chapter 3, the author pointed out c-axis parallel oriented ZnO film was induced by the ion bombardment of highly energetic O^- from a ZnO target to the substrate during the RF magnetron sputtering (Fig 4.9(c)). Therefore, c-axis parallel oriented AlN film cannot be expected in a conventional sputtering system. On the other hand, positive ions had low energy, but they were easily accelerated by RF substrate bias. Figure 4.10 shows energy distributions of Ar^+ positive ions which enter the substrate during the AlN growth with 2 MHz RF bias. As is the case in Section 4.2, both the amount of

ion flux and ion energy drastically increased as RF bias power increased. This highly-energetic positive ion bombardment can be used for the unusual crystal growth.

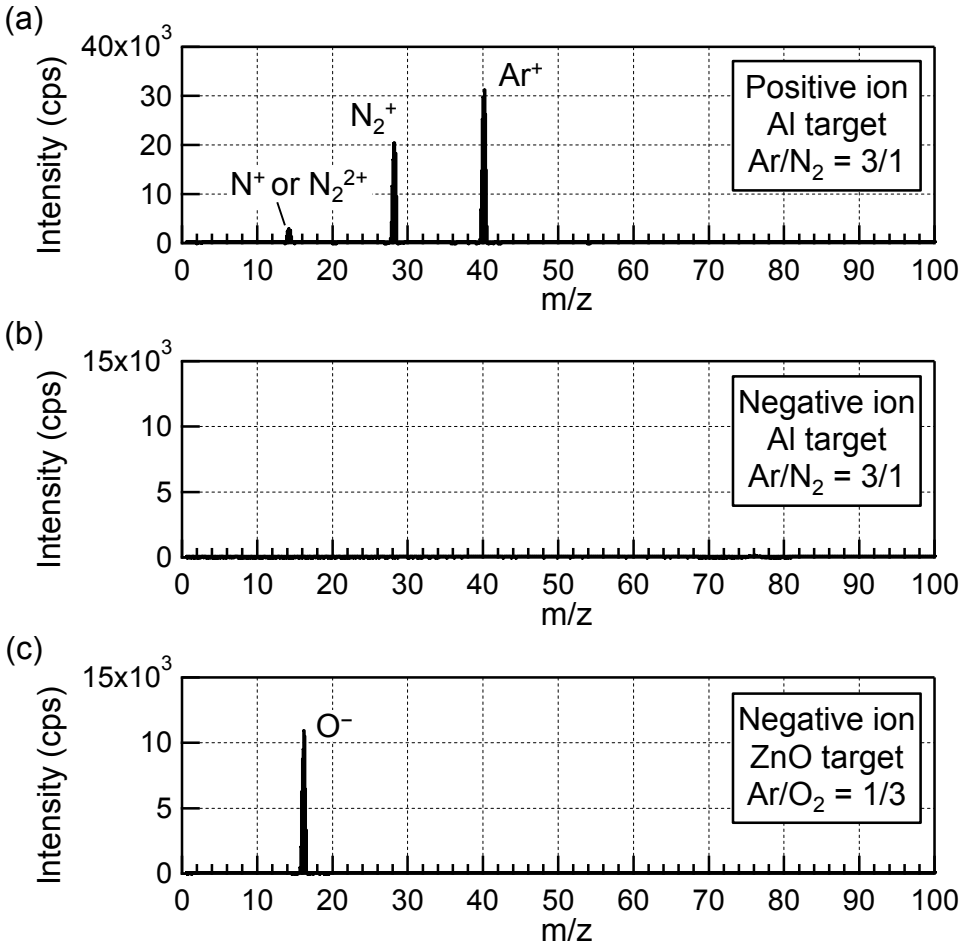

Fig. 4.9 Mass spectra of (a) positive ions and (b) negative ions bombarding the substrate in AlN film growth, and that of (c) negative ions in ZnO film growth using a conventional RF magnetron sputtering.

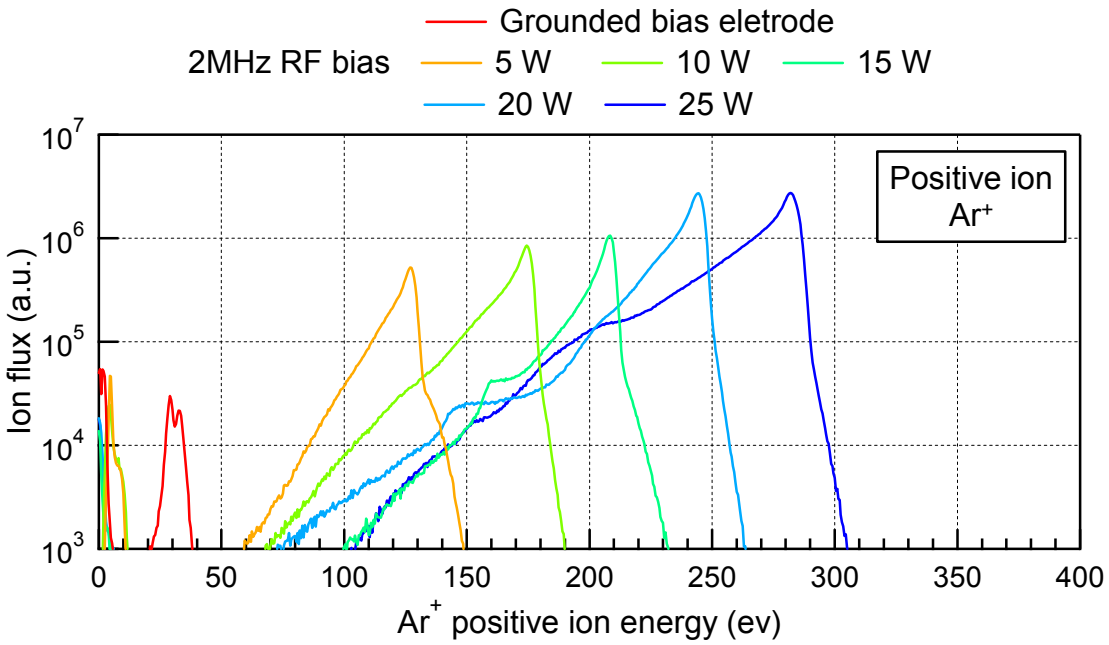

Fig. 4.10 Energy distributions of Ar^+ positive ions which enter the substrate during the AlN growth with 2 MHz RF bias.

4.3.b AlN AND ScAlN FILM GROWTH

The deposition condition of AlN sample growth in RF-bias sputtering is shown in Table 4.3. The sputtering system was same in Section 4.2. A Silica glass with evaporated aluminum electrode layer was used as a substrate. A sample on a silica glass without the RF bias was also prepared for comparison. For ScAlN growth, Sc ingot grains were set on the Al target. Yanagitani et al. reported about 20% Sc concentration in the deposited sample with the totally 1 g Sc grains [4.11]. The deposition condition of ScAlN growth was same in Table 4.3 except for the Sc ingot grains.

Table 4.3 Deposition condition of an AlN sample growth in RF-bias sputtering

Gas pressure	1 Pa
Ar / N_2	3 / 1
RF power supply to the target	13.56 MHz, 100W
RF bias power supply	2 MHz, 10 W
Sputtering target	Al

The crystalline orientations of the samples were measured by 2θ–ω scan XRD. Figure 4.11 shows the XRD patterns of the samples. An (0002) peak was observed in the sample deposited without bias. The (0001) plane has a lower surface energy density than all other planes, as is the case in ZnO crystal, which results in the easy formation of the (0001) preferred orientation. The usual (0001) orientation changed into the $(11\bar{2}0)$ preferred orientation with RF bias as expected. On the other hand, $(11\bar{2}0)$ and $(10\bar{1}0)$ XRD peaks were observed in the ScAlN film with 10 W RF bias. The c-Axis parallel oriented ScAlN film can be also grown under the RF bias condition. FWHM values of the $(11\bar{2}0)$ plane ω-scan rocking curves were 6.6º in AlN film and 5.0º in ScAlN film. However, in $\{11\bar{2}2\}$ pole figure analysis, $\{11\bar{2}2\}$ poles were not observe, and therefore c-axis randomly oriented in the plane of the film. This result also indicates the in-plane alignment required an angled bombardment of negative ions. Further results on the incident angle of ion bombardment should be examined.

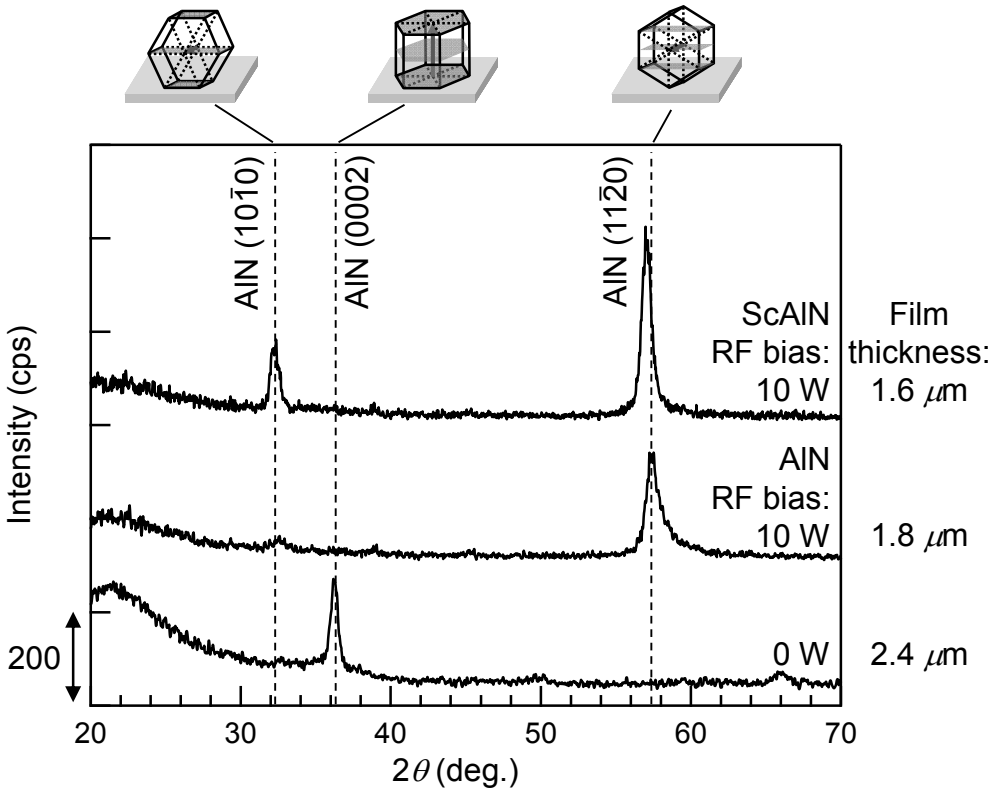

Fig. 4.11 XRD patterns of the AlN and ScAlN samples with 2 MHz RF bias.

REFERENCES

[4.1] J. L. Vossen and J. J. O'Neill Jr.,
RCA Review **29,** 566 (1968).

[4.2] J. L. Vossen,
J. Vac. Sci. Tech. **8,** S12 (1971).

[4.3] J. W. Patten and E. D. McClanahan,
J. Appl. Phys. **43,** 4811 (1972).

[4.4] H. F. Winters and E. Kay,
J. Appl. Phys. **38,** 3928 (1968).

[4.5] J. W. Coburn and E. Kay,
J. Appl. Phys. **43**, 4965 (1972).

[4.6] G. K. Wehner and G. S. Anderson,
Handbook of Thin Film Technology edited by L. I. Maissel and R. Glang (McGraw-Hill, New York, 1970), p. 3-10.

[4.7] N. Fujimura, T. Nishihara, S. Goto, J. Xu, and T. Ito,
J. Cryst. Growth **130**, 269 (1993).

[4.8] S. Fujii, T. Odawara, T. Omori, K. Hashimoto, H. Torii, H. Umezawa, and S. Shikata,
in *2011 IEEE Int. Ultrasonics Symp. Proc.*, Orlando, Florida, 18-21 October 2011, pp. 555-558.

[4.9] K. Hashimoto, S. Sato, A. Teshigahara, T. Nakahara, and K. Kano,
IEEE Trans. Ultrason. Ferroelectr. Freq. Control **60**, 637 (2013).

[4.10] M. Akiyama, T. Kamohara, K. Kano, A. Teshigahara, Y. Takeuchi, and N. Kawahara,
Adv. Mater. **21**, 593 (2009).

[4.11] N. Suganuma, M. Suzuki, and T. Yanagitani,
in *Proc. Piezoelectric Materials and Devices Symp.*, Sendai, Japan, 30-31 January 2012, pp. 19-22 [in Japanese].

5 PIEZOELECTRIC EFFECT AND ELECTROMECHANICAL CONVERSION

5.1 PIEZOELECTRIC EFFECT

Electric charges appear on a piezoelectric crystal surface with internal electrical fields when stress is applied to the crystal. This phenomenon is called piezoelectricity. Periodic expansions and contractions are generated in the crystal by an electromagnetic wave. Acoustic waves can be excited as a result of this phenomenon. The piezoelectric stress equation can be written as

$$T_{ij} = c^{E}_{ijkl} S_{kl} - e_{kij} E_k \,, \tag{5.1.a}$$

$$D_i = e_{ikl} S_{kl} + \varepsilon^{S}_{ik} E_k \,. \tag{5.1.b}$$

where, T_{ij}, S_{kl}, D_i and E_k are stress, strain, electric flux density and electric field components, respectively. These equations include three constants: elastic constants c^{E}_{ijkl}, piezoelectric constants e_{ijk} and dielectric constant ε^{S}_{ik}. Superscripts E and S mean elastic and dielectric constants measured under constant electric field and strain, respectively. A part of Eq. (5.1.a) represents *Hooke*'s law which describes the relationship between T_{ij} and S_{kl}. In addition, if E_k is applied to the crystal, T_{ij} are induced.

5.2 MATERIAL CONSTANT TENSOR

ZnO has a hexagonal structure as shown in Fig. 5.1. Piezoelectric properties of ZnO crystals depend on the crystal direction due to the crystal anisotropy [5.1-5.2]. Subscript matrix notations of the constants in Eq. (5.1) are abbreviated as $T_{ij} \equiv T_p$, $S_{kl} \equiv S_q$, $c^{E}_{ijkl} \equiv c^{E}_{pq}$, and $e_{ikl} \equiv e_{ip}$ introduced in IEEE Standard on Piezoelectricity [5.3]. The elastic constant tensor of ZnO is simplified by hexagonal symmetry [5.4]:

$$c_{pq}{}^{E} = \begin{pmatrix} 2.096 & 1.205 & 1.046 & 0 & 0 & 0 \\ 1.205 & 2.096 & 1.046 & 0 & 0 & 0 \\ 1.046 & 1.046 & 2.106 & 0 & 0 & 0 \\ 0 & 0 & 0 & 0.423 & 0 & 0 \\ 0 & 0 & 0 & 0 & 0.423 & 0 \\ 0 & 0 & 0 & 0 & 0 & 0.446 \end{pmatrix} \times 10^{11} \text{ [N/m}^2\text{]}. \quad (5.2)$$

The piezoelectric constant tensor e_{ip} of ZnO is as follows:

$$e_{ip} = \begin{pmatrix} 0 & 0 & 0 & 0 & -0.48 & 0 \\ 0 & 0 & 0 & -0.48 & 0 & 0 \\ -0.573 & -0.573 & 1.321 & 0 & 0 & 0 \end{pmatrix} \text{ [C/m}^2\text{]}. \quad (5.3)$$

The relative dielectric constant is

$$\varepsilon_{ik}^{S} / \varepsilon_0 = \begin{pmatrix} 8.55 & 0 & 0 \\ 0 & 8.55 & 0 \\ 0 & 0 & 10.2 \end{pmatrix}, \quad (5.4)$$

where, $\varepsilon_0 = 8.854 \times 10^{-12}$ [F/m]. The density ρ of ZnO is 5.665×10^3 kg/m^3.

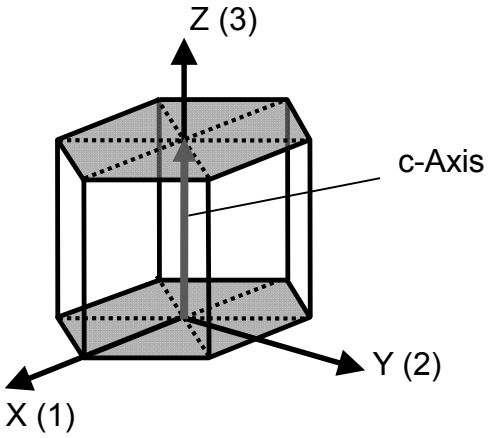

Fig. 5.1. Hexagonal structure.

Wave propagation properties of BAWs and SAWs depend on crystalline anisotropy. The coordinate transformations are required in each tensor so that the direction of the crystal axis (X, Y, Z) corresponds to that of the wave propagation (x_1, x_2, x_3). Fig 5.2 shows Euler angles ϕ, θ, and ψ for the coordinate transformations. The transformation matrix [a] through ϕ, θ, and ψ is described by:

$$[a]=\begin{bmatrix}\cos\phi & \sin\phi & 0\\ -\sin\phi & \cos\phi & 0\\ 0 & 0 & 1\end{bmatrix}\begin{bmatrix}1 & 0 & 0\\ 0 & \cos\theta & \sin\theta\\ 0 & -\sin\theta & \cos\theta\end{bmatrix}\begin{bmatrix}\cos\psi & \sin\psi & 0\\ -\sin\psi & \cos\psi & 0\\ 0 & 0 & 1\end{bmatrix}. \qquad (5.5)$$

The dielectric constant ε' transforms as

$$[\varepsilon']=[a]\ [\varepsilon]\ [a]^T. \qquad (5.6)$$

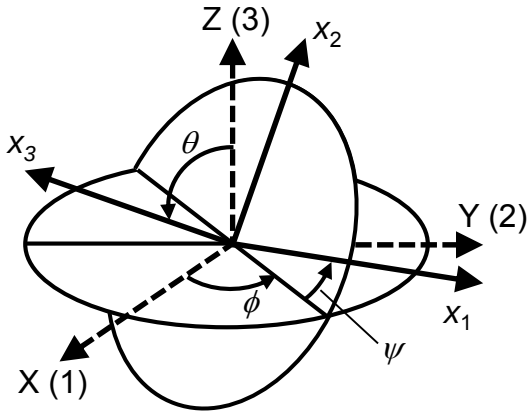

Fig. 5.2. Euler angles ϕ, θ, and ψ for the coordinate transformations.

To transform the elastic and piezoelectric constant tensors, Bond's method [5.5] is applied to the tensors with abbreviated subscript notations. The 6×6 transformation matrix of coefficients [M] in Bond's method is given as

$$[M]=\begin{bmatrix} a_{11}^2 & a_{12}^2 & a_{13}^2 & 2a_{12}a_{13} & 2a_{13}a_{11} & 2a_{11}a_{12} \\ a_{21}^2 & a_{22}^2 & a_{23}^2 & 2a_{22}a_{23} & 2a_{23}a_{21} & 2a_{21}a_{22} \\ a_{31}^2 & a_{32}^2 & a_{33}^2 & 2a_{32}a_{33} & 2a_{33}a_{31} & 2a_{31}a_{32} \\ a_{21}a_{31} & a_{22}a_{32} & a_{23}a_{33} & a_{22}a_{33}+a_{23}a_{32} & a_{23}a_{31}+a_{21}a_{33} & a_{21}a_{32}+a_{22}a_{31} \\ a_{31}a_{11} & a_{32}a_{12} & a_{33}a_{13} & a_{12}a_{33}+a_{13}a_{32} & a_{13}a_{31}+a_{11}a_{33} & a_{11}a_{32}+a_{12}a_{31} \\ a_{11}a_{21} & a_{12}a_{22} & a_{13}a_{23} & a_{12}a_{23}+a_{13}a_{22} & a_{13}a_{21}+a_{11}a_{23} & a_{11}a_{22}+a_{12}a_{21} \end{bmatrix}. \tag{5.7}$$

Finally, transformed elastic and piezoelectric constant tensors *c*' and *e*' are obtained using Eqs. (5.5) and (5.7):

$$[c']=[M]\,[c]\,[M]^T, \tag{5.8}$$

and

$$[e']=[a]\,[e]\,[M]^T. \tag{5.9}$$

5.3 BAW PROPAGATION

In Chapters 3 and 4, c-axis parallel oriented ZnO films could be grown. For their applications to BAW devices, BAW propagation in the film will be analyzed in this section. Fig. 5.3 shows an analytical model of it. The x_3 direction is the wave propagation direction, and the x_1 direction corresponds to the c-axis direction. The Euler angles (ϕ, θ, ψ) are (0º, 90º, 90º) in this model. Transformed elastic constant, piezoelectric constant and dielectric constant tensors $c'_{pq}{}^{E}$, e'_{ip} and $\varepsilon'_{ik}{}^{S}$ are calculated as follows:

$$c'^{E}_{pq} = \begin{pmatrix} 2.096 & 1.046 & 1.046 & 0 & 0 & 0 \\ 1.046 & 2.096 & 1.205 & 0 & 0 & 0 \\ 1.046 & 1.205 & 2.106 & 0 & 0 & 0 \\ 0 & 0 & 0 & 0.446 & 0 & 0 \\ 0 & 0 & 0 & 0 & 0.423 & 0 \\ 0 & 0 & 0 & 0 & 0 & 0.423 \end{pmatrix} \times 10^{11}\ [\mathrm{N/m^2}], \quad (5.10)$$

$$e'_{ip} = \begin{pmatrix} 1.321 & -0.573 & -0.573 & 0 & 0 & 0 \\ 0 & 0 & 0 & 0 & 0 & -0.48 \\ 0 & 0 & 0 & 0 & -0.48 & 0 \end{pmatrix}\ [\mathrm{C/m^2}], \quad (5.11)$$

$$\varepsilon'^{S}_{ik} / \varepsilon_0 = \begin{pmatrix} 10.2 & 0 & 0 \\ 0 & 8.55 & 0 \\ 0 & 0 & 8.55 \end{pmatrix}. \quad (5.12)$$

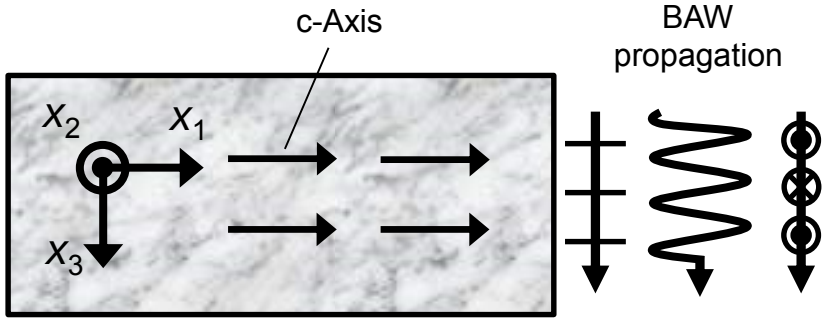

Fig. 5.3. Analytical model of BAW propagation in a c-axis-parallel-oriented film.

In BAW propagation toward x_3 direction, general plane-wave solutions of mechanical displacement components u_1, u_2, u_3 and electric potential φ are well known as:

$$\begin{pmatrix} u_1 \\ u_2 \\ u_3 \\ \varphi \end{pmatrix} = \begin{pmatrix} A_1 \\ A_2 \\ A_3 \\ A_4 \end{pmatrix} \exp\left\{ j\omega \left(t - \frac{x_3}{v} \right) \right\}, \quad (5.13)$$

where ω is the angular frequency and v is the phase velocity. The Strain field components S_{kl} are defined by u_1, u_2 and u_3 as

$$S_{kl} = \frac{1}{2}\left(\frac{\partial u_k}{\partial x_l} + \frac{\partial u_l}{\partial x_k} \right) \qquad (k = l), \tag{5.14.a}$$

$$S_{kl} = \frac{\partial u_k}{\partial x_l} + \frac{\partial u_l}{\partial x_k} \qquad (k \neq l). \tag{5.14.b}$$

and the electric field E_k are given by φ:

$$E_k = -\frac{\partial \varphi}{\partial x_k}. \tag{5.15}$$

Thus, the wave motion equation for the x_3 direction is given by

$$\rho \frac{\partial^2 u_1}{\partial t^2} = \frac{\partial T_{11}}{\partial x_1} + \frac{\partial T_{21}}{\partial x_2} + \frac{\partial T_{31}}{\partial x_3} = \frac{\partial T_{31}}{\partial x_3}, \tag{5.16.a}$$

$$\rho \frac{\partial^2 u_2}{\partial t^2} = \frac{\partial T_{12}}{\partial x_1} + \frac{\partial T_{22}}{\partial x_2} + \frac{\partial T_{32}}{\partial x_3} = \frac{\partial T_{32}}{\partial x_3}, \tag{5.16.b}$$

$$\rho \frac{\partial^2 u_3}{\partial t^2} = \frac{\partial T_{13}}{\partial x_1} + \frac{\partial T_{23}}{\partial x_2} + \frac{\partial T_{33}}{\partial x_3} = \frac{\partial T_{33}}{\partial x_3}, \tag{5.16.c}$$

where

$$T_{31} = T_5 = c'^{E}_{55} \frac{\partial u_1}{\partial x_3} + e'_{35} \frac{\partial \varphi}{\partial x_3}, \tag{5.17.a}$$

$$T_{32} = T_4 = c'^{E}_{44} \frac{\partial u_2}{\partial x_3}, \tag{5.17.b}$$

$$T_{33} = T_3 = c'^{E}_{33} \frac{\partial u_3}{\partial x_3}. \tag{5.17.c}$$

As div $\boldsymbol{D}$ = 0, the electrostatic equation is as follows:

$$\frac{\partial D_3}{\partial x_3} = e'_{35}\frac{\partial^2 u_1}{\partial x_3^2} - \varepsilon'^{S}_{33}\frac{\partial^2 \varphi}{\partial x_3^2} = 0. \tag{5.18}$$

Substituting Eq. (5.13) into Eqs. (5.16) and (5.18) gives the following relation:

$$\begin{pmatrix} c'^{E}_{55} - \rho v^2 & 0 & 0 & -e'_{35} \\ 0 & c'^{E}_{44} - \rho v^2 & 0 & 0 \\ 0 & 0 & c'^{E}_{33} - \rho v^2 & 0 \\ -e'_{35} & 0 & 0 & \varepsilon'^{S}_{33} \end{pmatrix} \begin{pmatrix} A_1 \\ A_2 \\ A_3 \\ A_4 \end{pmatrix} = 0. \tag{5.19}$$

If A_1, A_2, A_3 and A_4 are all nonzero, three types of the phase velocity are obtained:

$$v_{S1} = \sqrt{\frac{c'^{E}_{55} + \frac{e'^{\,2}_{35}}{\varepsilon'^{S}_{33}}}{\rho}} = 2830 \text{ [m/s]}, \tag{5.20.a}$$

$$v_{S2} = \sqrt{\frac{c'^{E}_{44}}{\rho}} = 2800 \text{ [m/s]}, \tag{5.20.b}$$

$$v_{L} = \sqrt{\frac{c'^{E}_{33}}{\rho}} = 6080 \text{ [m/s]}. \tag{5.20.c}$$

v_{S1} and v_{S2} are the velocities of pure shear wave with a u_1 and u_2 displacement, respectively, and v_L is that of longitudinal wave. Only v_{S1} includes the piezoelectric constant e'_{35}. This result means that a shear stress T_5 is generated through coupling of the piezoelectric constant e'_{35}, when an electric field E_3 is applied to a ZnO film whose c-axis is aligned along the x_1 direction. Therefore, a shear-mode HBAR and FBAR can be fabricated by sandwiching a c-axis-parallel ZnO film between a top and bottom electrodes.

5.4 ELECTROMECHANICAL COUPLING COEFFICIENT

A Degree of the transformation of electrical energy into mechanical energy and vice versa is defined by electromechanical coupling coefficient k. The value of k depends on vibration mode and temperature, and affects the insertion loss and bandwidth of piezoelectric transducers as well as various piezoelectric devices. An input electrical energy U_i and an output mechanical energy U_o can be given by

$$U_i = \frac{1}{2} ED = \frac{1}{2} \varepsilon^S E^2, \tag{5.21.a}$$

$$U_o = \frac{1}{2} TS = \frac{1}{2} \frac{e^2 E^2}{c^E}. \tag{5.21.b}$$

Here, electromechanical coupling coefficient k is defined as

$$\frac{k^2}{1-k^2} = \frac{U_o}{U_i} = \frac{e^2}{\varepsilon^S c^E} \tag{5.22}$$

using piezoelectric constant e, dielectric constant ε^S and elastic constant c^E. Thus, k can be written as

$$k^2 = \frac{e^2 / \varepsilon^S}{e^2 / \varepsilon^S + c^E}. \tag{5.23}$$

Using piezoelectrically stiffened elastic constant

$$c^D = c^E + \frac{e^2}{\varepsilon^S}, \tag{5.24}$$

which measured under constant electric flux density, k is written by c^D as

$$k = \sqrt{1 - \frac{c^E}{c^D}} \,. \tag{5.25}$$

On the other hand, in SAW and Lamb wave analyses, the effective electromechanical coupling coefficient K^2 is derived from

$$K^2 = 2 \times \left(1 - \frac{v_\mathrm{m}}{v_\mathrm{f}} \right), \tag{5.26}$$

where v_f and v_m are the phase velocities for the free and metallized surface of the wave propagation path, respectively.

REFERENCES

[5.1] N. F. Foster, G. A. Coquin, G. A. Rozgonyi, and F. A. Vannatta, IEEE Trans. Ultrason. Ferroelectr. Freq. Control **15**, 28 (1968).

[5.2] B. A. Auld, *Acoustic fields and waves in solid*, (Wiley, New York, 1973), vol. 1, p. 73.

[5.3] *IEEE Stabdard on Piezoelectricity (ANSI/IEEE Std. 176-1987)*, IEEE Trans. Ultrason. Ferroelectr. Freq. Control **43**, 719 (1996).

[5.4] R. T. Smith and V. E. Stubblefield, J. Acoust. Soc. Am., **46**, 105 (1969).

[5.5] W. Bond, Bell System Technical Journal, **22**, 1 (1943).

6 ESTIMATION OF ELECTROMECHANICAL COUPLING COEFFICIENT AND THICKNESS OF UNORIENTED LAYER

It is important to know the electromechanical coupling coefficient k in order to apply a piezoelectric film to acoustic-wave devices. In this section, HBAR structures using c-axis-parallel-oriented film were fabricated, and the electromechanical resonance characteristics of these HBARs were experimentally observed. These results were compared with the theoretical estimations by a mechanical transmission line model to determine the shear-mode k_{15} [6.1, 6.2].

In addition, by applying this method, the thickness of the unoriented layer was predicted. Wide band-gap semiconductor films such as GaN, AlN, ZnO and SiC have been well studied to meet the demands of short-wavelength optical devices and high-power electronic devices [6.3-6.7]. In particular, highly oriented polycrystalline ZnO have been of great interest for use in transparent thin film transistors [6.8, 6.9]. ZnO films can be deposited on glass or plastic substrate without use of an epitaxial technique and therefore they are promising for invisible and flexible display devices [6.8-6.13]. In the case of non-epitaxial growth such as a growth of the highly oriented polycrystalline film, crystalline orientation in initial stage of the growth differs from that in full-grown stage [6.14]. Distribution of the crystalline orientation in the depth direction is, however, difficult to investigate by using a usual non-destructive XRD method. Therefore, the crystalline orientation in the depth direction is generally determined by a cross sectional transmission electron microscopy (TEM) analysis and electron diffraction in the cross section of cut samples. In this chapter, a non-destructive method for predicting the thickness of the unoriented layer, making use of piezoelectricity distribution of films is proposed.

6.1 ONE-DIMENSIONAL MECHANICAL TRANSMISSION LINE MODEL

6.1.a MASON'S EQUIVALENT CIRCUIT MODEL

An HBAR structure is fabricated to estimate electromechanical coupling coefficient k_{15} in c-axis-parallel oriented film [6.1, 6.2] as shown in Fig. 6.1. The experimentally-observed HBAR conversion loss compares with numerical simulation model. One-dimensional Mason's equivalent circuit model was employed as a simulation model [6.15]. To consider the effect of electrode on HBAR, Equivalent circuit is represented including thin electrode layers.

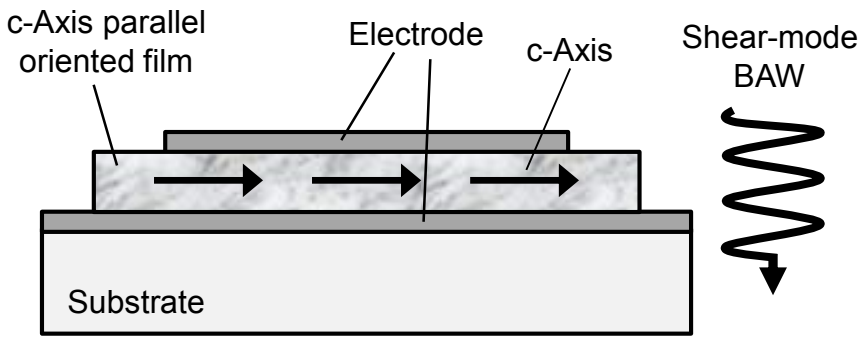

Fig. 6.1 HBAR structure consisting of c-axis-parallel-oriented film.

In the case of non-piezoelectric elastic solid, a thickness shear mode vibrator can be described as T-type equivalent circuit (Fig. 6.2), where F_1 and F_2 are mechanical forces, and v_1 and v_2 are particle velocity acting on each surface of the solid. Here, Z is acoustic impedance, γ is the propagation constant, and d is the thickness of the solid. γ and Z are given as:

$$\gamma = j\frac{\omega}{v_{S1}}, \tag{6.1}$$

$$Z = S\rho v_{S1}, \tag{6.2}$$

where ρ is density of the elastic solid and S is electrode area of the vibrator. On the other hand, the vibrator with a piezoelectric elastic solid can be described as the Mason's three port equivalent circuit. As shown in Fig. 6.3, this circuit includes additional electric terminal concerning electric voltage V and current I [6.15]. Static capacitance C and ratio of transformer ϕ_0 in the circuit are written as:

$$C = \varepsilon'^{S}_{33} \frac{S}{d}, \tag{6.3}$$

$$\phi_0 = \frac{e'_{35} S}{d}. \tag{6.4}$$

Shear mode electromechanical coupling coefficient k_{15} affects the equivalent circuit through the relationship as follows

$$k_{15}^2 = \frac{e'^{\,2}_{35} \Big/ \varepsilon'^{S}_{33}}{e'^{\,2}_{35} \Big/ \varepsilon'^{S}_{33} + c'^{E}_{55}}. \tag{6.5}$$

Thus, ϕ_0 is given by k_{15}

$$\phi_0 = \left[\frac{CZv_{S1}}{d} \left(\frac{k_{15}^2}{1-k_{15}^2} \right) \right]^{\frac{1}{2}}. \tag{6.6}$$

As shown in Fig. 6.4, the equivalent circuit for HBAR is described by cascade arranging non-piezoelectric and piezoelectric part using the circuits in Figs. 6.2 and 6.3. Subscript p, et, eb and s in the figure represent piezoelectric layer, top electrode layer, bottom electrode layer and substrate, respectively. Because of the top electrode surface is free of mechanical stress,

the acoustic input port is shorted. In this case, the substrate thickness is enough to ignore reflection waves from the bottom surface of the substrate. Therefore, it is assumed as infinite.

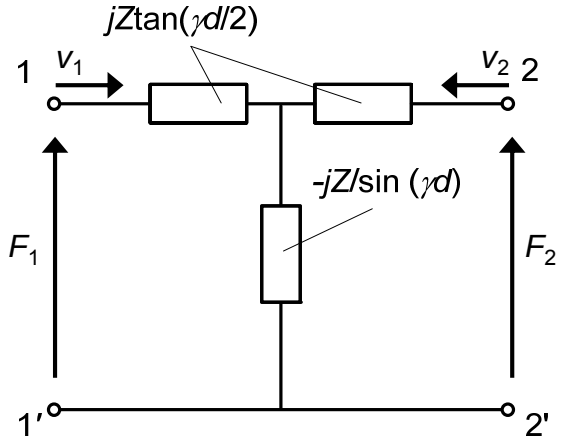

Fig. 6.2 Equivalent circuit of non-piezoelectric elastic solid.

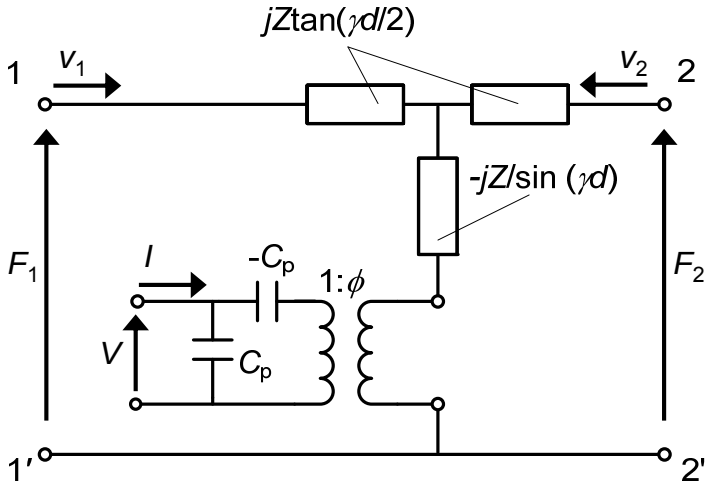

Fig. 6.3 Equivalent circuit of piezoelectric elastic solid.

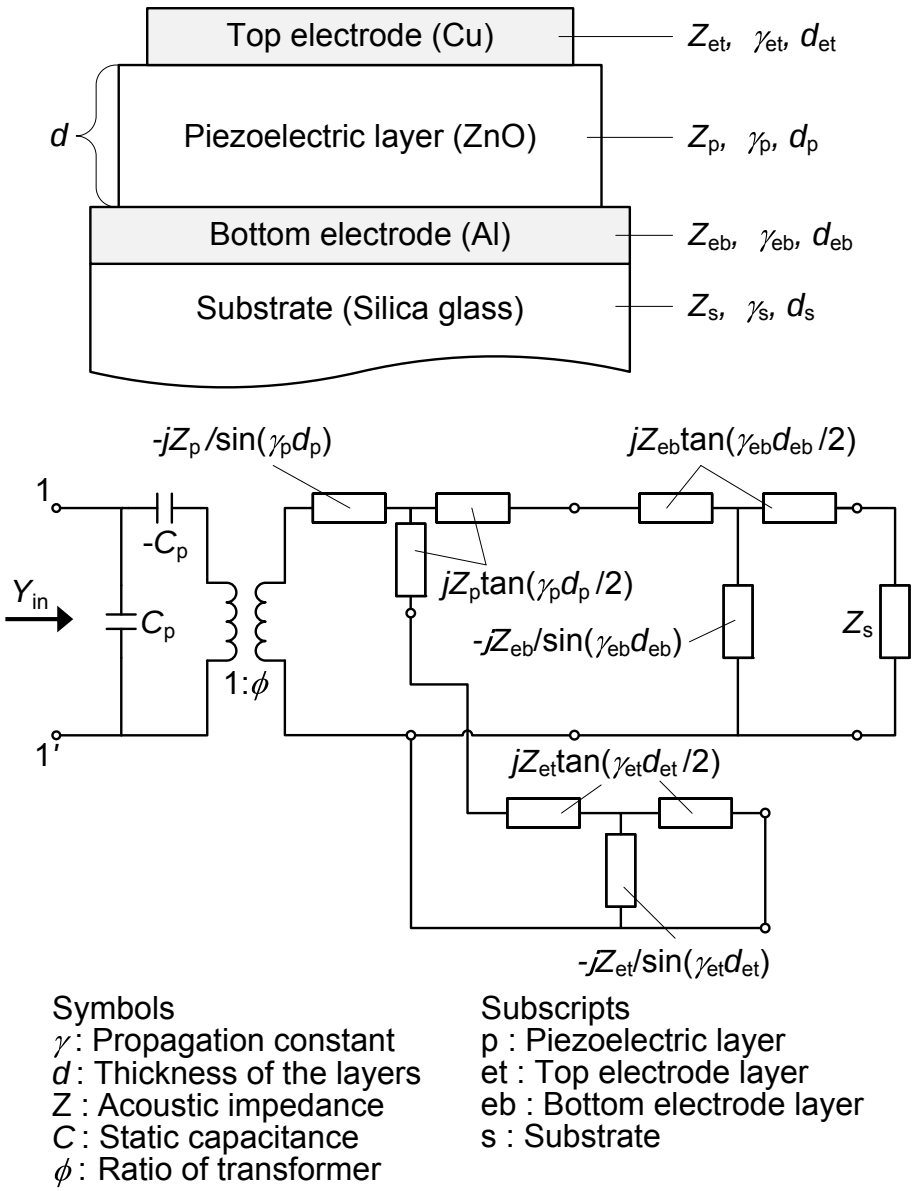

Fig. 6.4 One-dimensional mechanical transmission line model of the HBAR.

Input admittance Y_{in} of the HBAR can be calculated by the equivalent circuit in Fig. 6.4. Using the calculated Y_{in}, conversion loss CL is given by the following equation:

$$CL = 10\log_{10}\frac{4G_0G_f}{\left(G_0+G_f\right)^2+B_f{}^2}+Loss, \tag{6.7}$$

where G_o is the conductance of the electrical source (G_o=0.02 S), G_f and B_f are

input conductance and susceptance of Y_{in}, respectively. The value of electromechanical coupling coefficient k_{15} was optimized so that the calculated minimum conversion loss mostly agrees with the experimental minimum conversion loss.

6.1.b EQUIVALENT CIRCUIT MODEL INCLUDING PIEZOELECTRICALLY INACTIVE LAYER

Thicknesses of a randomly oriented layer or an amorphous layer in the initial stage of the film growth can be predicted non-destructively from the characteristics of electromechanical resonance induced by applying RF electric field. Stress is generated when electric field is applied to a piezoelectric layer. In contrast, stress is not generated when electric field is applied to a randomly oriented layer or amorphous layer, because these layers are piezoelectrically inactive [6.14]. Figures 6.5(a) and (b) show schematic diagrams of piezoelectric polarizations of electromechanical resonators consisting of a single piezoelectric layer and a multilayer including the piezoelectrically inactive layer, respectively. In the case of the single layer resonator, a fundamental mode is excited but a second-overtone mode is not excited, because the stresses or piezoelectric polarizations induced at the upper and lower parts of the piezoelectric layer cancel each other, and acoustic waves cannot be excited in a second-overtone mode. In contrast, in the case of the multilayer resonator including the piezoelectrically inactive layer, both fundamental and second-overtone modes are exited, because the stresses or piezoelectric polarizations induced at the upper and lower parts of the multilayer are not equal and not completely canceled, as shown in Fig. 6.5(b) [6.16]. Therefore, the degree of second-overtone mode excitation is proportional to the degree of the piezoelectricity and the thickness of the inactive layer. In comparison of the experimental intensity ratio of fundamental and second-overtone modes with the theoretical one obtained from a mechanical transmission line model, the thickness of the

piezoelectrically inactive layer can be estimated and the thickness of unoriented layer can be predicted.

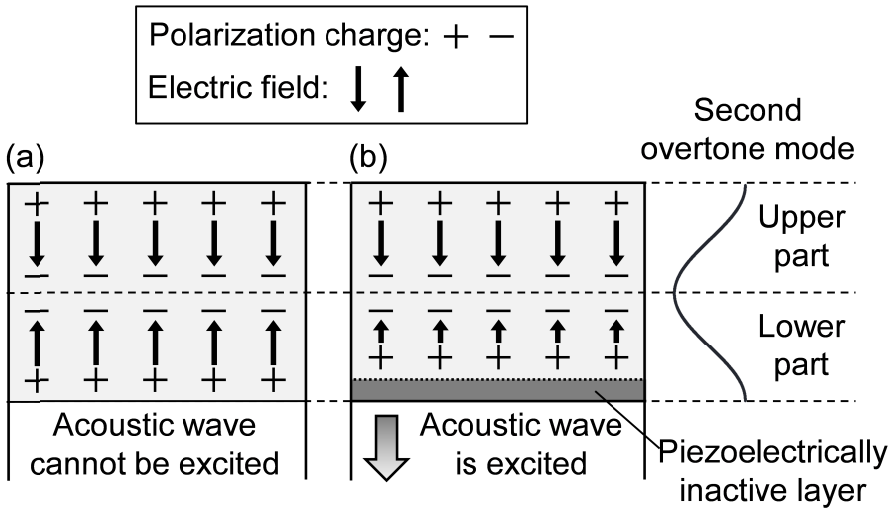

Fig. 6.5 Schematic diagrams of piezoelectric polarizations induced at upper and lower parts of (a) a single uniform piezoelectric layer and (b) a multilayer including the piezoelectrically inactive multilayer, respectively.

Figure 6.6 shows a mechanical transmission line model for a resonator including a piezoelectrically inactive layer in the initial stage of the film growth. Because the crystalline orientation of the piezoelectric film gradually improved as the growth proceeded, the initial growth layer strictly has some piezoelectric response. The piezoelectric effect of initial growth layer is, however, significantly less than that of the highly oriented layer that developed with further film growth. Therefore, this model includes a simple piezoelectrically inactive layer whose mechanical properties are assumed to be ideal ZnO film and the piezoelectric constant is zero. Input admittance Y_{in} was calculated by using the equivalent circuit and then conversion loss *CL* was calculated from Eq. (6.7). The electromechanical coupling coefficient *k* value and the velocity values of the ZnO film were selected so that the minimum conversion loss mostly agreed with the experimental result. Then,

the thickness of the piezoelectrically inactive ZnO layer d_n value was estimated.

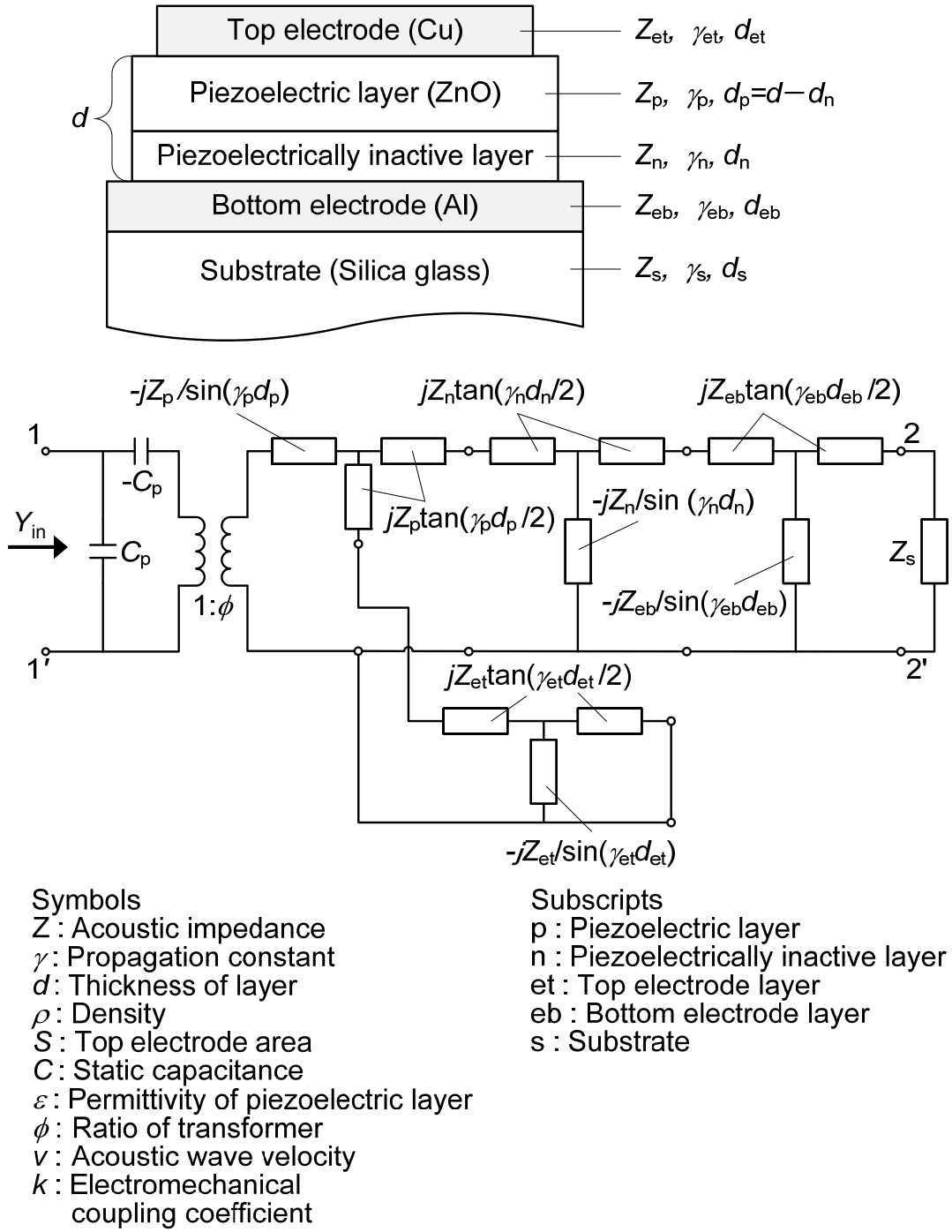

Symbols
Z : Acoustic impedance
γ : Propagation constant
d : Thickness of layer
ρ : Density
S : Top electrode area
C : Static capacitance
ε : Permittivity of piezoelectric layer
ϕ : Ratio of transformer
v : Acoustic wave velocity
k : Electromechanical coupling coefficient

Subscripts
p : Piezoelectric layer
n : Piezoelectrically inactive layer
et : Top electrode layer
eb : Bottom electrode layer
s : Substrate

Fig. 6.6 One-dimensional mechanical transmission line model included a piezoelectrically inactive layer. The substrate thickness is assumed to be infinite to exclude the effect of acoustic waves reflected from the bottom surface of the substrate.

6.2 ESTIMATION OF ELECTROMECHANICAL COUPLING COEFFICIENT

To measure the piezoelectric properties of the HBAR, acoustic waves were excited by applying a high frequency sinusoidal electric field between the top and bottom electrodes [6.17], as shown in Fig. 6.7. Shear waves propagate into the substrate and reflected at the top electrode surface and the bottom surface of the substrate. This wave was observed using inverse Fourier transform of reflection coefficients (S_{11}) of the HBAR (Fig. 6.8), which were measured using a network analyzer (Agilent, E5071B) with a microwave probing system (GGB Industries, Picoprobe model 40A). Top electrode areas were adjusted to have the capacitive impedance of the layers close to 50 Ω at fundamental thickness shear mode resonant frequency. Conversion losses of the HBARs were calculated from a Fourier transform of the first echo in the shear wave. In the conversion losses, the effect of the propagation loss in the silica glass substrate was subtracted using $\alpha/f^2 = 1.99\times10^{-15}$ dB·s^2/m for a shear wave [6.18, 6.19].

The experimental conversion losses were compared with the theoretical conversion losses of one-dimensional mechanical transmission line model in Fig. 6.4. The physical constant tensors of the ZnO layer were assumed to be identical to the single crystal values [6.20] and properly rotated in accordance with the c-axis tilt angle of 90º.

Table 6.1 shows the sample structures of the HBARs. The c-axis-parallel-oriented ZnO film in sample A was grown by a conventional RF magnetron sputtering system in Chapter 3 and had $(11\bar{2}0)$ preferred orientation. The FWHM value of the ZnO$(11\bar{2}0)$ plane ω-scan rocking curve was 5.1º. On the other hand, the c-axis-parallel-oriented ZnO film in sample B was grown by RF substrate bias sputtering in Chapter 4 and had $(10\bar{1}0)$ preferred orientation. The FWHM value of the ZnO$(10\bar{1}0)$ plane ω-scan rocking curve was 5.7º.

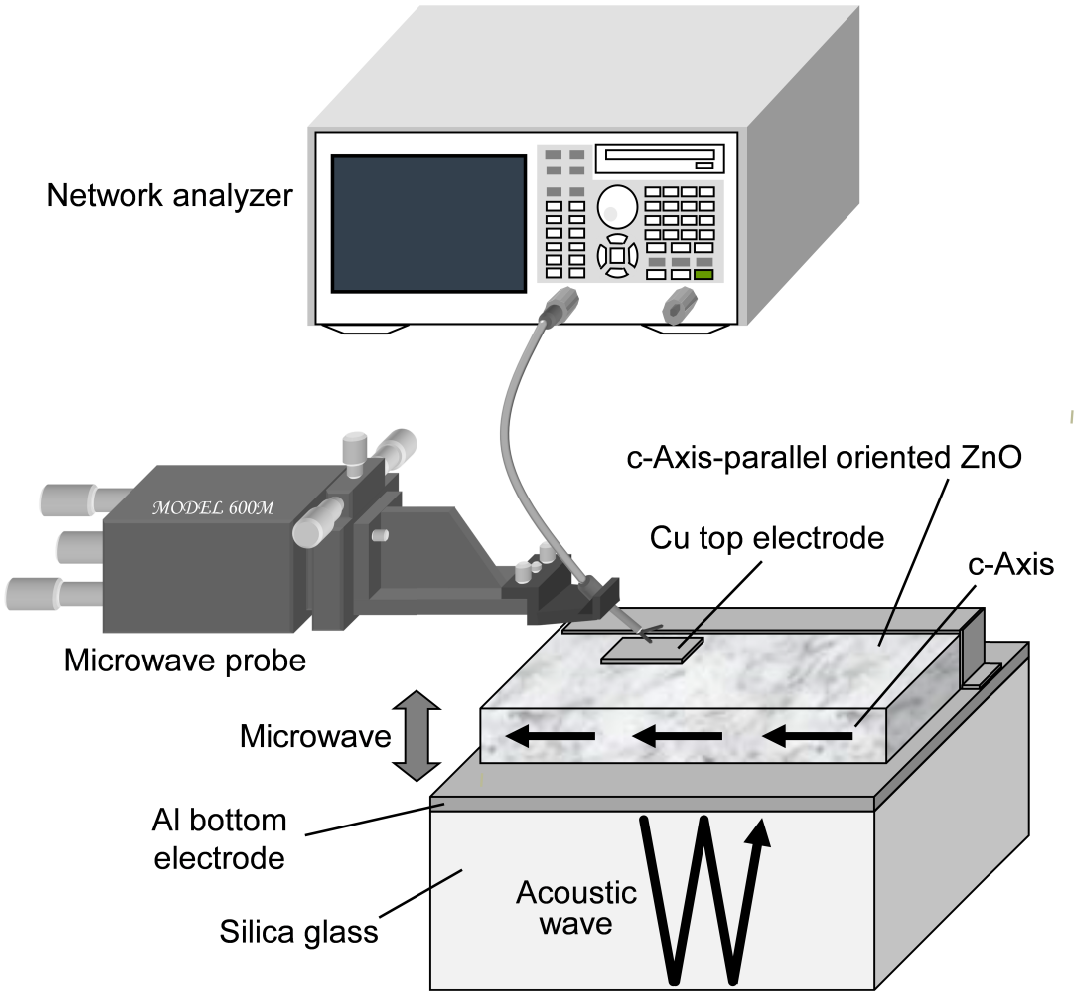

Fig. 6.7 Measurement system of reflection coefficient S_{11} by a network analyzer.

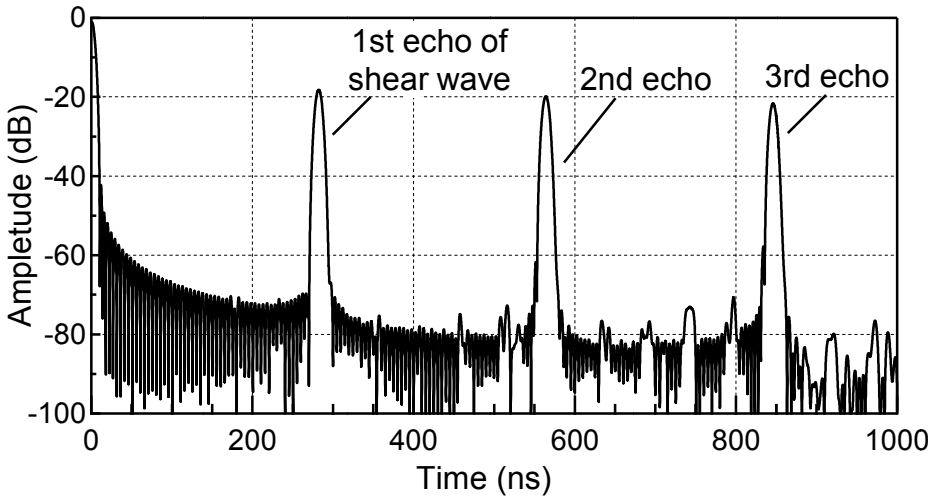

Fig. 6.8 Impulse response of the HBAR.

Table 6.1 HBAR structures of sample A and B

	A: Cu/ZnO(11$\bar{2}$0)/Al/SiO_2	B: Cu/ZnO(10$\bar{1}$0)/Al/SiO_2
Top electrode	Cu (0.25 μm)	Cu (0.10 μm)
Piezoelectric layer	(11$\bar{2}$0) oriented ZnO (4.0 μm)	(10$\bar{1}$0) oriented ZnO (2.4 μm)
Deposition method	RF magnetron sputtering	RF substrate bias sputtering
Bottom electrode	Al (0.17 μm)	Al (0.10 μm)
Substrate	Silica glass (0.5 mm)	Silica glass (0.5 mm)
Acoustic wave excitation	Shear wave	Shear wave

Figures 6.9(a) and (b) show the frequency responses of the experimental shear mode conversion loss measured in sample A and B, respectively. In Fig. 6.8(a), the minimum conversion loss was found at 320 MHz, corresponding to the fundamental thickness shear mode resonant frequency (S_1) in the ZnO film. The solid lines show the theoretical conversion losses calculated using shear-mode electromechanical coefficients of k_{15}=0.09, 0.12, and 0.15. The calculated minimum conversion loss using k_{15}=0.12 provided the best agreement with the experimental minimum conversion loss. The shear-mode electromechanical coefficient in sample A was thus estimated as k_{15}=0.12, which corresponds to 65% of that in a ZnO single crystal (k_{15}=0.26). Likewise, as shown in Fig. 6.9(b), the k_{15} value was estimated to be 0.17 in sample B, and corresponds to 46% of that in a ZnO single crystal. A discrepancy in the shape of the experimental and theoretical curves is observed at approximately 640 and 1040 MHz in Figs. 6.9(a) and 6.9(b), respectively, which corresponds to the second overtone mode resonant frequency (S_2). In the next section, the thickness of the unoriented layer was estimated by analyzing the second overtone mode resonant.

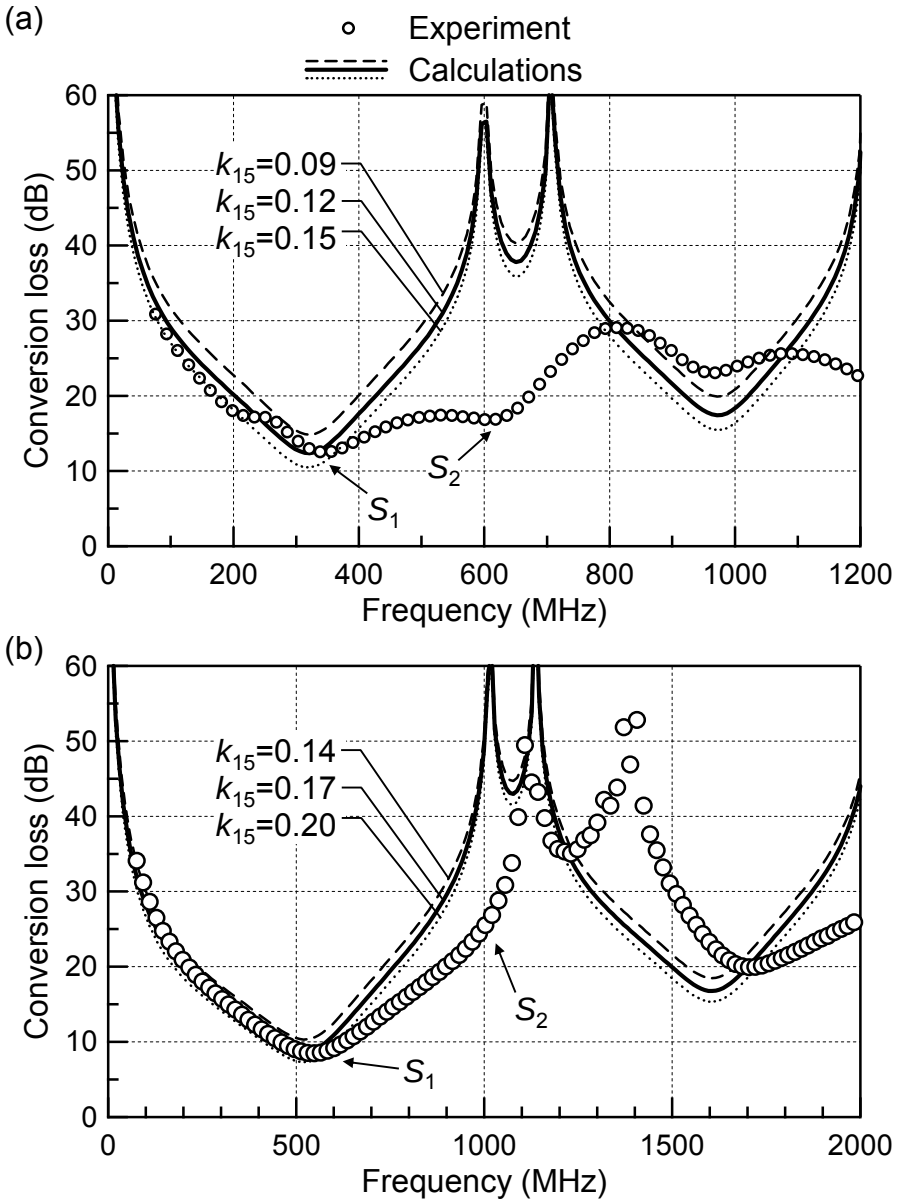

Fig. 6.9 Frequency response of the shear-mode conversion losses of (a) sample A and (b) sample B.

6.3 ESTIMATION OF THICKNESS OF UNORIENTED LAYER

To confirm the effect of the piezoelectrically-inactive layer on the conversion loss of HBAR, sample C and D were prepared as shown Table 6.2. The (0001) oriented ZnO layer can be grown on a (0001) oriented Ti electrode because of the local epitaxial relationship between ZnO(0001) and Ti(0001).

Therefore, the author predicted the piezoelectrically inactive ZnO layer would be very thin in the sample consisting of Cu/ZnO(0001)/Ti(0001)/SiO_2 (sample C). On the other hand, the sample including artificial piezoelectrically-inactive layer (sample D) was prepared. (0001) oriented Al-doped-ZnO (AZO) layer was intentionally inserted between ZnO(0001) and Ti(0001) layers. Because AZO does not exhibit a piezoelectric effect due to its low resistivity, the AZO(0001) layer behaves as a pseudo piezoelectrically-inactive-ZnO layer. The resonator consisting of the (0001) oriented ZnO film excites pure longitudinal wave.

Table 6.2 HBAR structures of sample C and D

	C: Cu/ZnO(0001)/Ti(0001) /SiO_2	D: Cu/ZnO(0001)/AZO(0001) /Ti(0001)/SiO_2
Top electrode	Cu (0.15 μm)	Cu (0.15 μm)
Piezoelectric layer	(0001) oriented ZnO (3.2 μm)	(0001) oriented ZnO (3.5 μm)
Artificial non-piezoelectric layer	———	(0001) oriented Al-doped-ZnO (0.5 μm)
Bottom electrode	(0001) oriented Ti (0.10 μm)	(0001) oriented Ti (0.10 μm)
Substrate	Silica glass (0.5 mm)	Silica glass (0.5 mm)
Acoustic wave excitation	Longitudinal wave	Longitudinal wave

The crystalline orientations of the ZnO films in sample C and D were measured with an X-ray diffractometer (PANalytical, X-Pert Pro. MRD). An intense ZnO(0002) peak was observed in the both samples. The full width at half maximum (FWHM) values of the ZnO(0002) plane ω-scan rocking curve in sample C and D were 1.3º and 1.5º, respectively.

The experimental conversion losses of the resonators were measured likewise in Section 6.2, and compared with the calculated conversion loss by using the one-dimensional mechanical transmission line model including the piezoelectrically-inactive layer in Fig. 6.6. In the theoretical model, the

author selected the electromechanical coupling coefficient k value and the velocity values of the ZnO film so that the minimum conversion loss mostly agreed with the experimental result. Then, the thickness of the piezoelectrically inactive ZnO layer d_n value was estimated.

Figures 6.10(a) and (b) shows the frequency response of the experimental longitudinal mode conversion loss in the resonator of sample A and B, respectively. The minimum conversion losses were found at 890 MHz in Fig. 6.10(a) and at 730 MHz in Fig. 6.10(b), corresponding to the fundamental longitudinal mode resonant frequency L_1. In Fig. 6.10(a), the lines show the theoretical conversion losses simulated by using transmission line model with d_n=0.0, 0.1, 0.2 and 0.3 μm. The second overtone mode resonant L_2 at 1.78 GHz was enhanced with increasing d_n values as expected. The theoretical curve at d_n=0.2 μm was in good agreement with the experimental curve. Consequently, thickness of the piezoelectrically inactive layer in the sample A was determined to be 0.2 μm. In Fig. 6.10(b), the second overtone mode resonant L_2 at 1.46 GHz was highly excited due to the artificial inactive AZO layer as expected. The theoretical curve at d_n=0.7 μm was in good agreement with the experimental curve. Considering the 0.2 μm thickness of the inactive layer in the sample A and the 0.5 μm thickness of AZO film as the artificial inactive layer, the 0.7 μm thickness of the inactive layer in the sample B is reasonable.

To estimate the thickness of the unoriented layer, likewise, as shown in Fig. 6.11(a) and 6.11(b), the d_n value was estimated in sample A and B, respectively. The theoretical curves at d_n=0.3 and 1.5 μm were in reasonable agreement with the experimental curves of sample A and B, The thicknesses of the piezoelectrically inactive layer in the sample A and B were determined to be 0.3 and 1.5 μm from the resonance characteristics, respectively.

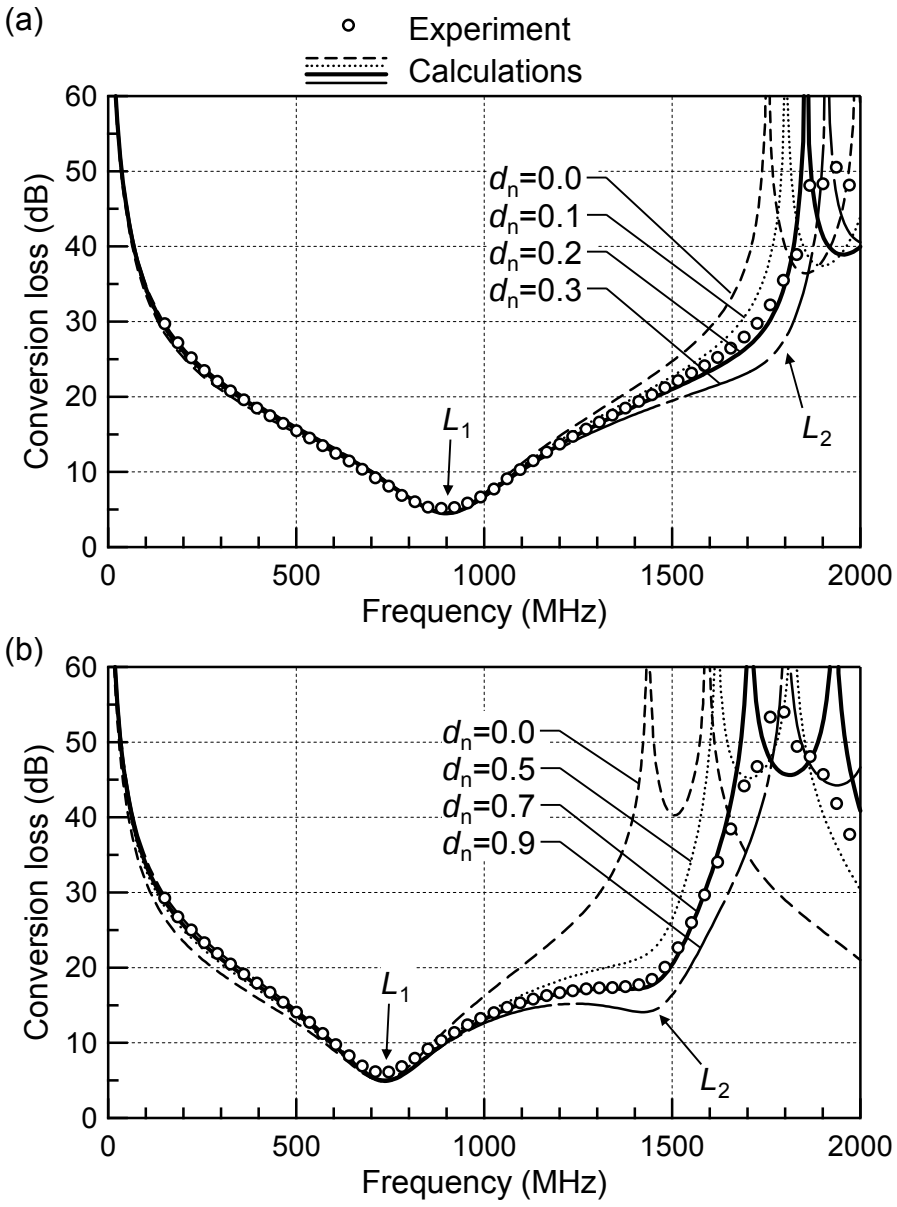

Fig. 6.10 Frequency responses of the longitudinal-mode conversion losses of (a) the ZnO(0001) film resonator (sample C) and (b) the ZnO(0001)/AZO(0001) film resonator (sample D). The simulated minimum conversion losses using k_{33}=0.23 in Fig. 6.9(a) and k_{33}=0.22 in Fig. 6.9(b) provided the best agreement with the experimental one at the fundamental thickness longitudinal mode resonant frequency L_1.

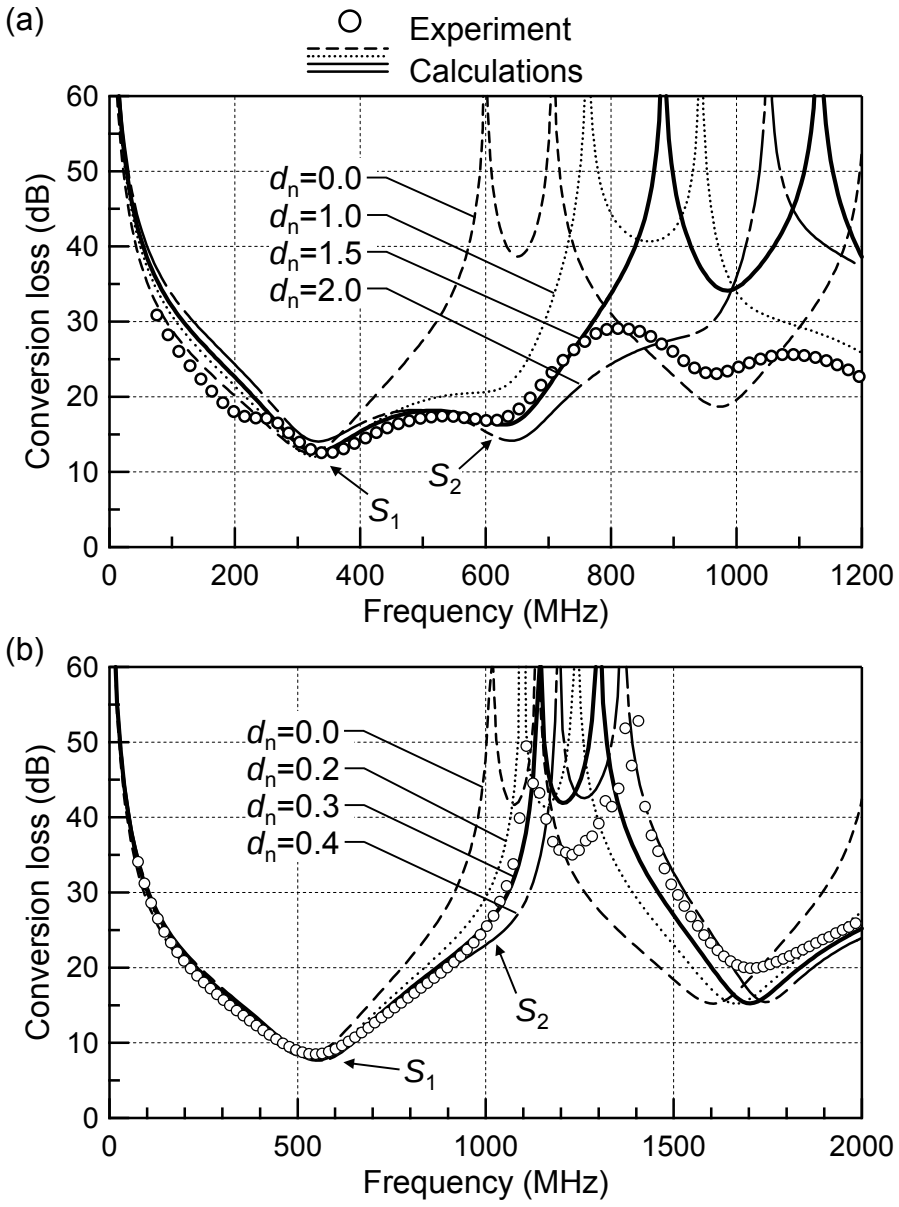

Fig. 6.11 Frequency responses of the longitudinal-mode conversion losses of (a) the ZnO($11\bar{2}0$) film resonator (sample A) and (b) the ZnO($10\bar{1}0$) film resonator (sample B). The simulated minimum conversion losses using k_{15}=0.12 in Fig. 6.10(a) and k_{15}=0.17 in Fig. 6.10(b) provided the best agreement with the experimental one at the fundamental thickness shear mode resonant frequency S_1.

ED patterns of the sample A measured at three regions surrounded by a circle in the TEM image of Fig. 6.12(a) were shown in Figs. 6.12(b)-6.12(d). The direction of the incident electron beam was normal to the $(1\bar{1}00)$ plane. A ring pattern was observed in the ED pattern at the region 0.5 μm from the Al bottom electrode, as shown in Fig. 6.12(d). The ring pattern at this region indicates the random orientation in the initial stage of the film growth. At the region 1.9 μm, although the slight ring pattern still remained, a spot pattern appeared, as shown in Fig. 6.12(c). The ring pattern disappeared and the spot pattern was clearly observed at the region 3.3 μm in Fig. 6.12(b). These results indicate good crystalline orientation at more than 1.9 μm in thickness of the ZnO$(11\bar{2}0)$ film. From this observation, the author can conclude that the thickness of the piezoelectrically inactive layer of d_n=1.5 μm estimated from resonance characteristic is reasonable. In the transmission line model proposed in Fig. 6.6, the author assumed the piezoelectrically inactive layer as a uniform structure. On the other hand, the crystalline orientation of the ZnO $(11\bar{2}0)$ film in depth direction gradually improved as the growth proceeded in Fig. 6.12. In spite of these actual conditions, these results show that the d_n value estimated from the simple theoretical model can be used as an index of the degree of the crystalline orientation in depth direction.

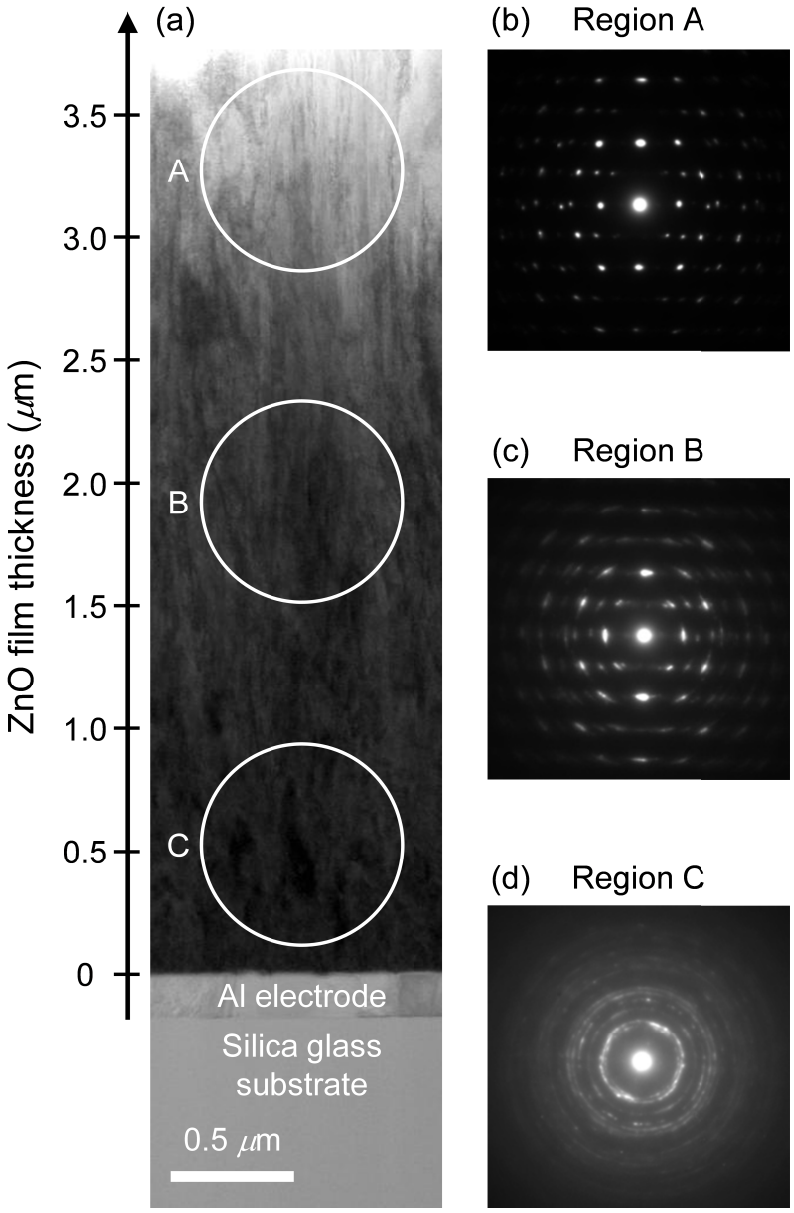

Fig. 6.12 (a) Cross-sectional TEM image of the $(11\bar{2}0)$ ZnO film (sample A) and ED patterns at the region (b) 3.3 μm (region A), (c) 1.9 μm (region B) and (d) 0.5 μm (region C) from the Al bottom electrode.

REFERENCES

[6.1] T. Yanagitani, M. Kiuchi, M. Matsukawa, and Y. Watanabe, IEEE Trans. Ultrason. Ferroelectr. Freq. Control **54**, 1680 (2007).

[6.2] T. Yanagitani, M. Kiuchi, M. Matsukawa, and Y. Watanabe, J. Appl. Phys. **102**, 024110 (2007).

[6.3] S. Nakamura, Y. Harada, and M. Seno, Appl. Phys. Lett. **58**, 2021 (1991).

[6.4] P. Kung, A. Saxler, X. Zhang, D. Walker, T. C. Wang, I. Ferguson, and M. Razeghi, Appl. Phys. Lett. **66**, 2958 (1995).

[6.5] J. B. Casady and R. W. Johnson, Solid-State Electron. **39**, 1409 (1996).

[6.6] P. Zu, Z. K. Tang, G. K. L. Wong, M. Kawasaki, A. Ohtomo, H. Koinuma, and Y. Segawa, Solid State Commun. **103**, 459 (1997).

[6.7] D. C. Look, Mater. Sci. Eng. B **80**, 383 (2001).

[6.8] E. Fortunato, P. Barquinha, A. Pimentel, A. Gonçalves, A. Marques, L. Pereira, and R. Martins, Thin solid films **487**, 205 (2005).

[6.9] A. N. Banerjee, C. K. Ghosh, K. K. Chattopadhyay, H. Minoura, A. K. Sarkar, A. Akiba, A. Kamiya, and T. Endo, Thin solid films **496**, 112 (2006).

[6.10] S. Masuda, K. Kitamura, Y. Okumura, S. Miyatake, H. Tabata, and T. Kawai, J. Appl. Phys. **93**, 1624 (2003).

[6.11] H. Hosono, Thin solid films **515**, 6000 (2007).

[6.12] T. Yanagitani and M. Kiuchi, J. Appl. Phys. **102**, 044115 (2007).

[6.13] T. Yanagitani and M. Kiuchi,
Surf. Coat. Technol. **206**, 816 (2011).

[6.14] N. F. Foster,
J. Appl. Phys. **40**, 4202 (1969).

[6.15] W. P. Mason,
Physical Acoustics (Academic New York 1964), vol. 1, part A.

[6.16] S. Takayanagi, T. Yanagitani, and M. Matsukawa,
Jpn. J. Appl. Phys. **51**, 07GC08 (2012)

[6.17] T. Yanagitani, T. Nohara, M. Matsukawa, Y. Watanabe, and T. Otani,
IEEE Trans. Ultrason. Ferroelectr. Freq. Control **58**, 1062 (2011).

[6.18] J. Kushibiki and M. Arakawa,
IEICE Tech. Rep. US2004-72 (2004) [in Japanese].

[6.19] D. B. Fraser, J. T. Krause, and A. H. Meizler,
Appl. Phys. Lett. **11**, 308 (1967).

[6.20] R. T. Smith and V. E. Stubblefield,
J. Acoust. Soc. Am., **46**, 105 (1969).

7 APPLICATION OF C-AXIS-PARALLEL ORIENTED ZnO FOR SURFACE ACOUSTIC WAVE AND LAMB WAVE DEVICES

7.1 SAW AND LAMB WAVE PROPERTIES OF C-AXIS PARALLEL ORIENTED ZnO FILM

Surface acoustic wave (SAW) devices are widely used for frequency filters in mobile communications [7.1, 7.2] and microsensors [7.3, 7.4]. The bandwidth of SAW filters and the limitation of sensitivity in SAW sensors depend on electromechanical coupling coefficient K^2 in the substrate structure. For example, SAW substrate structures with high K^2 value are required for broadband SAW filter [7.5]. On the other hand, SAW sensors such as gas sensor and ultrabiolet sensor detect velocity changes of SAW in a piezoelectric medium, and high K^2 value leads to high sensitivity in these sensors. Therefore, the SAW substrate structures with high K^2 value have been searched in many studies in order to improve the performance of these SAW devices.

Wave propagation properties depend on crystalline anisotropy of the substrate structure. Figure 7.1 shows the relationship between the direction of electric field applied to ZnO and the electromechanical coupling coefficients of bulk quasi-longitudinal wave k'_{33} and bulk quasi-shear wave k'_{35} [7.6]. If the c-axis direction corresponds to the electric field direction, the k'_{33} value reaches maximum. On the other hand, the k'_{35} value reaches maximum at the c-axis direction tilted with respect to the electric field. These results indicate the piezoelectric constant e_{33}, which is the highest value in the piezoelectric constants of ZnO, strongly contributes to both quasi-longitudinal and quasi-shear electromechanical coupling coefficients. Based on these BAW properties by the crystalline anisotropy, c-axis-parallel-oriented ZnO film could enhance the K^2 value in the case of Rayleigh mode SAW coupled with longitudinal and shear vertical (SV) wave.

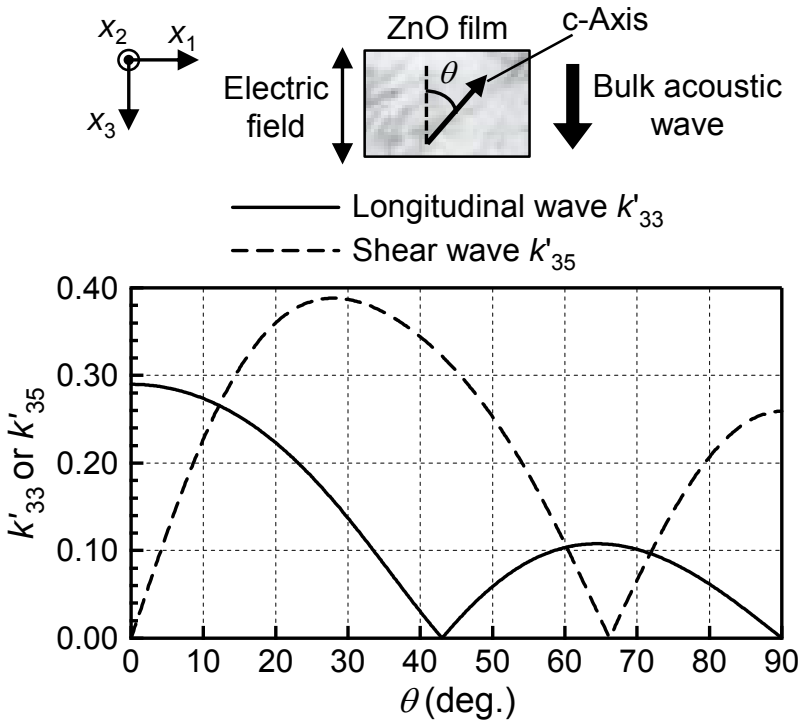

Fig. 7.1 Calculated electromechanical coupling coefficients of quasi-longitudinal wave k'_{33} and quasi-shear wave k'_{35} for ZnO as a function of the angle θ between the c-axis and electric field direction [7.6].

The K^2 value also depends on the acoustic and piezoelectric properties in the substrate material. ZnO films, which have high piezoelectric constants, have been studied for acoustic devices [7.5]. A ZnO film/silica glass substrate structure is good candidate for the SAW devices because of its low cost and relatively-high K^2 value [7.7, 7.8]. On the other hand, Si substrate is widely used for MEMS devices. SAW devices fabricated on Si have an advantage for integrated circuits. In addition, Lamb wave device can be fabricated by etching the Si substrate. Lamb wave devices usually achieve the higher electromechanical coupling than SAW devices.

At first, the SAW propagation property in an IDT/ZnO/Si substrate structure was analyzed as functions of normalized film thickness H/λ and c-axis tilt angle θ by using the Farnell and Adler's method [7.9]. The SAW propagation direction (x_1) was parallel to c-axis tilt plane (x_1-x_3) in order to

investigate the effect of the c-axis tilt, as shown in Fig. 7.1, on Rayleigh mode SAW. Physical constants of ZnO reported by Smith and Stubblefield [7.10] were used in the analysis.

Figure 7.2 shows surface plots of the calculated K^2 values of the second (Sezawa) mode SAW in IDT/ZnO/Si structure. Maximum K^2 value was found to be K^2 = 3.8% (phase velocity V = 5280 m/s) at H/λ = 0.30 and θ = 90º. θ of 90º means that the c-axis of ZnO is parallel to the substrate plane. Because the electric field parallel to the substrate plane is enhanced in this structure, highly piezoelectric effect was exhibited by the highest piezoelectric constant e_{33} at θ = 90º. Figure 7.3(a) and 7.3(b) shows the profile curves of K^2 as a function of H/λ at θ = 0º and 90º in this structure. The K^2 value of the second mode at θ = 90º and H/λ = 0.30 was also higher than that of the other mode. As a result, the second mode SAW in the IDT/c-axis parallel ZnO/Si structure is a promising candidate for SAW devices.

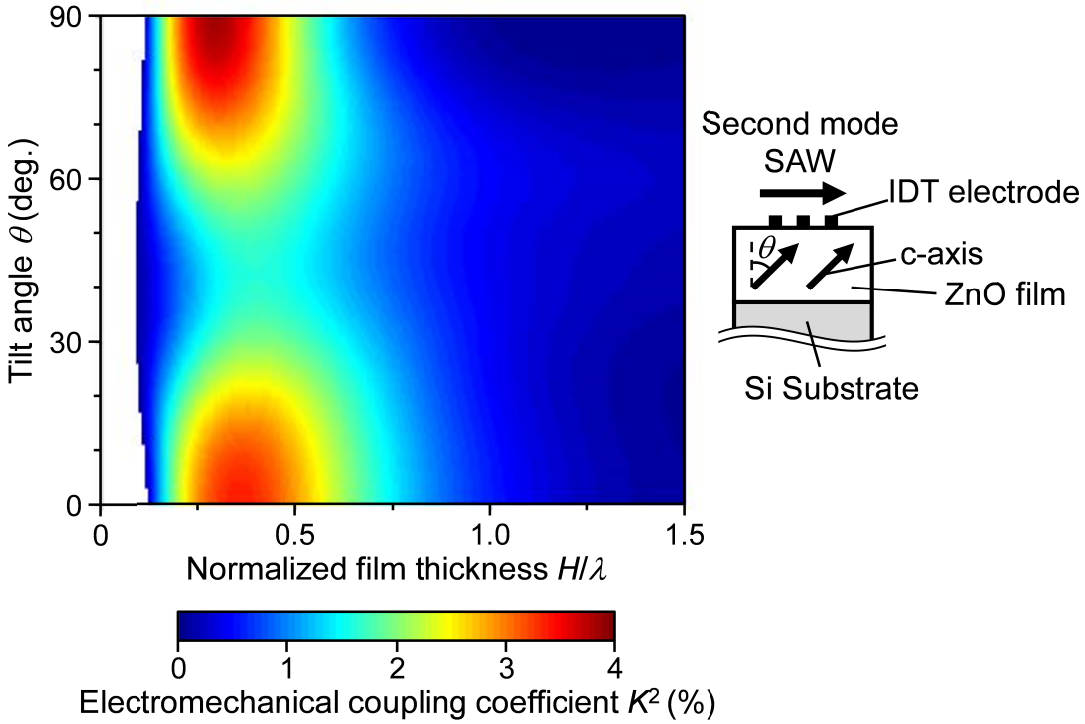

Fig. 7.2 Calculated electromechanical coupling coefficient K^2 of the second mode (Sezawa) SAW as a function of the c-axis tilt angle θ and normalized film thickness H/λ in IDT/ZnO/Si structure.

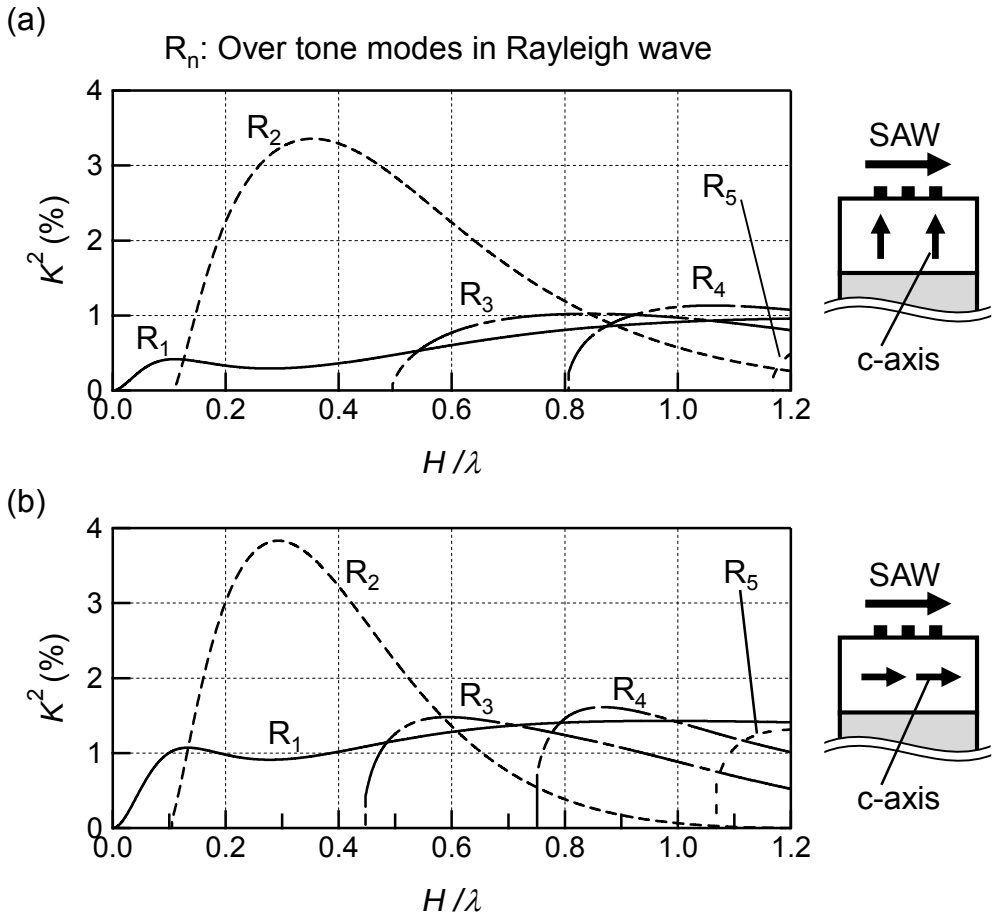

Fig. 7.3 the profile curves of K^2 as a function of H/λ at (a) $\theta = 0°$ and (b) 90° in IDT/ZnO/Si structure.

Next, the Lamb propagation properties in the ZnO film were analyzed as is the case in the SAW analysis. Figures 7.4(a) and 7.4(b) show surface plots of the calculated K^2 values of the first symmetrical Lamb wave mode (S_0) in ZnO film and ZnO film/bottom electrode, respectively, as functions of normalized film thickness H/λ and c-axis tilt angle θ. Maximum K^2 value was found to be K^2 = 10.5% (phase velocity V = 5610 m/s) at H/λ = 0.09 and θ = 90° in the ZnO film without bottom electrode. Figure 7.5 shows the profile curves of K^2 as a function of H/λ at $\theta = 0°$ and 90° in the first asymmetrical mode (A_0) and first symmetrical mode (S_0) of these structures. The K^2 value of the S_0 mode at $\theta = 90°$ and H/λ = 0.09 was also higher than that of the other mode. As a result, the S_0 mode Lamb wave in the c-axis parallel ZnO can be of great interest for the applications.

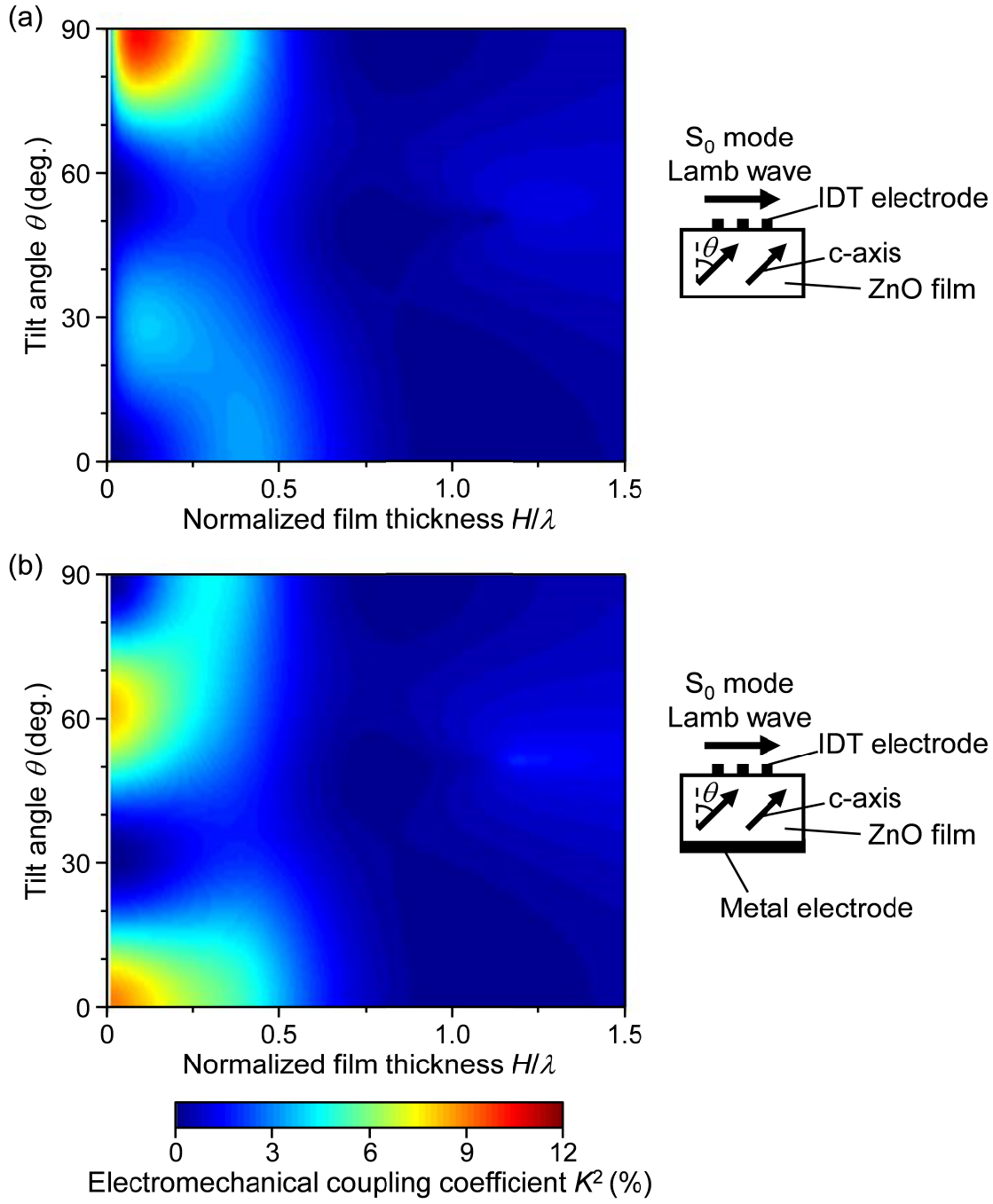

Fig. 7.4 Calculated K^2 values of the first symmetrical Lamb wave mode (S_0) in (a) ZnO film and (b) ZnO film/bottom electrode, respectively, as functions of normalized film thickness H/λ and c-axis tilt angle θ.

ZnO films which c-axis is normal to the substrate plane are generally used in acoustic wave devices, because wurtzite structure film including ZnO tends to grow in c-axis normal (0001) orientation [7.11]. However, in Chapters 3

and 4, c-axis-parallel-oriented ZnO films could be grown without epitaxial technique. Next section, a first attempt to fabricate the Lamb device using the c-axis-parallel-oriented ZnO film will be demonstrated.

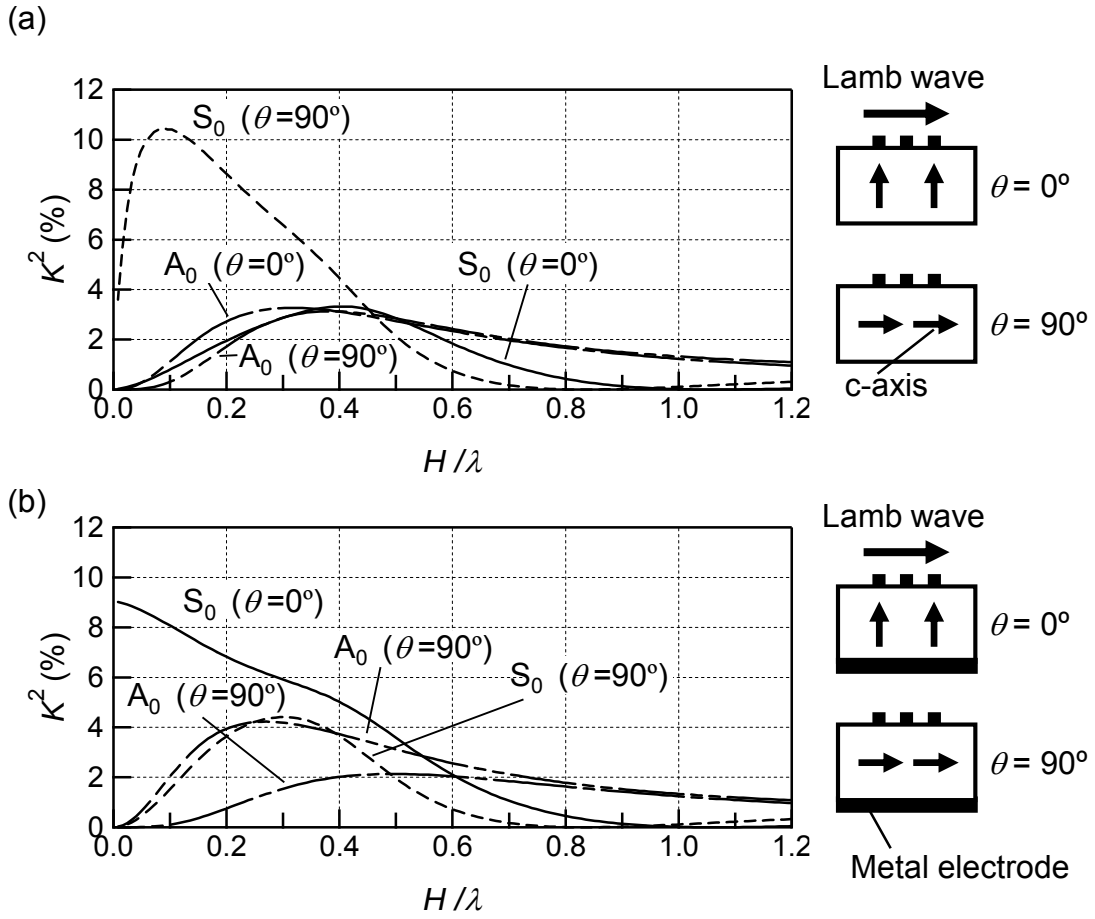

Fig. 7.5 Profile curves of K^2 as a function of H/λ at θ = 0º and 90º in the first asymmetrical mode (A_0) and first symmetrical mode (S_0) of (a) ZnO film and (b) ZnO film/bottom electrode

7.2 SAW AND LAMB WAVE DEVICE FABRICATIONS

First, a c-axis parallel oriented ZnO film was deposited on a Si substrate by an RF magnetron sputtering system likewise in Chapter 3. Table 7.1 shows a deposition conditions. The film thickness of the sample was 2.3 μm above the target erosion area.

The crystalline orientations of the ZnO film were determined by XRD measurement. Figures 7.6 show a XRD pattern of the sample above the erosion area. An intense $(11\bar{2}0)$ peak was observed, and the FWHM value of the ZnO $(11\bar{2}0)$ plane ω-scan rocking curve was 4.6º. Therefore, the c-axis-parallel oriented film can be also grown on a Si substrate using the conventional RF magnetron sputtering system.

Table 7.1 Deposition conditions is grown on a Si substrate in RF magnetron sputtering

Total gas pressure	0.1, 1.0 Pa
Ar / O_2	1 / 3
RF power	13.56 MHz, 200 W
Deposition time	1 h 50 min
Film thickness	2.3 μm

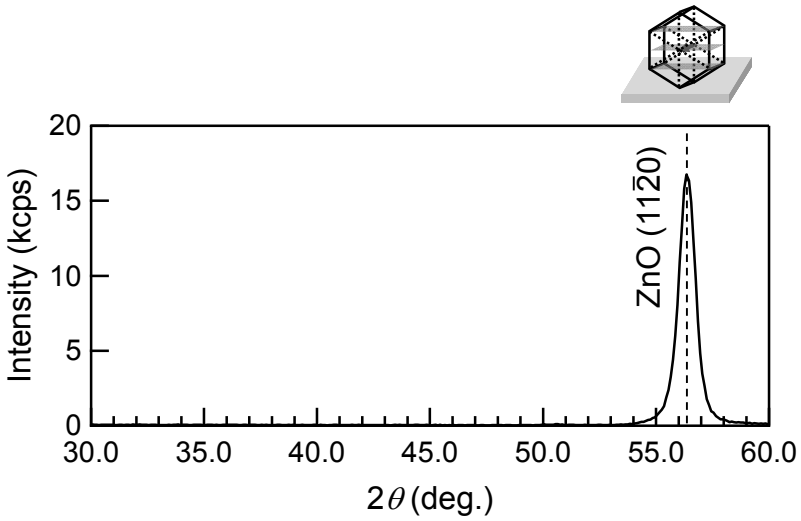

Fig. 7.6 XRD pattern of the sample on Si substrate.

Next, Al/Ti IDTs with the wavelength of 8 μm were fabricated on the sample to excite SAWs. The c-axis direction corresponded to the wave propagation direction. Figures 7.7(a) and 7.7(b) show the IDT configurations

and optic-microscopic image of the IDT structure. An insertion loss of the sample was measured by a network analyzer to investigate the propagation characteristics of SAWs as shown in Fig. 7.8. The strongest peak was observed at the center frequency (f_1) of 575 MHz. The phase velocity of the acoustic wave was roughly estimated to be 4850 m/s at the wavelength of 8 μm. To determine the wave mode, SAW velocities calculated as a function of normalized film thickness H/λ were plotted in Fig. 7.9. Compared with the experimental value of the velocity, the second (Sezawa) mode SAW was probably excited. One possible reason for the difference between the experimental and calculated values is that the density of the c-axis-parallel oriented film was lower than that of single crystal ZnO used in the calculation.

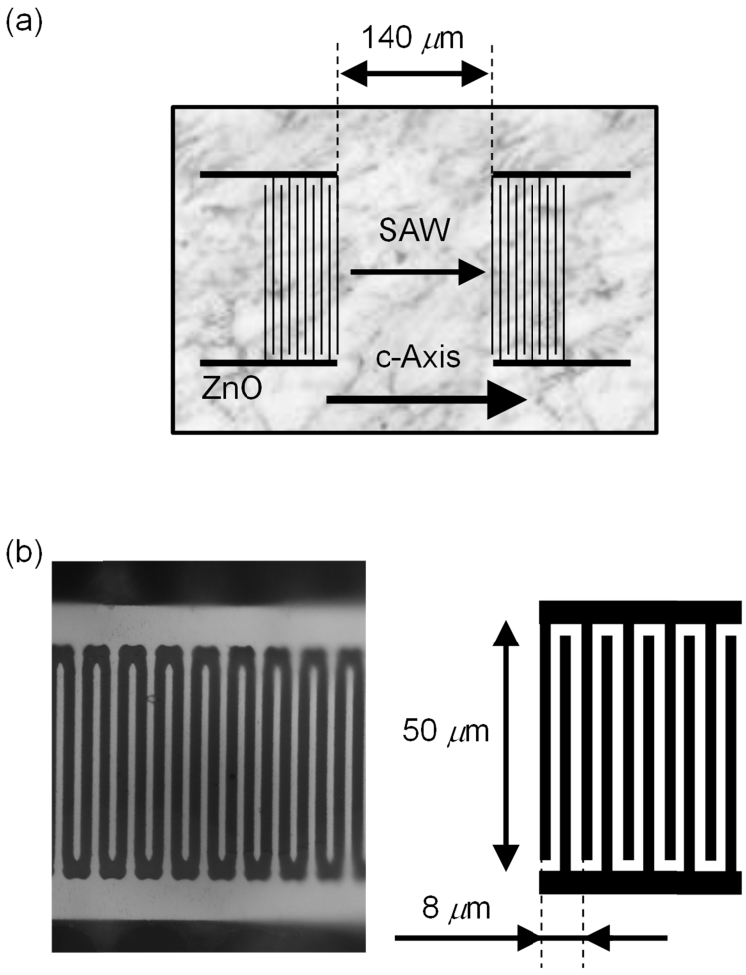

Fig. 7.7 (a) IDT configurations and (b) optic-microscopic image of the IDT structure.

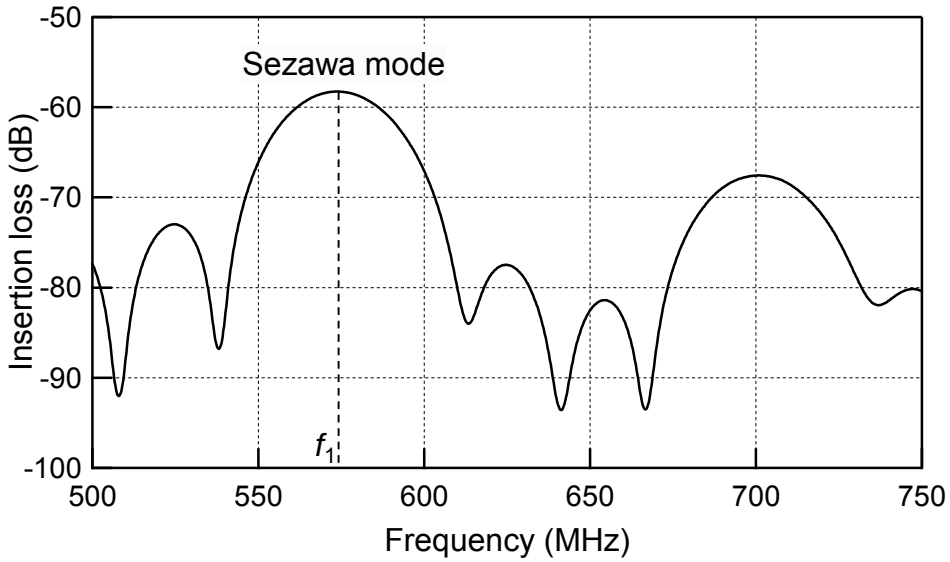

Fig. 7.8 Insertion loss characteristic observed in the Al/Ti IDT/c-axis-parallel-oriented ZnO/Si substrate structure.

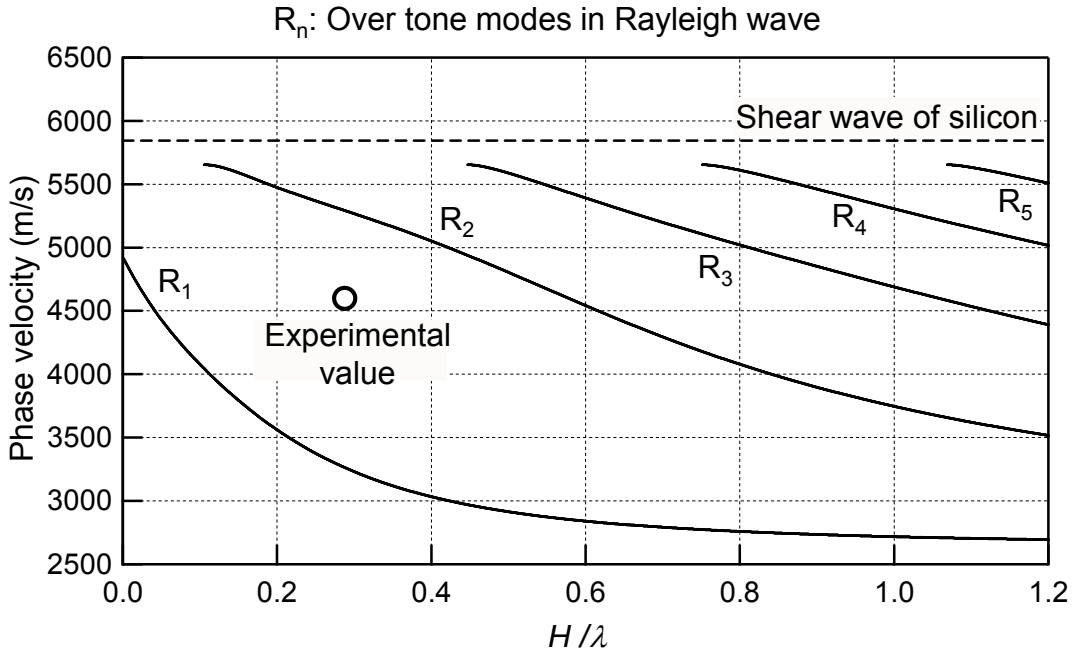

Fig. 7.9 SAW velocities calculated as a function of normalized film thickness H/λ.

Finally, the Si substrate was etched to fabricate a Lamb wave device. Figure 7.10 shows an optic-microscopic image of the Al/Ti IDT/c-axis-parallel ZnO membrane structure. Likewise, an insertion loss of the sample was measured to investigate the propagation characteristics of Lamb waves as shown in Fig. 7.11. The strongest peak was observed at the center frequency of 606 MHz, and the phase velocity was estimated to be 4850 m/s. Lamb wave velocities calculated as a function of normalized film thickness H/λ were plotted in Fig. 7.12. Compared with the experimental value of the velocity, the first symmetrical mode Lamb wave (S_0) was excited. The difference between the experimental and calculated values also indicated the lower density of the c-axis-parallel oriented film. The minimum insertion loss of the S_0 mode in the Lamb device was about 3 dB higher than that of the Sezawa mode in the SAW device. Therefore, the Lamb device has higher electromechanical coupling coefficient K^2 than the SAW device.

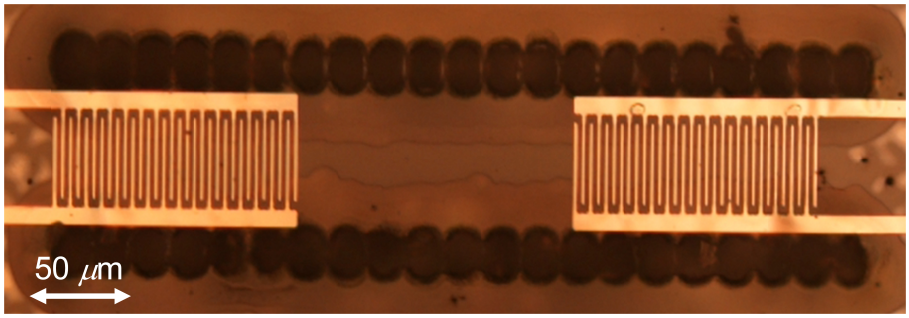

Fig. 7.10 Optical-microscopic image of the Al/Ti IDT/c-axis-parallel-oriented ZnO membrane structure.

Although further investigations of the fabrication methods and device properties are required, the c-axis-parallel-oriented film can be applied to Lamb devices. For an additional application, the high frequency magneto-elastic coupling in multilayered structure including the c-axis-parallel-oriented ZnO membrane and magnetostrictive thin film can be of great interest [7.12].

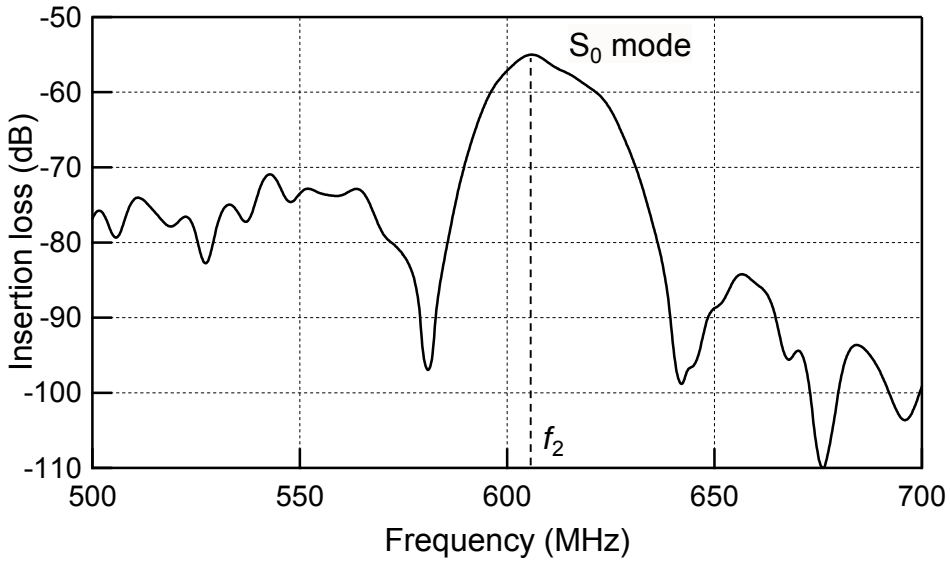

Fig. 7.11 Insertion loss characteristic observed in the Al/Ti IDT/c-axis-parallel-oriented ZnO membrane structure.

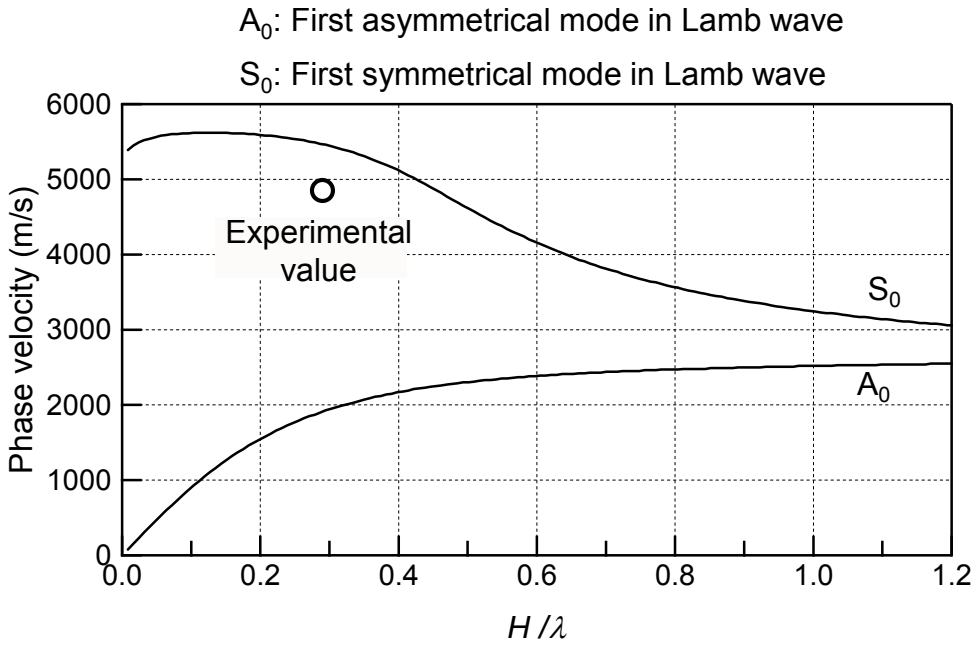

Fig. 7.12 Lamb wave velocities calculated as a function of normalized film thickness H/λ.

REFERENCES

[7.1] Y. Yoshino, T. Makino, Y. Katayama, and T. Hata,
Vacuum **59**, 538 (2000).

[7.2] M. Kadota,
Jpn. J. Appl. Phys. **44**, 4285 (2005).

[7.3] E. J. Staples and S. Viswanathan,
Ind. Eng. Chem. Res. **47**, 8361 (2008).

[7.4] S. Kumar, G. Kim, K. Sreenivas, and R.P. Tandom,
J. Electroceram. **22**, 198 (2009).

[7.5] K. Hashimoto, S. Sato, A. Teshigahara, T. Nakahara, and K. Kano,
IEEE Trans. Ultrason. Ferroelectr. Freq. Control **60**, 637 (2013).

[7.6] T. Yanagitani, N. Morisato, S. Takayanagi, M. Matsukawa, and Y. Watanabe,
IEEE Trans. Ultrason. Ferroelect. Freq. Control **58**, 1062 (2011).

[7.7] M. Kadota and C. Kondoh,
IEEE Trans. Ultrason. Ferroelect. Freq. Control **44**, 658 (1997).

[7.8] A. Tanaka, T. Yanagitani, M. Matsukawa, and Y. Watanabe,
IEEE Trans. Ultrason. Ferroelect. Freq. Control **55**, 2709 (2008).

[7.9] G. W. Farnell and E. L. Adler,
Physical Acoustics, edited by W. P. Mason and R. N. Thurston (Academic, New York, 1972) Vol. 9, p.35.

[7.10] R. T. Smith and V. E. Stubblefield,
J. Acoust. Soc. Am., **46**, 105 (1969).

[7.11] S. Muthukumar, C.R. Gorla, N.W. Emanetoglu, S. Liang, and Y. Lu,
J. Cryst. Growth **225**, 197 (2001).

[7.12] N. Tiercelin, A. Talbi, V. Preobrazhensky, P. Pernod, V. Mortet, K. Haenen, and A. Soltani,
Appl. Phys. Lett. **93**, 162902 (2008).

8. CONCLUSIONS

In conclusion, the unusual crystalline growth of ZnO film induced by the negative ion bombardment in the RF magnetron sputtering has been investigated. The unusual $(11\bar{2}0)$ preferred orientation appeared on the target erosion area with decreased gas pressure from 1 Pa to 0.1 Pa. The amount of negative ion flux in low gas pressure of 0.1 Pa, where mean free path is long, was twice as large as that in 1 Pa on the target erosion area. By comparing these results, it was indicated that the highly-crystallized $(11\bar{2}0)$ ZnO film was obtained at the area where a large amount of energetic negative ion O^- bombardment (170-250 eV) exist. This ion bombardment technique is promising for the unusual crystalline growth of various oxide films.

The author also investigated quantitative information of relationship between the RF bias power, amount of ion flux, ion energy and crystalline orientation of ZnO in RF substrate bias sputtering. The usual (0001) orientation changed into the $(11\bar{2}0)$ preferred orientation with 2 MHz RF bias power of 10 W, where the peak value of O_2^+ energy was 180 eV. The $(11\bar{2}0)$ preferred orientation then changed into the $(10\bar{1}0)$ preferred orientation with increasing RF bias power of 20 W at O_2^+ energy of 250 eV. The highly-energetic positive ion irradiation by high RF bias power induced c-axis-parallel orientation in ZnO film. RF substrate bias method is useful for orientation control of polycrystalline films.

Finally, the author investigated the potentiality of the c-axis-parallel-oriented ZnO films for guided acoustic waves including surface and Lamb acoustic waves, experimentally and theoretically. Values of K^2 can be theoretically achieved up to 3.8% for the second Rayleigh mode SAW in the ZnO film/Si substrate structure and 10.5% for the first symmetrical mode Lamb wave in the ZnO membrane. Then, Sezawa SAW and first symmetrical mode Lamb wave were experimentally excited. Applications for the acoustic devices which have the high K^2 are expected.

APPENDIX

A EFFECT OF METAL AND OXIDE MODE OF Zn TARGET ON c-AXIS-PARALLEL-ORIENTED ZnO FILM GROWTH IN A REACTIVE MAGNETRON SPUTTERING

A.1 INTRODUCTION

ZnO polycrystalline films have attracted considerable interest in piezoelectric devices and sensors [A.1-A.10]. ZnO films have a strong tendency to develop a c-axis normal orientation [(0001) orientation]. c-Axis normal oriented films are widely used for microwave frequency resonators and filters based on acoustic longitudinal wave and Rayleigh-type surface acoustic wave [A.1-A.5]. In contrast, unusual c-axis parallel oriented films [$(10\bar{1}0)$ or $(11\bar{2}0)$ oriented films] are suitable for acoustic shear wave and surface-horizontal-type surface acoustic wave excitation [A.8-A.10]. These films are promising for the sensors to measure mass loading in the liquid.

In previous study, c-axis-parallel-oriented ZnO films could be grown by using an RF magnetron sputtering of a ZnO ceramic target without use of epitaxial growth techniques, and the effects of sputtering gas conditions on the development of c-axis parallel $(11\bar{2}0)$ orientation have been investigated [A.11]. This orientation appears under the conditions of low gas pressure (< 0.1 Pa) and high oxygen gas concentration. A probable reason is the high-energy oxygen negative ions generated at the ZnO target. These negative ions easily bombard the substrate during the deposition under the low gas pressure where the mean free pass is long. The $(11\bar{2}0)$ preferentially develop was due to the anisotropy of damage tolerance for ion bombardment among crystal plane. The most densely packed (0001) plane should incur more damage by ion bombardment than the $(11\bar{2}0)$ planes. Therefore, the ion bombardment during deposition suppresses the usual (0001)-oriented grain growth, resulting in the preferential development of the $(11\bar{2}0)$ orientation instead of the (0001) orientation [A.12-A.14].

In general, a ZnO ceramic target or a Zn metal target is used as a

sputtering target in a ZnO film deposition. A ceramic target have been used in the c-axis parallel oriented film deposition because fully oxidized ZnO films can be easily obtained. However, quality of the films varies according to different ZnO ceramic target. On the other hand, in terms of cost effectiveness, workability, and high purity, a metal targets are used in a reactive sputtering method for oxide films. It is well known that transition between metal mode and oxide mode occurs on the metal target surface according to the condition of oxygen gas flow rates and applied DC or RF power [A.15-A.19].

In this appendix, effects of metal mode and oxide mode on the unusual c-axis parallel oriented ZnO films in a reactive sputtering of Zn metal target were investigated. The author predicted that highly crystallized $(11\bar{2}0)$ orientations are obtained in the oxide mode because more oxygen ion bombardment to the substrate is expected in the oxide mode than the metal mode. Two types of samples deposited under the metal mode and the oxide mode were prepared. The transition between these modes was controlled by adjusting the target temperature without changing conditions of oxygen gas flow rates and applied RF power, because these deposition parameters have a great effect on the degree of the $(11\bar{2}0)$ orientation [A.11]. Influence between the metal mode and the oxide mode on the crystalline orientation were investigated.

A.2 ZnO FILM FABRICATIONS

Figure A.1 shows an RF magnetron sputtering apparatus with a neodymium magnet used in the experiment. ZnO films were deposited on silica glass substrates (25×75×1 mm^3, Tosoh, ED-B) with an evaporated aluminum electrode thin layer. The substrate holder was cooled by water, so that substrate temperature was 100-200 ºC. A Zn metal disc (80 mm diameter, Furuuchi Chemical Co.) was used as a sputtering target and fixed on the water-cooled cathode with a bolt. The target temperature were controlled by the degree of tightening of the bolt. When the Zn target was tightly bolted on

the cathode, the Zn target surface was cold because of heat transfer from the cathode to the Zn target. In this case, the Zn target surface was in the metal mode. On the other hand, when the Zn target was loosely bolted on the cathode, its surface was in the oxide mode. Table A.1 shows the deposition conditions. Two types of samples deposited in the metal mode and the oxide mode were prepared. Figure A.2 (a) and (b) shows the images of target surfaces in the case of the metal mode and the oxide mode. Target temperature was monitored by an infrared radiation thermometer. Target surface start to oxidize at 300 ºC, and when the temperature exceeded 340 ºC, Zn target start to sublime, in present RF power and gas pressure condition shown in Table I.

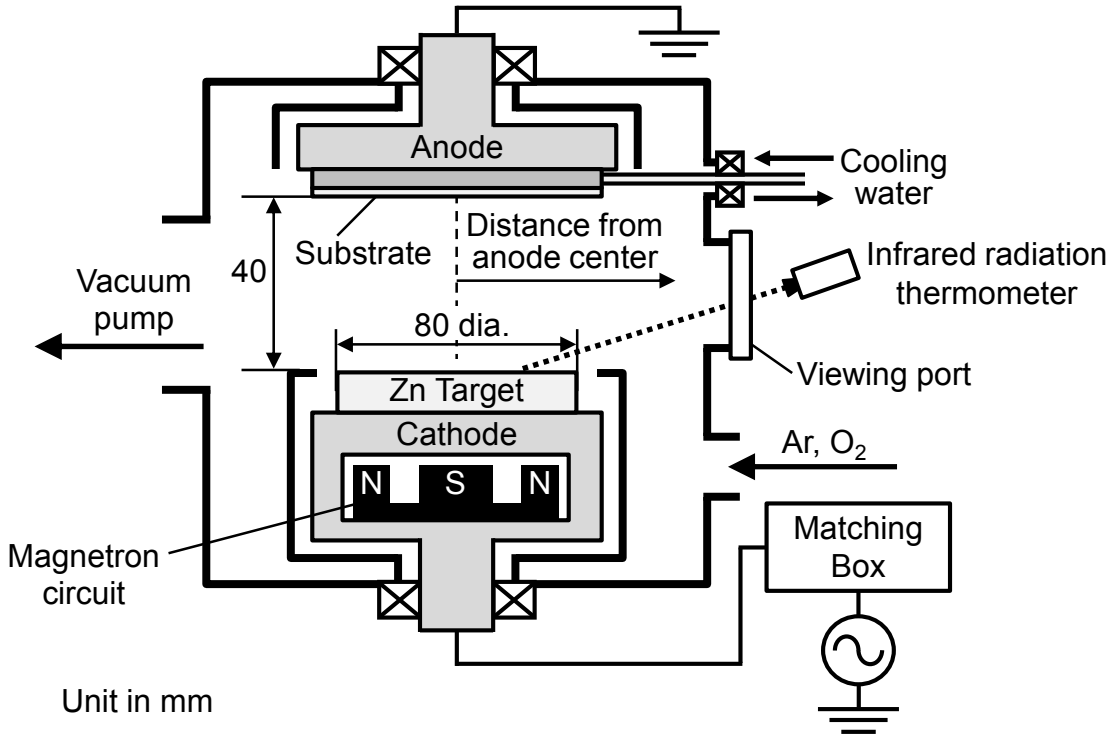

Fig. A.1 Reactive RF magnetron sputtering system for fabricating c-axis parallel oriented ZnO films.

Film samples were visually clear and transparent. Film thicknesses of the samples in metal mode and in oxide mode were 6.4 and 4.1 μm, respectively, at 30 mm from the anode center. The deposition rate in the oxide mode is

generally lower than that in the metal mode in reactive sputtering because the sputtering rate of an oxide is lower than that of metals [A.20]. The difference of these thicknesses is due to the transition between the metal mode and the oxide mode.

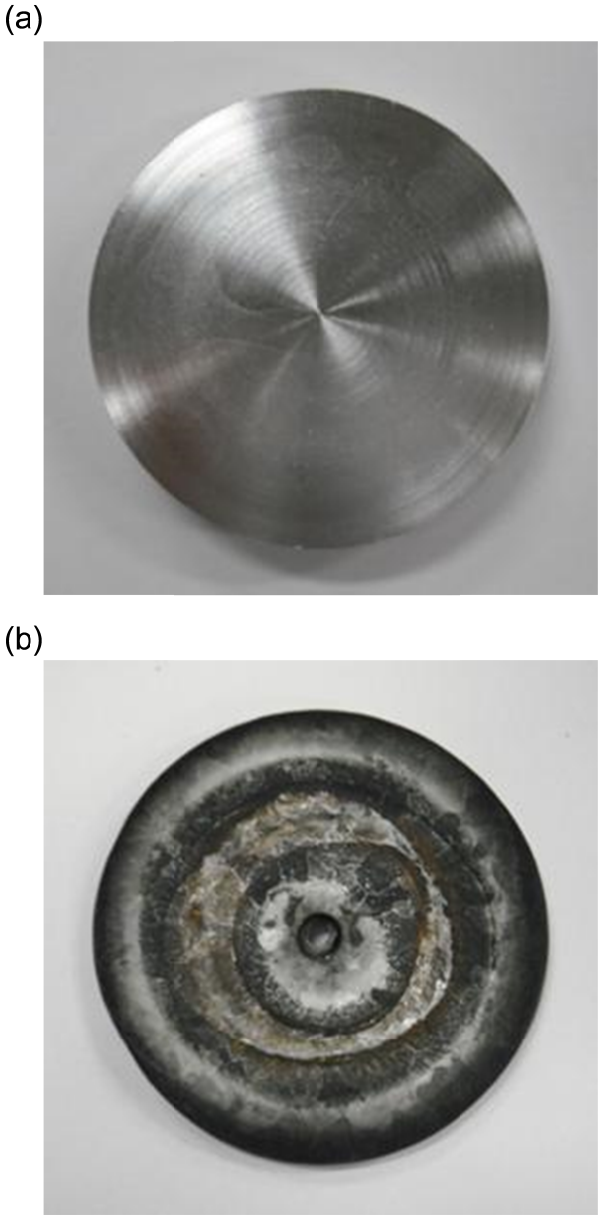

Fig. A.2 Zn target used in the sputtering deposition (a) in the metal mode and (b) the oxide mode. Temperatures of the target surface in the metal mode and the oxide mode were adjusted to 300 ºC and 340 ºC, respectively.

Table A.1 Deposition conditions for ZnO films

RF power	13.56 MHz, 200 W
Zn target	Metal mode or oxide mode
Total gas pressure	0.1 Pa
Gas	O_2
Target-substrate distance	40 mm
Deposition time	3 hours

A.3 CRYSTALLINE ORIENTATIONS OF ZnO FILMS

The crystalline orientations of the samples were measured by 2θ–ω scan XRD patterns using an x-ray diffractometer (PANalytical, X-Pert Pro MRD). These measurements were performed on each sample at 5 mm intervals to 50 mm from the anode center.

Figure A.3(a) and A.3(b) shows the XRD patterns of the samples deposited in the metal mode and the oxide mode, respectively. $(11\bar{2}0)$ peaks observed in both samples indicate c-axis parallel orientation. Intense $(11\bar{2}0)$ peaks were observed in the sample in the oxide mode around 25 mm from the anode center, compared with the peaks in the sample in the metal mode. In addition, the degree of the $(11\bar{2}0)$ preferred orientation of the samples was evaluated from the full width at half maximum (FWHM) of the $(11\bar{2}0)$ plane ω-scan rocking curve, as shown in Fig. A.4. FWHM values of sample in the oxide mode also showed higher crystalline alignments than that of the sample in the metal mode.

In a previous report, Tominaga et al. have investigated the flux of the energetic oxygen ions in the reactive sputtering of the Zn target [A.21, A.22]. These oxygen ions were mainly generated by the sputtering of the oxidized part of the Zn target. The reason for higher $(11\bar{2}0)$ crystalline orientation in oxide mode may be due to the oxygen bombardment. Actually, higher $(11\bar{2}0)$ crystalline orientation appeared around the target erosion area (30 mm from

anode center) where a large amount of energetic oxygen ions generates owing to the magnetron circuit. The FWHM value in the oxide mode at 30 mm from anode center was 5.4º. This FWHM value shows good crystalline alignment as well as that in the previous samples deposited using ZnO ceramic target [A.11].

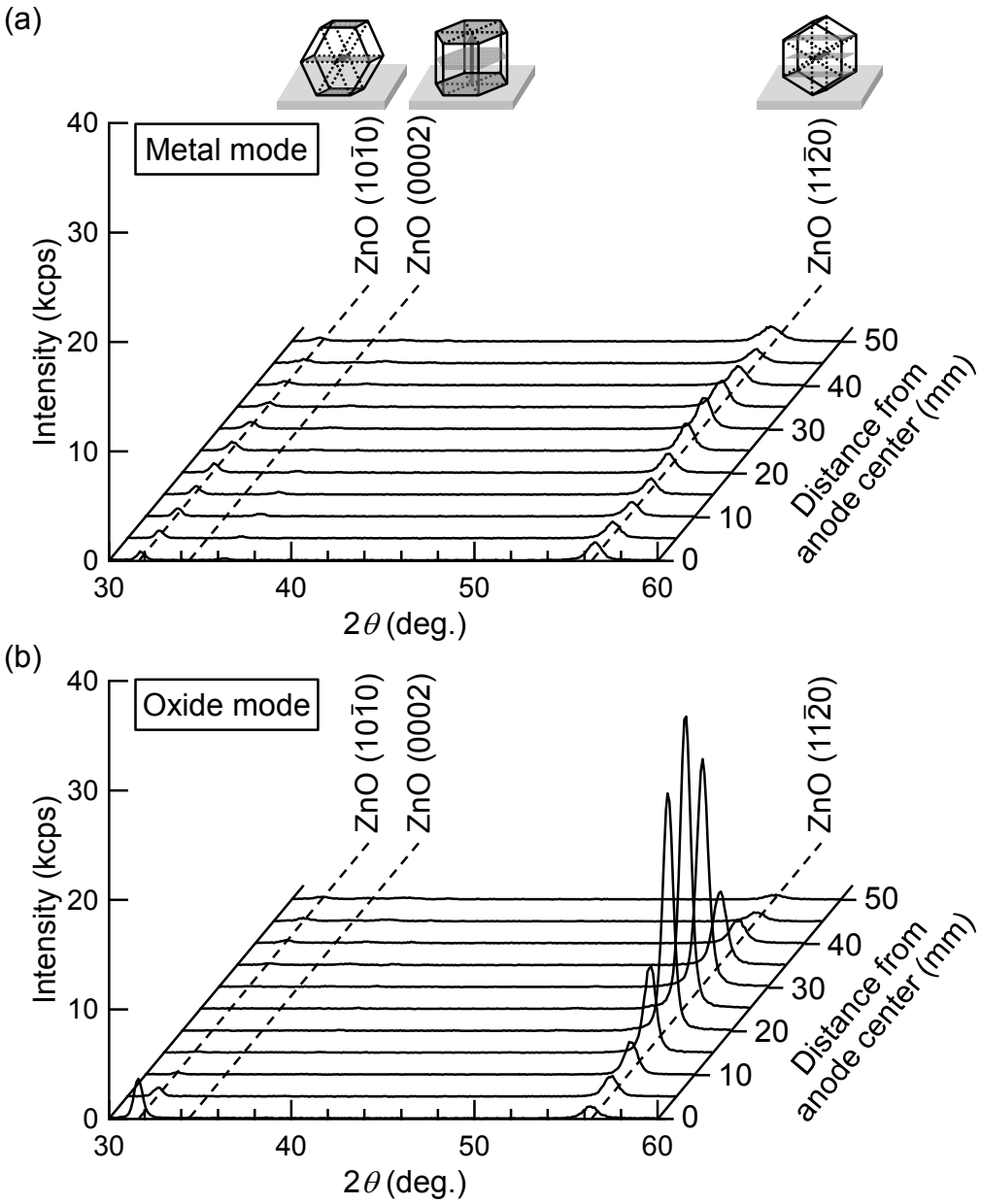

Fig. A.3 2θ–ω scan XRD patterns of the ZnO films deposited (a) in the metal mode and (b) in the oxide mode of the Zn target.

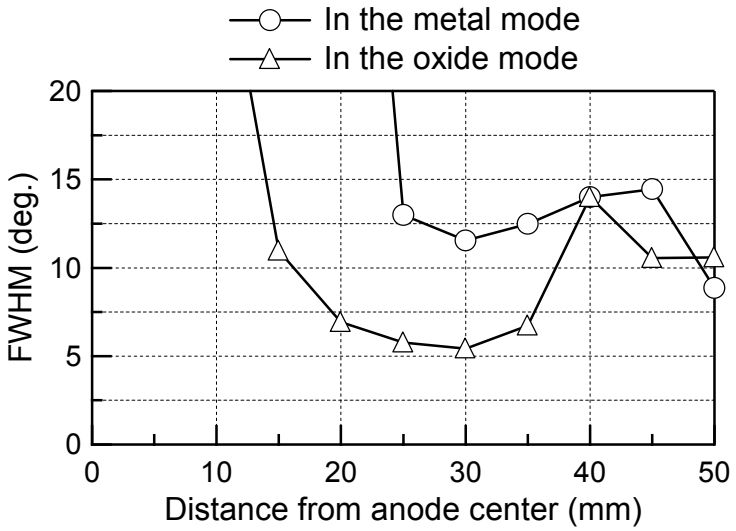

Fig. A.4 FWHM of the $(11\bar{2}0)$ plane ω–scan rocking curve in the ZnO films deposited in the metal mode and in the oxide mode.

A.4 CONCLUSIONS

The effects of the ZnO film depositions in the metal mode and the oxide mode on the c-axis parallel $(11\bar{2}0)$ orientation have been investigated by reactive sputtering of a Zn target. Strong preferred $(11\bar{2}0)$ orientation appeared in the sample deposited in the oxide mode. It may be caused by the excessive supply of energetic oxygen species generated from the surface of a fully oxidized target. It is possible that the crystalline orientation of oxide film is controlled by the difference of the supply of energetic oxygen species between the conditions in the metal mode and in the oxide mode.

REFERENCES

[A.1] F. S. Hickernell,
IEEE Trans. Sonics Ultrason. **32**, 621 (1985).

[A.2] R. Weigel, D. P. Morgan, J. M. Owens, A. Ballato, K. M. Lakin, K. Hashimoto, and C. C. W. Ruppel,
IEEE Trans. Microwave Theory Tech. **50**, 738 (2002).

[A.3] K. M. Lakin,
IEEE Trans. Ultrason. Ferroelectr. Freq. Control **52**, 707 (2005).

[A.4] M. Kadota,
Jpn. J. Appl. Phys. **44**, 4285 (2005).

[A.5] Y. Yoshino,
J. Appl. Phys. **105**, 061623 (2009).

[A.6] J. S. Wang, and K. M. Lakin,
Appl. Phys. Lett. **42**, 352 (1983).

[A.7] T. Yanagitani, N. Morisato, S. Takayanagi, M. Matsukawa, and Y. Watanabe,
IEEE Trans. Ultrason. Ferroelectr. Freq. Control **58**, 1062 (2011).

[A.8] T. Yanagitani, M. Kiuchi, M. Matsukawa, and Y. Watanabe,
J. Appl. Phys. **102**, 024110 (2007).

[A.9] T. Yanagitani, M. Kiuchi, M. Matsukawa, and Y. Watanabe,
IEEE Trans. Ultrason. Ferroelectr. Freq. Control **54**, 1680 (2007).

[A.10] A. Tanaka, T. Yanagitani, M. Matsukawa, and Y. Watanabe,
IEEE Trans. Ultrason. Ferroelectr. Freq. Control **55**, 2709 (2008).

[A.11] S. Takayanagi, T. Yanagitani, and M. Matsukawa,
Appl. Phys. Lett. **101**, 232902 (2012).

[A.12] W. Ensinger.
Nucl. Instrum. Methods Phys. Res. B **106**, 142 (1995).

[A.13] T. Yanagitani, and M. Kiuchi,
J. Appl. Phys. **102**, 044115 (2007).

[A.14] T. Yanagitani, and M. Kiuchi,
Surf. Coat. Technol. **206**, 816 (2011).

[A.15] K. Kumeta, H. Ono, and S. Iizuka,
Thin Solid Films **518**, 3522 (2010).

[A.16] D.K. Hohnke, D.J. Schmatz, and M.D. Hurley,
Thin Solid Films **118**, 301 (1984).

[A.17] F. Fenske, W. Fuhs, E. Nebauer, A. Schöpke, B. Selle, and I. Sieber,
Thin Solid Films **343-344**, 130 (1999).

[A.18] K. Tominaga, T. Kikuma, K. Kusaka, and T. Hanabusa,
Vacuum **66**, 279 (2002).

[A.19] Y. Abe, K. Shinya, Y. Chiba, M. Kawamura, and K. Sasaki,
Vacuum **84**, 1365 (2010).

[A.20] M. Scherer, and P. Wirz,
Thin Solid Films **119**, 203 (1984).

[A.21] K. Tominaga, Y. Sueyoshi, H. Imai, and M. Shirai,
Jpn. J. Appl. Phys. **31**, 3009 (1992).

[A.22] K. Tominaga, T. Murayama, Y. Sato, I. Mori,
Thin Solid Films **343-344**, 81 (1999).

B WIDEBAND MULTIMODE TRANSDUCER CONSISTING OF c-AXIS TILTED ZnO/c-AXIS NORMAL ZnO MULTILAYER

B.1 INTRODUCTION

Wideband ultrasonic transducers are required for acoustic imaging [B.1-B.6]. They can be used to determine the qualitative and quantitative properties of cells and bulk tissue [B.1-B.3, B.5]. Wideband detector response is essential for imaging reconstruction of multiscale objects using a range of characteristic acoustic wavelengths [B.2]. However, the frequency bandwidth is narrow in the case of a conventional thickness-mode transducer, because even-order overtones cannot be excited. Nakamura *et al.* have reported the fabrication of a wideband VHF transducer using a ferroelectric inversion layer formed by the heat treatment of a $LiNbO_3$ plate [B.7-B.9]. An electric field applied across the plate can excite a second-overtone mode as well as a fundamental mode. The combination of these mode excitations makes a wideband excitation possible.

High resonant frequency in the UHF range is necessary for achieving high resolution imaging of microstructures. Thickness-mode resonant frequency is determined by the thickness of the piezoelectric layer. Because the thicknesses of $LiNbO_3$ plates were several ten to several hundred μm, the center frequencies of these transducers were in the VHF range (several ten to several hundred MHz). Several μm thin piezoelectric layers are necessary in a transducer operating in the UHF range. On the other hand, thin film transducers that can excite both the longitudinal and shear modes have been studied for application to nondestructive evaluation [B.10-B.12]. In these studies, c-axis tilted piezoelectric thin layers are used. In previous studies, a transducer consisting of a single c-axis tilted ZnO layer were developed, as shown in Fig. B.1(a) and succeeded in the simultaneous excitation of longitudinal and shear waves [B.12-B.14].

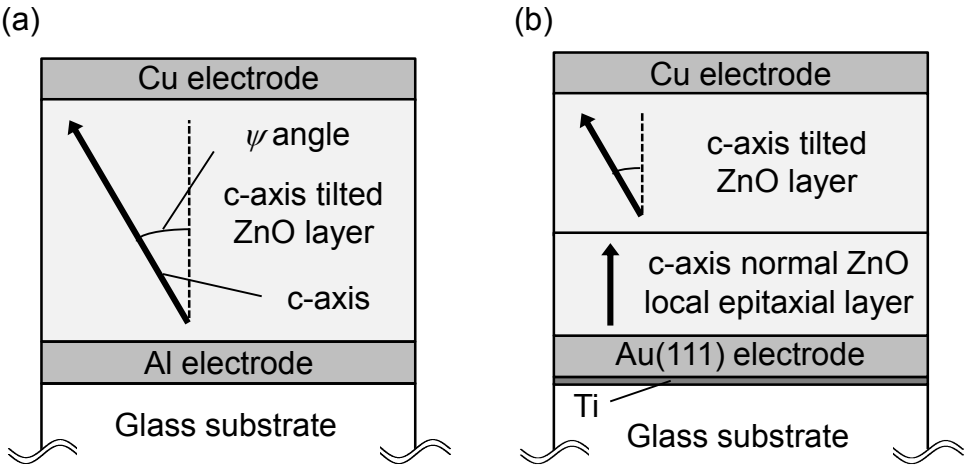

Fig. B.1 Structures of the transducers consisting of (a) single c-axis tilted ZnO layer and (b) c-axis tilted ZnO/c-axis normal ZnO multilayer.

In this study, a wideband multilayer transducer consisting of a c-axis tilted ZnO/c-axis normal ZnO multilayer is proposed, as shown in Fig. B.1(b). The crystalline orientation of a ZnO layer is strongly influenced by the crystalline orientation of the bottom electrode [B.15-B.17]. It is mainly caused by lattice fitting between the grains of the ZnO polycrystalline layer and the grains of the bottom polycrystalline electrode. The lattice misfit between ZnO($1\bar{1}00$) and Au(110) is only 2.5% [B.16-B.17]. Because of the local epitaxial relationship between ZnO(0001) and Au(111), the c-axis normal ZnO layer can be grown on a Au(111) layer even though these layers are polycrystal. It was predicted that the c-axis normal ZnO layer forms on the Au electrode due to the local epitaxial effect during the initial stage of ZnO deposition, and c-axis tilted orientation gradually forms as growth proceeds. This means that the c-axis tilted ZnO/c-axis normal ZnO multilayer can be continuously grown in one deposition process. The multilayer transducer consisting of these layers is expected to excite both the fundamental and second-overtone modes.

To demonstrate this idea experimentally, a c-axis tilted ZnO/c-axis normal ZnO multilayer on a Au(111) layer was fabricated by sputtering deposition. Next, the crystalline orientations of the multilayer transducer were investigated by an XRD pole figure and a scanning electron microscopy

(SEM) analyses. Finally, it was demonstrated that the c-axis tilted ZnO/c-axis normal ZnO multilayer is suitable for a wideband transducer by a comparison between the theoretical and experimental frequency responses of the transducer conversion loss characteristics.

B.2 EXPERIMENTAL METHODS

B.2.a TRANSDUCER FABRICATION

A silica glass (0.625 mm thickness, Tosoh, ED-B) with Au(111) (0.15 μm)/Ti (0.01 μm) layers was used as a substrate. The c-axis tilted ZnO/c-axis normal ZnO multilayers shown in Fig. B.1(b) were deposited on the substrate using an RF magnetron sputtering system (Ulvac Kiko, RFS-200) with a neodymium magnet, as shown in Fig. B.2. The substrate was set at 80º with respect to the ZnO target surface at the anode center [B.12-B.14]. Deposition conditions were set as shown in Table B.1. The c-axis 20 to 30º tilted ZnO single layer on the Al bottom electrode with good crystalline alignment can be formed under these conditions [B.13]. These conditions were not changed during the ZnO multilayer deposition. Finally, the Cu top electrode layer (0.18 μm) was evaporated on the ZnO layer surface.

Table B.1 Deposition conditions for c-axis tilted ZnO/c-axis normal ZnO multilayer

RF power	13.56 MHz, 200 W
Total gas pressure	1.0 Pa
Ar / O_2	3 / 1
Substrate heating	400 ºC
Deposition time	1 hour

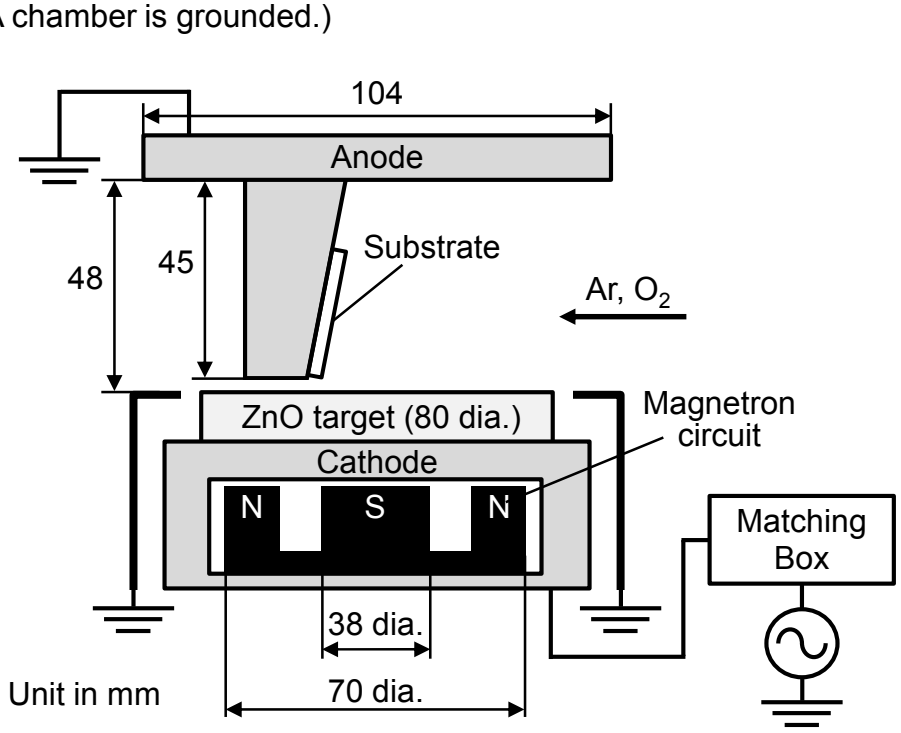

Fig. B.2 RF magnetron sputtering system for fabricating c-axis tilted ZnO/c-axis normal ZnO multilayer.

B.2.b TRANSDUCER CHARACTERIZATION

Crystalline orientation of the transducer was determined by XRD pole figure analysis (PANalytical, X-pert Pro MRD). The ψ-scan profile curves of Au(111) and ZnO(0002) in the transducer were measured. The ψ angle, where a (0002) ZnO peak appears, corresponds to the c-axis tilt angle from the normal to the transducer surface. The structure of crystal grain growth was observed by cross-sectional SEM.

To measure the piezoelectric properties of the transducer, acoustic waves were excited by applying a high frequency sinusoidal electric field between the top and bottom electrodes [B.18, B.19]. Longitudinal and shear waves propagate into the substrate and reflected at the top electrode surface and the bottom surface of the substrate. These waves were observed using inverse Fourier transform of reflection coefficients (S_{11}) of the transducer, which were

measured using a network analyzer (Agilent, E5071B) with a microwave probing system (GGB Industries, Picoprobe model 40A). Top electrode areas were adjusted to have the capacitive impedance of the layers close to 50 Ω at fundamental thickness longitudinal or shear mode resonant frequency. Conversion losses of the transducer were calculated from a Fourier transform of the first echo in longitudinal or shear waves. In the conversion losses, the effect of the propagation loss in the silica glass substrate was subtracted using $\alpha/f^2 = 9.55\times10^{-16}$ dB·s^2/m for a longitudinal wave or $\alpha/f^2 = 1.99\times10^{-15}$ dB·s^2/m for a shear wave [B.20, B.21]

This experimental conversion losses were compared with the theoretical conversion losses of a single layer transducer and a multilayer transducer. Theoretical curves were calculated using a modified Mason's equivalent circuit model including the effect of c-axis tilt angle and electrodes [B.18, B.19] The physical constant tensors of the ZnO layer were assumed to be identical to the single crystal values and properly rotated in accordance with the c-axis tilt angle of the ZnO layer [B.22]

B.3 CRYSTALLINE ORIENTATION OF THE TRANSDUCER

Figure B.3 shows the ψ-scan profile curve of Au(111) in the multilayer transducer [Fig. B.1(b)]. The maximum value of ψ-scan profile curve was observed at ψ = -0.2º, indicating that the Au(111) layer was parallel to the substrate. The ψ-scan FWHM of this curve was 5.6º. Figures 4(a) and 4(b) show the ψ-scan profile curves of ZnO(0002) in the single layer transducer [Fig. B.1(a)] and the multilayer transducer [Fig. B.1(b)], respectively. The single layer transducer was also prepared for comparison with the multilayer transducer. Only one peak was observed at ψ = 21.6º in the single layer transducer. This peak indicates that the c-axis tilt angle of the ZnO single layer is 21.6º. Generally, the c-axis normal ZnO local epitaxial layer is not grown on the Al electrode, because the surface of Al is covered with amorphous aluminum oxide in the presence of oxygen [B.16, B.17]. Therefore,

the c-axis tilted ZnO layer was grown on the Al electrode surface in this case. In contrast, two peaks were observed at ψ = -0.7 and 22.0º in the multilayer transducer, and the ψ-scan FWHM of the peak at ψ = -0.7 was 6.6º in Fig. B.4(b). This result shows that the multilayer transducer included two different orientations: c-axis normal and c-axis 22.0º tilted orientations. In general, the surface of Au does not oxidize, and therefore, the c-axis normal ZnO layer is epitaxially grown on the Au(111) layer [B.16, B.17].

A cross-sectional SEM image of the multilayer transducer is shown in Fig. B.5. Crystal grain growth in the normal direction on the Au bottom electrode was observed during the initial stage of ZnO layer deposition. Crystal growth direction began to tilt at the c-axis normal layer thickness of 1.25 μm. The author can confirm that the c-axis tilted ZnO/c-axis normal ZnO multilayer was continuously grown during one deposition process.

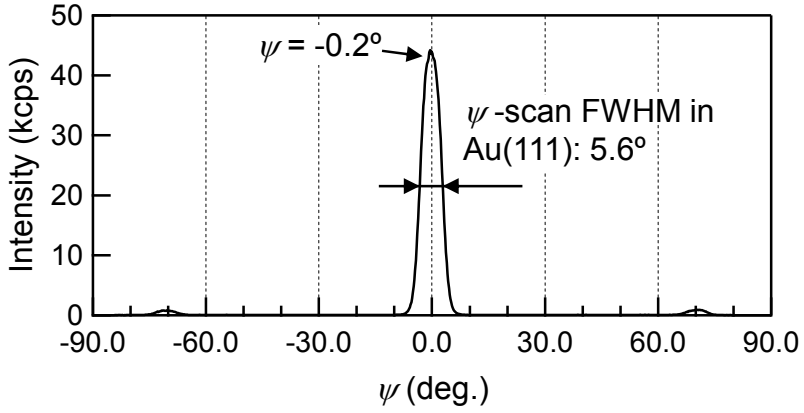

Fig. B.3 ψ-scan profile curve of Au(111) in the multilayer transducer.

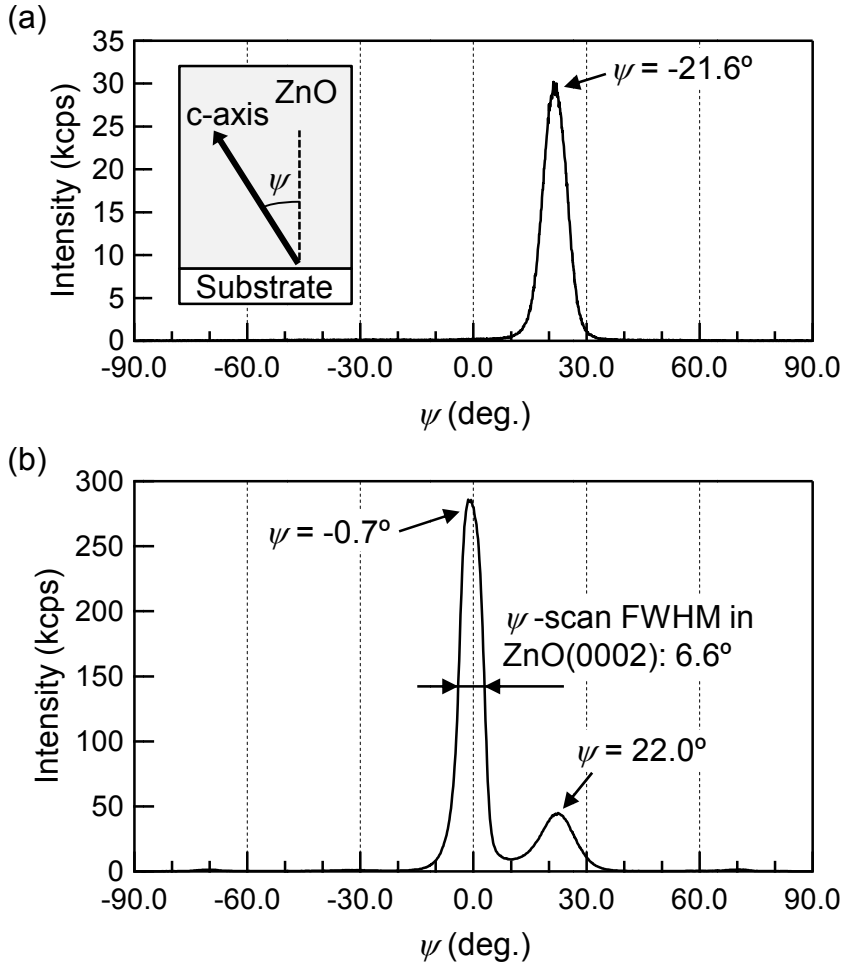

Fig. B.4 ψ-scan profile curves of ZnO(0002) in (a) the single layer transducer and (b) multilayer transducer.

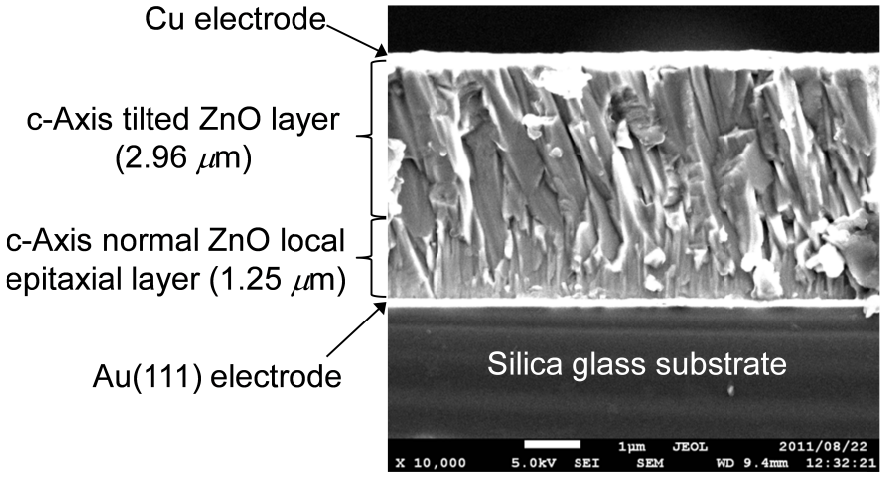

Fig. B.5 Cross-sectional SEM image of the multilayer transducer.

The results shown in Figs. B.3-B.5 indicate that the c-axis normal ZnO layer grew on the Au(111) layer by local epitaxial relationship between ZnO(0001) and Au(111) during the initial stage of ZnO layer deposition. It seems that this local epitaxial effect decreases as ZnO film growth proceeds. Therefore, the c-axis tilted ZnO layer is grown instead of the c-axis normal layer, because the sputtered particles tilt to the substrate plane [B.23, B.24] The ZnO transducer with the c-axis tilted ZnO/c-axis normal ZnO multilayer thus can be fabricated continuously without changing the conditions during the deposition.

The thickness of the c-axis normal layer was 1.25 μm in this study. The origin of 1.25 μm thickness is not clear, but this thickness may be determined by the thickness that the epitaxial effect from the bottom electrode reaches, and the thickness can be controlled by the crystallinity of the bottom electrode or deposition conditions.

B.4 FREQUENCY CHARACTERISTICS OF THE TRANSDUCER

Figures B.6(a) and B.6(b) show longitudinal wave and shear wave conversion losses of the transducers. Two theoretical curves were calculated using Mason's equivalent model. One was the characteristic of the single layer transducer (with the thickness of c-axis 22.0º tilted layer being 4.21 μm) and the other was that of the multilayer transducer (with the thicknesses of the c-axis normal and 22.0º tilted layers being 1.25 and 2.96 μm, respectively). The fundamental mode resonant frequencies of the longitudinal wave (L_1) and shear wave (S_1) are the frequencies of minimum points of the conversion losses. L1 and S1 were found at 630 and 300 MHz, respectively.

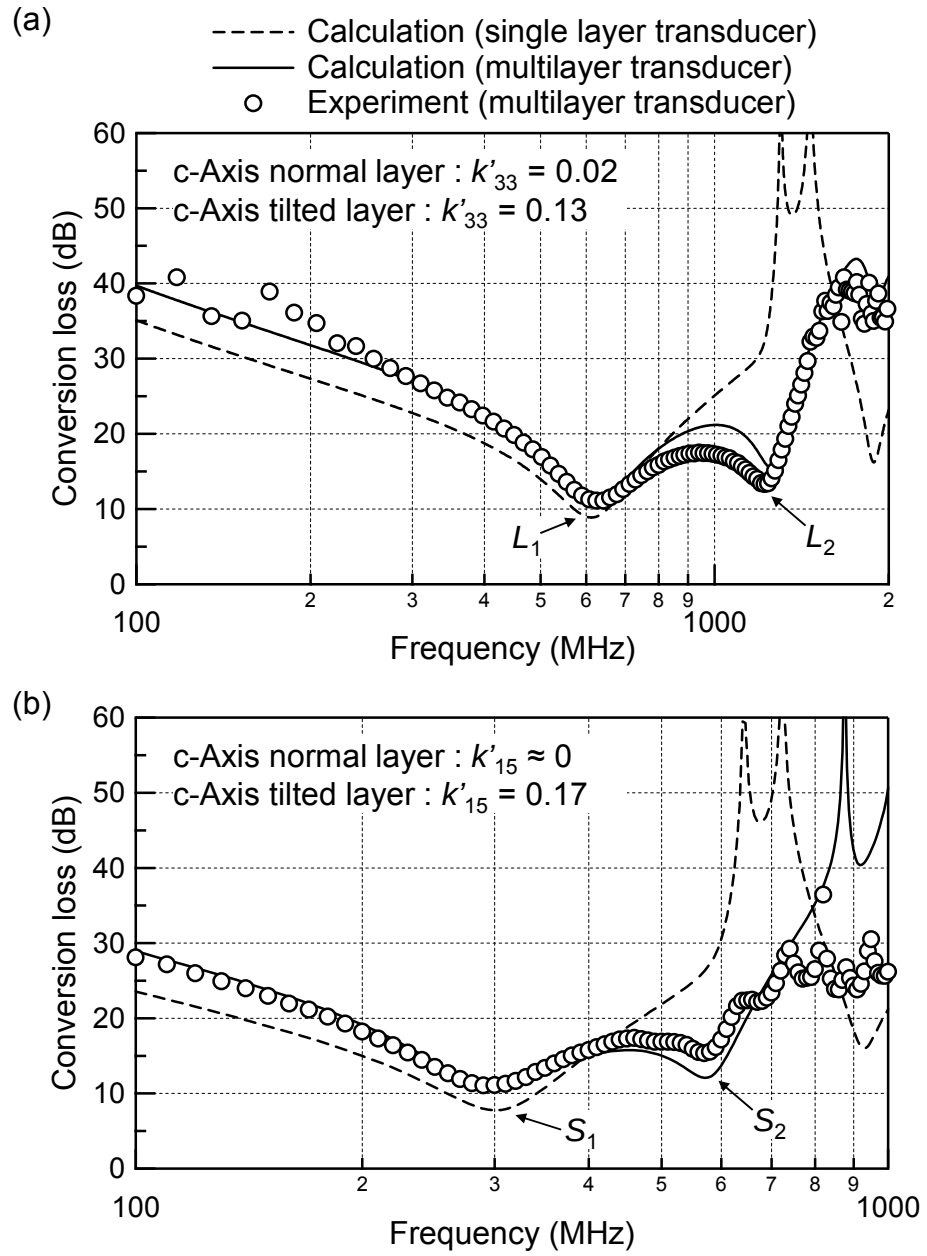

Fig. B.6 (a) Longitudinal wave and (b) shear wave conversion losses of the transducers. Dashed lines show the theoretical curves of the single layer transducer. Circles and lines show the experimental and theoretical curves of the multilayer transducer, respectively.

A second-overtone mode excitation is not found in the theoretical curve of the single layer transducer in Figs. B.6(a) and B.6(b). Figures B.7(a) and B.7(b) show schematic diagrams of piezoelectric polarizations of the single layer and multilayer transducers, respectively. Stresses or piezoelectric

polarizations induced at the upper and lower parts of the piezoelectric layer cancel each other in the single layer transducer, and acoustic waves cannot be excited and detected in a second-overtone mode. In contrast, the second-overtone modes of the longitudinal wave (L_2) and shear wave (S_2) were observed in the multilayer transducer at 1.22 GHz and 580 MHz, respectively. Stresses or piezoelectric polarizations induced at the c-axis tilted ZnO/c-axis normal ZnO multilayer are not equal and are not completely canceled, as shown in Fig. B.7(b). Second-overtone modes are then excited and detected. The frequency bandwidth of the multilayer transducer was broader than that of the single layer transducer in the UHF range, because the fundamental and second-overtone modes were excited. Longitudinal and shear conversion losses of the multilayer transducer fell within 7 dB in the 500 MHz-1.3 GHz and 200-600 MHz ranges, respectively.

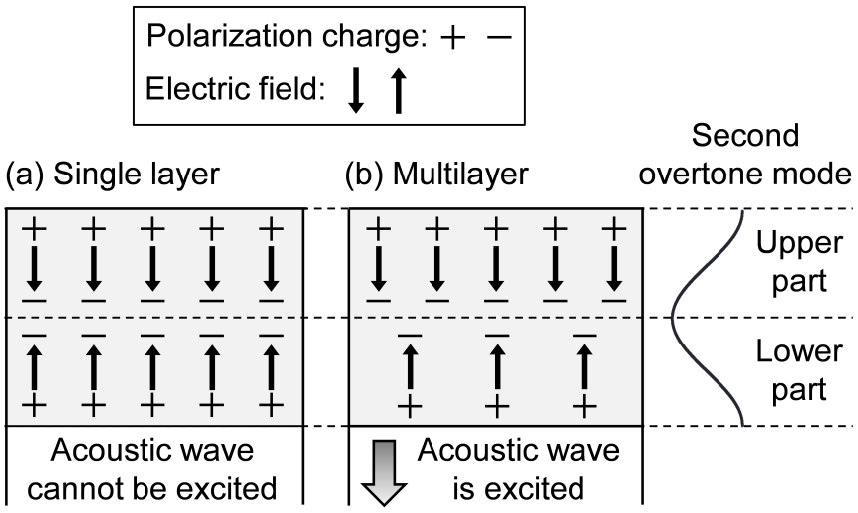

Fig. B.7 Schematic diagrams of piezoelectric polarizations induced at upper and lower parts of (a) the ZnO single layer and (b) ZnO multilayer.

B.5 CONCLUSIONS

The ZnO multimode transducer consisting of the c-axis tilted ZnO/c-axis normal ZnO multilayer has been investigated. The ZnO multilayer on a

Au(111)/Ti/silica glass substrate were fabricated by RF magnetron sputtering under the condition of the c-axis tilted ZnO layer growth. To grow the c-axis normal ZnO layer, the local epitaxial relationship between ZnO(0001) and Au(111) were used. XRD pole figure analysis and cross-sectional SEM revealed that the c-axis normal ZnO layer was grown on the Au(111) layer and, as ZnO grain growth proceeded, the c-axis 22.0º tilted ZnO layer was grown instead. Using this fabrication method for the multilayer transducer, the c-axis tilted ZnO/c-axis normal ZnO multilayer can be grown without changing the conditions during the deposition. This multilayer transducer simultaneously excited the second-overtone modes of longitudinal and shear waves as well as the fundamental modes in the UHF range. Therefore, the frequency bandwidth of the multilayer transducer was broader than that of a single layer transducer consisting of the c-axis tilted ZnO layer. The center frequencies of the longitudinal and shear waves of the multilayer transducer were 900 and 400 MHz, respectively. This wideband UHF transducer consisting of the c-axis tilted ZnO/c-axis normal ZnO multilayer has potential for use in acoustic imaging and nondestructive evaluation.

REFERENCES

[B.1] E. Maeva, F. Severin, C. Miyasaka, B. R. Tittmann, and R. Gr. Maev, IEEE Trans. Ultrason. Ferroelectr. Freq. Control **56**, 1352 (2009).

[B.2] S.-L. Chen, S.-W. Huang, T. Ling, S. Ashkenazi, and L. J. Guo, IEEE Trans. Ultrason. Ferroelectr. Freq. Control **56**, 2482 (2009).

[B.3] E. M. Strohm, G. J. Czarnota, and M. C. Kolios, IEEE Trans. Ultrason. Ferroelectr. Freq. Control **57**, 2293 (2010).

[B.4] S. Brand, M. Petzold, P. Czurratis, J. D. Reed, M. Lueck, C. Gregory, A. Huffman, J. M. Lannon Jr., and D. S. Temple, in *Proc. 61st Electronic Components and Technology Conf.*, Lake Buena Vista, Florida, 31 May-3 June 2011, pp. 37-42.

[B.5] M. Xu and L. V. Wang, Rev. Sci. Instrum. **77**, 041101 (2006).

[B.6] Q. Zhou, S. Lau, D. Wu, and K. K. Shung, Prog. Mater. Sci. **56**, 139 (2011).

[B.7] K. Nakamura and H. Shimizu, in *IEEE 1989 Ultrasonics Symp. Proc.*, Montreal, Canada, 3-6 October 1989, pp. 309-318.

[B.8] K. Nakamura, K. Fukuzawa, K. Yamada, and S. Saito, IEEE Trans. Ultrason. Ferroelectr. Freq. Control **50**, 1558 (2003).

[B.9] K. Nakamura, K. Fukuzawa, K. Yamada, and S. Saito, IEEE Trans. Ultrason. Ferroelectr. Freq. Control **53**, 651 (2006).

[B.10] C.-K. Jen, K. Sreenivas, and M. Sayer, J. Acoust. Soc. Am. **84**, 26 (1988).

[B.11] J. M. Rouvaen, A. Menhaj-Rivenq, P. Logette, P. Goutin, and F. Haine, J. Phys. D **33**, 1287 (2000).

[B.12] T. Yanagitani, N. Morisato, S. Takayanagi, M. Matsukawa, and Y. Watanabe, IEEE Trans. Ultrason. Ferroelectr. Freq. Control **58**, 1062 (2011).

[B.13] T. Matsuo, T. Yanagitani, M Matsukawa, and Y. Watanabe, in *2007 IEEE Ultrasonics Symp. Proc.*, New York City, New York, 28-31 October 2007, pp. 1229-1232.

[B.14] T. Matsuo, T. Yanagitani, M Matsukawa, and Y. Watanabe, in *2007 IEEE Ultrasonics Symp. Proc.*, New York City, New York, 28-31 October 2007, pp. 1874-1877.,

[B.15] T. Shiosaki, in *IEEE 1978 Ultrasonics Symp. Proc.*, Cherry Hill, New Jersey, 25-27 September 1978, pp. 100-110.

[B.16] Y. Yoshino, K. Inoue, M. Takeuchi, and K. Ohwada, Vacuum **51**, 601 (1998).

[B.17] Y. Yoshino, J. Appl. Phys. **105**, 061623 (2009).

[B.18] T. Yanagitani, T. Nohara, M. Matsukawa, Y. Watanabe, and T. Otani, IEEE Trans. Ultrason. Ferroelectr. Freq. Control **58**, 1062 (2011).

[B.19] T. Yanagitani and M. Kiuchi, J. Appl. Phys. **102**, 024110 (2007).

[B.20] J. Kushibiki and M. Arakawa, IEICE Tech. Rep. US2004-72 (2004) [in Japanese].

[B.21] D. B. Fraser, J. T. Krause, and A. H. Meizler, Appl. Phys. Lett. **11**, 308 (1967).

[B.22] L. Qin and Q. M. Wang, J. Appl. Phys. **107**, 114102 (2010).

[B.23] T. Kawamoto, T. Yanagitani, M. Matsukawa, Y. Watanabe, Y. Mori, S. Sasaki, and M. Oba, Jpn. J. Appl. Phys. **49**, 07HD16 (2010).

[B.24] M. C. Pan, T. A. Bui, Y. C. Nien, and W. C. Shih, Jpn. J. Appl. Phys. **50**, 07HD02 (2011).